Modelling Nanoscale Processes at GaAs(001) Surfaces

Kennet Daven Rodriguez Hannikainen

A thesis submitted for the degree of Doctor of Philosophy

School of Physics and Astronomy, Cardiff University, United Kingdom

September 2020

Abstract

GaAs(001) is one of the most important semiconductor surfaces in today's technology. Since the invention of molecular beam epitaxy in the late 1960s, this surface has been the substrate to complex heterostructures and diverse nanostructures that have found and continue to find novel applications in optoelectronic devices. For this reason, the fundamental science of the GaAs(001) surface has been studied intensively over the past few decades, from the diverse reconstructions it exhibits to the mechanisms of epitaxial growth occurring on it. For the most part these studies have been documented by *ex-situ* characterization techniques such as atomic force microscopy (for morphological analysis) or scanning tunneling microscopy (for atomistic analysis). During the early years of MBE, investigation of the ongoing kinetic surface processes during growth was essentially limited to the use of *in-situ* reflection high energy electron diffraction, which can only give structural information averaged-out across the surface.

The design and assembly of a hybrid system simultaneously a low energy electron microscope and a molecular beam epitaxy reactor (by Prof David Jesson) has been a major breakthrough in investigating the fundamental physical processes occurring on GaAs(001) surfaces. In fact, it is the only instrument in the world capable of imaging III-As surfaces (with III = Ga or In) in real time and under realistic growth conditions. Over the past few years, the unique capabilities of this system have led to numerous experimental findings regarding fundamental aspects of the GaAs(001) surface which were previously inaccessible to conventional molecular beam epitaxy systems. Together with theoretical modelling, this has enlightened our understanding of this important surface. However, much still remains unknown regarding GaAs(001) in relation to growth. Therefore, making use of this unique experimental system and developing theoretical models, this thesis presents novel contributions to our understanding of the GaAs(001) surface, in particular regarding surface phase stability. Having this been team work, the author of this thesis has specialised in producing theoretical models and computations to help understand the experimental observations.

The first piece of work presented in this thesis is a novel form of surface phase coexistence on GaAs(001), occuring when the surface is heated under vacuum above $\sim 580°$C (a typical temperature for epitaxial growth on GaAs(001)). Under these conditions, Langmuir evaporation of the crystal becomes important and due to this, we directly imaged the spontaneous formation of metastable surface phase domains on GaAs(001) corresponding to a (6×6) periodicity. These metastable phases exist for some time before spontaneously transforming back to the thermodynamically stable parent phase (the well-known $c(8 \times 2)$ reconstruction), producing a dynamic phase coexistence between the two phases. Monte Carlo simulations were used to identify the key kinetic processes and investigate the interplay between phase metastability and evolving surface morphology. This is used to explain the measured temperature dependence of the time-averaged (6×6) coverage.

Next we present another piece of work in which we are able to map the surface phase diagram of GaAs(001) by combining droplet epitaxy with low energy electron microscopy imaging techniques. Upon subjecting Ga droplets on the GaAs(001) surface to an As flux we observe a sequence of well-defined surface phases with distance to the droplet edge. Using a simple model which links the spatial coordinates of phase boundaries to the free energy, we are able to interpret these phase patterns produced during droplet epitaxy. Based on the observed sequential order of the phases away from the droplet, it is possible to obtain important new information on surface phase stability. This is used to augment existing $T = 0\,\mathrm{K}$ phase diagrams generated by density functional theory calculations. We also establish the existence of a (3×6) phase, and confirm, that the controversial (6×6) phase is thermodynamically stable over a narrow range of conditions.

The last piece of work presented here is one that is purely theoretical. Since the mid 2000s a technique called local droplet etching has been used to produce nanohole templates on different III-As surfaces. It consists of high-temperature annealing ($T \sim 550°\mathrm{C} \rightarrow 600°\mathrm{C}$) of nanoscale group III liquid droplets on these surfaces under low As flux. Its main application is the production of strain-free quantum dots by subsequent filling of these holes by means of epitaxial growth. The main

advantage of this etching technique versus *ex situ* etching is the absence of defects and impurities as it is carried under epitaxial conditions and does not include foreign elements. Despite this technique having been widely used, the physical mechanism of droplet etching is not yet well understood. Here we present a model for the case of Ga droplet etching of GaAs which, considering the different kinetic mechanisms of mass transport, produces dynamic simulations of nanohole formation and is able to answer the major open questions regarding this technique.

Acknowledgments

Firstly, I am grateful to Cardiff University for their generous financial support throughout my PhD. I am equally grateful to my supervisors Prof David Jesson and Dr Juan Pereiro Viterbo for their invaluable guidance during these years, and to Dr Jerry Tersoff, from IBM T. J. Watson Research Center, for helpful discussions. I would also like to thank the rest of my teammates Dr Yuran Niu and Dr Daniel Gomez Sanchez, Matyo Ivanov, and Debobrata Deb Tushit for their excellent experimental work and their friendship. They have made my studies and my time at Cardiff a lot more rewarding. A very special thanks you goes to Prof Emyr Macdonald, my first contact at Cardiff University, whose unfailing support during my last year has been vital.

I would also like to express my gratitude to all my department colleagues that have each contributed create the friendly atmosphere in the department, especially to Dr. Matt Smith, Tom Allcock, Geraint Gough and Eve North for plain being so nice! Thank you also to the IT team for their skills and immediate willingness to help, especially to my compatriot Adrian :). My thanks also goes to the administration team that has been so helpful, particularly to Nicola Hunt who helped me with my countless questions when I was new. They have made my overall Wales experience one I won't forget.

Lastly I have to thank my family and friends. My parents for their relentless encouragement. My cousins, especially Diana for her care and advice (I'm so lucky to have a physicist cousin). My brother Ivar for being my best friend and of course for his expert academic advice. My brother-from-a-different-mother Iker for the great times we've had through the years. My physics school teacher Mr O'Connor for raising my interest in physics. Last but not least my school friends, especially Nitin and Carlos, and my house mates in Cardiff, in particular Amy for her contagious laughter x).

List of Publications

K. Hannikainen, D. Gomez, J. Pereiro, Y. R. Niu, D. E. Jesson, *"Surface Phase Metastability during Langmuir Evaporation"*, Phys. Rev. Lett **123**, 186102 (2019)

C. X. Zheng, K. Hannikainen, Y. R. Niu, J. Tersoff, D. Gomez, J. Pereiro, D. E. Jesson, *"Mapping the surface phase diagram of GaAs(001) using droplet epitaxy"*, Phys. Rev. Mater. **3**, 124603 (2019)

Conference Oral Presentations

K. Hannikainen, D. Gomez, J. Pereiro, Y. R. Niu, D. E. Jesson, *"Surface Phase Metastability during Langmuir Evaporation"*, UK Semiconductors, Sheffield (UK), July 2019

K. Hannikainen, C. X. Zheng, Y. R. Niu, J. Tersoff, D. Gomez, J. Pereiro, D. E. Jesson, *"Mapping the surface phase diagram of GaAs(001) using droplet epitaxy"*, European Materials Research Society (EMRS) 2019 Fall Meeting, Warsaw (Poland), September 2019

Contents

List of Figures

Chapter 1

Introduction

The family of III-V semiconductors is one of the most important groups of materials in today's electronic and optoelectronic technology. In their pure state, these materials are binary compound crystals consisting of an element of column III of the periodic table and another of column V in a 1:1 ratio. Examples are GaAs, AlAs, GaP, InP, InSb etc, the most well-known III-V semiconductor being GaAs. This group of materials tend to have high electron mobilities, giving them improved electronic properties compared to their 'predecessor' Si. Also, as is the case for GaAs, many of the III-V materials have direct bandgaps, making them efficient materials for both light absorption and emission devices. Added to this, different III-V materials can be alloyed together to form ternary or even quaternary compounds. For example, the group III 'half' of GaAs is frequently alloyed with Al to form ternary $Al_xGa_{1-x}As$. The group V 'half' can also be alloyed to form quaternaries such as $Al_xGa_{1-x}P_yAs_{1-y}$. This enables 'bandgap engineering', i.e., tuning the bandgap of the alloy by changing the alloy ratio. These properties of III-V materials find numerous applications in optoelectronic devices. For example, they are used in light emission devices such as light-emitting diodes (LEDs) [13] or lasers [14], as well as in absorption devices such as photodetectors or solar cells [15]. In fact, the solar cell with the world record efficiency is a multi-junction cell made of several successive micro-layers of III-V alloys [16]. This cell achieves a peak efficiency of 47.1% under 143 suns concentration. Furthermore, a lot of research has been undertaken in recent years to harness the properties of nanoscale structures of III-V materials, such as III-V quantum dots or nanowires, when embedded in devices. For example, III-V

nanowires make photodetectors with high absorption and fast carrier collection [17] and can potentially produce high efficiency solar cells [18]. InGaAs quantum dots can make ultrafast lasers [19] and III-nitride quantum dots are proving to be promising for single photon emitting devices [20].

The diverse structures of III-V materials that are used in devices are usually grown epitaxially by means of crystal growth techniques, the most popular ones being metal-organic chemical vapour deposition (MOCVD) and molecular beam epitaxy (MBE). While MOCVD is frequently used in industry, MBE remains the fundamental technique of epitaxial crystal growth and is the preferred technique for basic science research. MBE is performed under ultra-high vacuum (UHV), i.e., at pressures below 10^{-9} Torr, with the III and V components supplied in very fine doses, usually by heating ultra-pure solid sources of the individual elements in Knudsen cells adjoined to growth chamber. The III and V precursor atoms/molecules in the fine vapour can then be adsorbed on to the substrate and begin growing the III-V crystal. The delicate dosage and the purity of the III and V source elements enables the crystal to grow epitaxially and form highly crystalline and highly pure III-V films. Most III-V materials tend to crystallize into cubic (zinc-blende) structures. Some, such as GaN, crystallize into hexagonal (wurtzite) structures instead. Interestingly, however, phase switching between zinc-blende and wurtzite crystal structures has been shown to be possible during growth of GaAs nanowires by tuning the growth conditions in the reactor [21].

Out of all the III-V materials, GaAs is the most well-known of all. The most basic form of GaAs MBE growth is GaAs epitaxy on GaAs(001). The GaAs(001) surface is hence one of the most technologically important crystal surfaces, and has been studied extensively through the years for purposes of growth [22–28]. In particular, the many different surface reconstructions (or surface phases) that GaAs(001) can present has long fascinated the MBE community [1, 29, 30]. The state of a surface in MBE is typically monitored in situ by means of reflection high energy electron diffraction (RHEED). By observing the diffraction patterns the surface periodicities are recognised. However, RHEED only gives structural information that is averaged-

out across the surface, and is generally incapable of supplying information as to the nanoscale details of GaAs surfaces. As a means of overcoming this difficulty, complex vacuum systems have been designed which connect MBE growth reactors to microscopy apparatuses such as atomic force microscopes (AFM) [31] or scanning tunneling microscopes (STM) [32]. In this way growth experiments can be carried in the MBE chamber, and the sample can then be transferred out *in vacuo* through to the microscopy chamber for charaterization after quenching the sample down to room temperature. This modus operandi permits observing the surface seconds after pausing the growth experiment, and, for example, has enabled the direct observation of the atomistic arrangements of many of the GaAs(001) phases [1]. However, the act of quenching the sample for transfer to the microscope may alter the surface unexpectedly, and kinetic surface mechanisms will shut down during the process, making it unfeasible to really observe the surface under growth conditions.

To investigate growth mechanisms in a precise manner, a few experimental systems around the world combine epitaxial growth and *in situ* microscopy, in an effort to visualise growth in real time. For example, there exist transmission electron microscopes (TEM) with gas-phase sources built onto them. Using such systems, meaningful conclusions regarding the atomic-scale details of nanowire growth have been reached [21, 33]. Given its characteristics, TEM is an outstanding tool to observe and monitor growth of three-dimensional objects such as nanowires, but it cannot be used to study the GaAs(001) surface. Regarding imaging 2-dimensional surfaces under growth conditions, there do exist systems which combine MBE and *in situ* STM. These have produced interesting results concerning InAs quantum dot formation on GaAs(001) [34, 35]. However the sample temperature is limited to about $\sim 300^{\circ}$C for STM imaging and the scanning greatly reduced the time resolution of this technique. Low energy electron microscopy (LEEM) is unparalleled in imaging 2-dimensional surfaces under growth conditions. LEEM microscopes provide a 'bird's eye view' of conducting surfaces at the micro/nanoscale, and, being a non-scanning technique, every point on the surface is imaged simultaneously, thereby enabling real-time imaging at video rates. Generally speaking, LEEM mi-

croscopes provide atomic resolution in the direction perpendicular to the surface, so that atomic steps can be resolved, and resolutions down to $\sim 5\,\mathrm{nm}$ in the plane of the surface, provided the alignment of the system is sufficiently good and vibrations are minimised. LEEM also tends to provide diffraction contrast, i.e., parts of the surface presenting different reconstructions will tend to show contrast. These unique characteristics of LEEM, not to mention the possibility of using the low energy electron diffraction (LEED) mode and 'dark-field' imaging modes, render LEEM an ideal *in situ* microscopy technique to investigate the structure and morphology of GaAs(001) surfaces under growth conditions.

The School of Physics and Astronomy of Cardiff University is home to a LEEM-MBE hybrid system which is the only one in the world that is capable of imaging III-As surfaces under growth conditions (III being Ga or In) [36]. By performing simple experiments in our system, remarkable results have been obtained through the years regarding fundamental aspects of the GaAs surface and processes occurring on it [4, 37–39]. The possibilities the system provides and the lack of experimental set-ups similar to ours motivates performing further experiments to discover fundamental aspects of the technologically important GaAs(001) surface. During the time the author of this thesis has been present, our group has produced significant results concerning the surface phase stability on GaAs(001) [40, 41]. Given the fundamental nature of the science that is done in our system, theoretical modelling becomes a valuable tool in understanding the observational results that are produced and, more generally, in understanding the GaAs(001) surface. For this reason, the author's full time during the PhD period has been dedicated to theoretical modelling and extensive analysis of LEEM data, but not to LEEM experiments. These were performed by fellow teammates Dr. Yuran Niu, Dr. Daniel Gomez Sanchez, Dr. Changxi Zheng, and Dr. Juan Pereiro Viterbo.

The outline of the thesis is as follows. In Chapter 2, the background theory underpinning the models developed in the rest of the thesis is outlined. In particular, the manner in which the thermodynamics and kinetics of GaAs(001) surfaces are treated is explained. This involves understanding the statistical properties of

adsorbed atoms (adatoms) on GaAs(001), surface atoms of the crystal, dissolved As atoms in Ga droplets, as well as the kinetic descriptions of these when the system evolves in time. Adding to this, surface phases are defined and the important concept of phase stability is thoroughly explained. Chapter 2 is also dedicated to introducing the basic principles of the LEEM technique and the different components of our LEEM-MBE system. After this, our sample preparation method is explained and a novel microscopy technique named selective energy dark field imaging (SEDF), which was recently developed in our group and was extensively used in the results of this thesis, is presented.

Chapter 3 is the first of three results chapters. In this Chapter, a novel form of surface phase coexistence is presented. In this work, we imaged the spontaneous formation of metastable (6×6)-reconstructed domains on the GaAs(001) $c(8 \times 2)$ surface during Langmuir evaporation. Eventually, these metastable phases transform to the thermodynamically stable $c(8 \times 2)$ parent phase, producing a dynamic phase coexistence with a temperature-dependent, time-averaged coverage. A Monte Carlo model was developed to identify the key kinetic processes and investigate the interplay between phase metastability and evolving surface morphology. This is used to explain the measured temperature dependence of the time-averaged (6×6) coverage.

In Chapter 4, we present a piece of work in which we map the surface phase diagram of GaAs(001) by combining droplet epitaxy with LEEM imaging techniques. We develop a simple model that considers the diffusion of Ga adatoms from the droplets and their reaction with the incoming As flux to link the spatial coordinates of the phase boundaries to free energy, and hence interpret the phase patterns produced during droplet epitaxy. The respective order of such phases with distance to the droplet allows us to incorporate them in an approximate manner on to existing $T = 0\,\mathrm{K}$ GaAs(001) phase diagrams. Our observations confirm the stability of the controversial (6×6) phase across a narrow range of Ga chemical potential, and we also establish the existence of a novel (3×6) phase.

In Chapter 5 a theoretical model for local droplet etching (LDE) of Ga droplets

on GaAs surfaces is presented. This technique is relatively modern but has been practiced intensively over the past few years [9,12,42–47]. The main use of LDE is to produce nanohole templates for subsequent filling with quantum dots [48–50]. This enables the formation of quantum dots on lattice matched systems and therefore the production of strain-free quantum dots. The model incorporates kinetic concepts of mass transport between the droplet, the crystal, and the adatom population, to explain the mechanism of droplet etching. The simulation results indicate that etching originates with GaAs deposition at the droplet contact line position, and is driven by the droplet's surface tension pulling on the solid. The consequent loss in As in the droplet induces drilling at liquid-solid interface under the bulk droplet in order to replenish the equilibrium As content. The simulations also show that, though seeming to be counterintuitive at first thought, a finite flux is necessary for etching. This fact, which had previously been observed experimentally [12], is explained within the simple physical concepts of our theoretical model. The model should, in fact, be applicable to other III-As systems such Al etching of AlAs or In etching of InAs.

Chapter 6, the final chapter, is an outline of the conclusions that have been drawn from the results presented throughout the previous chapters.

Chapter 2

Background Theory and Methods

2.1 Thermodynamics of GaAs(001) Surfaces

Thin film growth, nanostructure fabrication and other surface processes are the overall result of mass transport at the atomic scale. Surface atoms perform kinetic processes on heated surfaces, such as diffusion, reaction with another atom or desorption from the surface [51]. These processes are typically limited by potential barriers which are overcome by thermal excitation. To model processes at GaAs surfaces it is thus essential to use the tools and concepts of kinetics and thermodynamics [52, 53]. Here we will first examine thermodynamic aspects of GaAs(001) surfaces.

The physical system we consider is a semi-infinite solid under vacuum, i.e., an infinite solid sliced in two across the (001) direction. On the surface there are loosely bound atoms that are free to diffuse across the surface. These are called 'adatoms' (short for adsorbed atoms), which can have different sources. For example, they can be deposited on the surface (as done in MBE), they can come from the bulk solid itself by decomposition of the latter, or they can detach from droplets as we will see in later chapters. Let us now introduce some basic concepts of thermodynamics that are of use in modeling the GaAs(001) surface.

In MBE growth experiments, surfaces are heated and held at a certain temperature T and under an ambient pressure P. Therefore, the relevant thermodynamic

potential is the system's Gibbs free energy G, defined as

$$G(T,P) = U - ST + PV, \tag{2.1}$$

where U is the system's internal energy, S is the entropy, T is the absolute temperature, P is the pressure, and V is the volume (see, for example Ref. [54]).

Equilibrium configurations of the system will then be ones that minimize this Gibbs free energy. Of fundamental importance is then the concept of chemical potential μ_i of a species i in the system, defined as

$$\mu_i \equiv \frac{\partial G}{\partial N_i}|_{T,P}, \tag{2.2}$$

that is, the change in the system's free energy upon adding a particle of species i to the system. The chemical potentials of the species are central quantities in a system governed by mass transport, as are heated GaAs(001) surfaces; mass will tend to be transported to regions where the chemical potential is lower, thus providing a configuration for the system with lower free energy. As we will see in the following chapters, the concept of chemical potential will be utilized frequently modeling processes at GaAs(001) surfaces.

Having defined chemical potential, the free energy G of the system as given by Eq. (2.1) can be written as

$$G = \sum_i \mu_i \, N_i, \tag{2.3}$$

as stated by Euler's relation. The sum spans over all species i in the system, N_i is the number of molecules of species i, and μ_i is the chemical potential of species i. This alternative form of writing the free energy in terms of the chemical potentials of the constituents will also be useful in the following sections.

Let us now apply the concepts of free energy and chemical potential to the different constituents of a GaAs(001) surface. We will consider first the adatoms in Section 2.1.1, then Ga droplets on the GaAs(001) surface in Section 2.1.2, and last the underlying bulk solid in Section 2.1.3. The concepts introduced herein are preliminary to the notions of kinetics outlined in Section 2.2, and will be used in

Chapters 4 and 5.

2.1.1 Adatoms on GaAs(001)

In our simplified model system, the species present will be Ga adatoms, As adatoms, and GaAs 'molecules' making up the solid. Adatoms are losely bound surface atoms that are free to diffuse along the surface. We assume that the growth/decomposition reaction between the adatoms and the solid is simply

$$\mathrm{Ga} + \mathrm{As} \longleftrightarrow \mathrm{GaAs}, \tag{2.4}$$

where a Ga adatom reacts with an As adatom to produce solid GaAs, or vice versa, a GaAs pair belonging to the bulk solid decomposes into a Ga adatom and a As adatom. In typical MBE growth experiments, the arsenic flux impinging the surface is usually made of As_4 (or As_2 molecules if an As cracker is used). The chemistry of these molecules on GaAs(001) surfaces is very complex, especially for the case of As_4 [26–28], as it is unclear what the growth reaction/mechanism consists of. Even when As_2 is used, the growth mechanisms are thought to be non-trivial [24, 55]. For this reason we assume the simplest of possibilities for the growth reaction; a Ga and an As adatom encounter each other and react to form GaAs as described by the growth reaction of Eq. (2.4). In modeling growth in Chapters 4 and 5, it is necessary to first consider the chemical potentials of Ga, As, and GaAs, and what the conditions are for equilibrium between the adatom population and the bulk crystal.

Consider now that the number of Ga adatoms changes an amount dN by undergoing the growth reaction of Eq. (2.4). Then the amount of As adatoms would also change by dN, and the amount of GaAs 'molecules' would change by $-dN$. According to Eq. (2.3) the change in the system's free energy would be

$$dG = (\mu_{\mathrm{Ga}} + \mu_{\mathrm{As}} - \mu_{\mathrm{GaAs}})\, dN, \tag{2.5}$$

where μ_{Ga}, μ_{As}, and μ_{GaAs} are the chemical potentials of Ga, As, and GaAs respec-

tively. The condition for equilibrium between the adatom population and the solid is minimization of the free energy G, that is $dG = 0$ or

$$\mu_{\mathrm{Ga}} + \mu_{\mathrm{As}} = \mu_{\mathrm{GaAs}}. \tag{2.6}$$

As we will now demonstrate, the adatom chemical potentials are functions of the adatoms densities, so that Eq. (2.6) is essentially a condition upon the concentration of Ga and As on the surface. To derive a simple expression for the chemical potentials, we assume that the adatoms can occupy certain surface sites, and may diffuse across the surface by hopping from one site to the next. The free energy G of the system will be the free energy of the crystal $G_{crystal}$ plus the contribution of the adatoms. Neglecting adatom-adatom interactions, we can add the contributions of the Ga and the As adatoms to the free energy independently, so that the system's free energy is

$$G = G_{crystal} + U_{\mathrm{Ga}} - S_{\mathrm{Ga}}T + U_{\mathrm{As}} - S_{\mathrm{As}}T, \tag{2.7}$$

where U_{Ga} and U_{As} are the energies of the Ga and the As adatoms respectively, and S_{Ga} and S_{As} are the contributions to the entropy of the Ga and the As adatom population respectively. The PV terms, (as per the definition of Gibbs free energy in Eq. (2.1)) are irrelevant for the case of adatoms. If there are n_{Ga} surface sites for Ga adatoms, and N_{Ga} Ga adatoms, the number of ways to distribute the adatoms among the sites is $n_{\mathrm{Ga}}!/((n_{\mathrm{Ga}} - N_{\mathrm{Ga}})!N_{\mathrm{Ga}}!)$. Therefore, assuming the only source of entropy is permutations of the adatoms among the allowed sites, we have that $U_{\mathrm{Ga}} = N_{\mathrm{Ga}}E_{\mathrm{Ga}}$, and $S_{\mathrm{Ga}} = k\ln\left(n_{\mathrm{Ga}}!/((n_{\mathrm{Ga}} - N_{\mathrm{Ga}})!N_{\mathrm{Ga}}!)\right)$, where k is the Boltzmann constant and E_{Ga} is the energy of binding to the surface of a Ga adatom. Substituting these expressions (and the analogous ones for As) into Eq. (2.7) we have

$$G = G_{crystal} + N_{\mathrm{Ga}}E_{\mathrm{Ga}} - kT\ln\left(\frac{n_{\mathrm{Ga}}!}{(n_{\mathrm{Ga}} - N_{\mathrm{Ga}})!N_{\mathrm{Ga}}!}\right) + N_{\mathrm{As}}E_{\mathrm{As}} - kT\ln\left(\frac{n_{\mathrm{As}}!}{(n_{\mathrm{As}} - N_{\mathrm{As}})!N_{\mathrm{As}}!}\right). \tag{2.8}$$

Applying $\ln\left(\frac{n_{\mathrm{Ga}}!}{(n_{\mathrm{Ga}} - N_{\mathrm{Ga}})!N_{\mathrm{Ga}}!}\right) = \ln(n_{\mathrm{Ga}}!) - \ln((n_{\mathrm{Ga}} - N_{\mathrm{Ga}})!) - \ln(N_{\mathrm{Ga}}!)$ and using

Stirling's approximation [1] we can calculate the chemical potential $\mu_{\mathrm{Ga}} = \partial G/\partial N_{\mathrm{Ga}}$ by differentiating now Eq. (2.8) to get $\mu_{\mathrm{Ga}} = E_{\mathrm{Ga}} + kT\ln\left(\frac{N_{\mathrm{Ga}}}{n_{\mathrm{Ga}}-N_{\mathrm{Ga}}}\right) \approx E_{\mathrm{Ga}} + kT\ln\left(\frac{N_{\mathrm{Ga}}}{n_{\mathrm{Ga}}}\right)$ as we assume low adatom coverages, i.e., $n_{\mathrm{Ga}} >> N_{\mathrm{Ga}}$. Therefore we may write

$$\mu_{\mathrm{Ga}} = E_{\mathrm{Ga}} + kT\ln\left(\frac{C_{\mathrm{Ga}}}{\nu_{\mathrm{Ga}}}\right), \tag{2.9}$$

where C_{Ga} is the number of Ga adatoms per unit area, and ν_{Ga} is now the number of sites per unit area, with, of course, an analogous expression applying for As. Eq. (2.9) is a fundamental equation in this work, and coincides with the expression in Ref. [56]. It relates adatom chemical potential to adatom concentration, so that at a given temperature T, the chemical potential is essentially the natural logarithm of the adatom concentration. For this reason, the terms adatom chemical potential and adatom concentration are often used interchangeably.

With Eq. (2.9) at hand, we will now consider the concept of adatom concentrations in equilibrium with the solid. Setting C_{Ga} in terms of μ_{Ga} in Eq. (2.9) we have

$$C_{\mathrm{Ga}} = \nu_{\mathrm{Ga}}\exp\left(\frac{\mu_{\mathrm{Ga}} - E_{\mathrm{Ga}}}{kT}\right). \tag{2.10}$$

Multiplying by the analogous expression for As, we have

$$C_{\mathrm{Ga}}C_{\mathrm{As}} = \nu_{\mathrm{Ga}}\nu_{\mathrm{As}}\exp\left(\frac{\mu_{\mathrm{Ga}} + \mu_{\mathrm{As}} - E_{\mathrm{Ga}} - E_{\mathrm{As}}}{kT}\right). \tag{2.11}$$

Now, the adatom population will be in equilibrium with the solid when Eq. (2.6) is satisfied. Therefore, the adatom concentration product $C_{\mathrm{Ga}}C_{\mathrm{As}}$ of equilibrium with the solid is

$$(C_{\mathrm{Ga}}C_{\mathrm{As}})_{eq} = \nu_{\mathrm{Ga}}\nu_{\mathrm{As}}\exp\left(\frac{\mu_{\mathrm{GaAs}} - E_{\mathrm{Ga}} - E_{\mathrm{As}}}{kT}\right). \tag{2.12}$$

Note that the $(C_{\mathrm{Ga}}C_{\mathrm{As}})_{eq}$ is a property of the solid via the chemical potential μ_{GaAs}, so that a high μ_{GaAs} implies a high $(C_{\mathrm{Ga}}C_{\mathrm{As}})_{eq}$. It is also interesting that the quantity of equilibrium is in particular the product of the Ga and As densities, so that multiplying one by a factor α implies dividing the other by a factor α in order to maintain equilibrium. This is consistent with the fact that, as we will see in

[1] $\ln(x!) \approx x\ln(x) - x$ for large x

Section 2.2, $C_{\mathrm{Ga}}C_{\mathrm{As}}$ is proportional to the rate of reaction of Ga and As reaction to form GaAs, and equilibrium means that the rate of reaction equals the rate of decomposition of the solid.

2.1.2 Thermodynamics of Ga Droplets

In Chapter 5 we will consider Ga droplets under As flux, and hence growth at the liquid-solid interface between a Ga droplet and solid GaAs. Therefore, in this subsection we will consider the chemical potentials μ_{Ga} and μ_{As} in a Ga:As alloy, and how these depend on the As mole fraction x_{As}. These concepts are explained in great detail Chapter 3 of Ref. [52]. Here we will give only the basic concepts.

The free energy of an alloy with 2 components is of the form $G = G(T, P, N_1, N_2)$, where N_1 and N_2 are the number of atoms of either component of the alloy. From this, the free energy per atom of the alloy can be defined as

$$g(T, P, x) = \frac{G(T, P, N_1, N_2)}{N_1 + N_2}. \tag{2.13}$$

It can be shown that this g depends upon N_1 and N_2 only through the molar fraction x of either of the components, i.e., $x_1 = N_1/(N_1 + N_2)$ or $x_2 = N_2/(N_1 + N_2)$. Note that x_1 and x_2 are not independent, as $x_1 + x_2 = 1$. From here on we will concentrate on the case of the liquid Ga:As alloy but any of the following expressions apply to any alloy having two components. We also choose to consider the mole fraction for As, x_{As}, as an independent variable, given that As will be considered the solute inside the Ga solvent.

The free energy per atom g in Eq. (2.13) can be expressed as

$$g = (1 - x_{\mathrm{As}})\; g^l_{\mathrm{Ga}} + x_{\mathrm{As}}\, g^l_{\mathrm{As}} + g_{mix}, \tag{2.14}$$

where g^l_{Ga} and g^l_{As} are the free energy of formation of pure liquid Ga and pure liquid As, respectively, and g_{mix} is the extra free energy per atom, associated with the mixing. If the Ga:As alloy were an ideal system, i.e., one in which unlike atoms interact with each other in the same way as like atoms do with each other, then g_{mix}

would be simply $g_{mix} = -Ts_{mix}$, where s_{mix} is simply the configurational entropy of distributing N_{As} atoms amongst $N_{Ga} + N_{As}$ sites. This entropy of mixing is then $s_{mix} = k\ln\left[(N_{\mathrm{Ga}} + N_{\mathrm{As}})!/(N_{\mathrm{Ga}}!N_{\mathrm{As}}!)\right]$, or, using Stirling's approximation

$$s_{mix} = -k\left[(1 - x_{\mathrm{As}})\ln(1 - x_{\mathrm{As}}) + x_{\mathrm{As}}\ln(x_{\mathrm{As}})\right]. \tag{2.15}$$

However, in a Ga:As alloy, dissimilar components do not interact with each other in the same way as similar atoms do, and so the free energy of mixing g_{mix} has additional contributions to that of the configurational entropy, and is expressed as

$$g_{mix} = kT\left[(1 - x_{\mathrm{As}})\ln(1 - x_{\mathrm{As}}) + x_{\mathrm{As}}\ln(x_{\mathrm{As}})\right] + x_{\mathrm{As}}(1 - x_{\mathrm{As}})P(x_{\mathrm{As}}). \tag{2.16}$$

The extra term $x_{\mathrm{As}}(1-x_{\mathrm{As}})P(x_{\mathrm{As}})$ contains these contributions; the $x_{\mathrm{As}}(1-x_{\mathrm{As}})$ factor ensures the term is zero when there is no mixing, and $P(x_{\mathrm{As}})$ is a semi-empirical polynomial (known as the Redlich-Kister polynomial [57]) whose coefficients are obtained by fitting to experimental data. These coefficients are available in the database of Ref. [58].

Knowing the free energy per atom $g = g(T, P, x_{\mathrm{As}})$ of the alloy phase, the chemical potentials of both components can be computed. Using the definition of chemical potential (Eq. (2.2)) and the definition of the molar free energy (Eq. (2.13)) we may write $\mu_{\mathrm{As}} = \partial G/\partial N_{\mathrm{As}} = \partial/\partial N_{\mathrm{As}}\left[(N_{\mathrm{Ga}} + N_{\mathrm{As}})g\right] = g + (N_{\mathrm{Ga}} + N_{\mathrm{As}})\partial g/\partial x_{\mathrm{As}}$ and therefore

$$\mu_{\mathrm{As}} = g + (1 - x_{\mathrm{As}})\frac{\partial g}{\partial x_{\mathrm{As}}}, \tag{2.17}$$

and, analogously for Ga

$$\mu_{\mathrm{Ga}} = g - x_{\mathrm{As}}\frac{\partial g}{\partial x_{\mathrm{As}}}. \tag{2.18}$$

This method of calculating the chemical potentials is called the 'tangent' construction for the following reason: the equation of the tangent to $g(x_{\mathrm{As}})$ at x_{As} is $T_{x_{\mathrm{As}}}(x) = g(x_{\mathrm{As}}) + (x - x_{\mathrm{As}})\partial g/\partial x_{\mathrm{As}}$, and so, the chemical potentials are $\mu_{\mathrm{Ga}}(x_{\mathrm{As}}) = T_{x_{\mathrm{As}}}(x = 0)$ and $\mu_{\mathrm{As}}(x_{\mathrm{As}}) = T_{x_{\mathrm{As}}}(x = 1)$, i.e., the intercepts of the tangent line at x_{As} with the $x_{\mathrm{As}} = 0$ and $x_{\mathrm{As}} = 1$ lines. This is shown schematically in Fig. 2.1

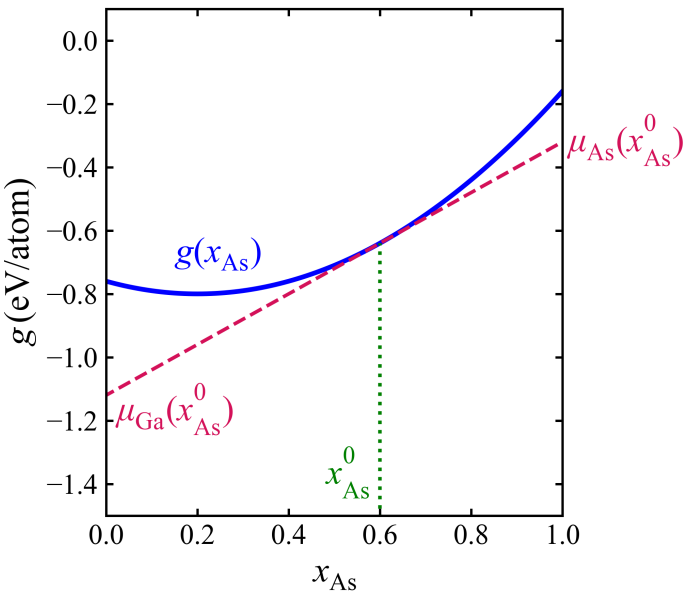

Figure 2.1: Schematic diagram explaining the 'tangent construction' for the chemical potentials μ_{Ga} and μ_{As} in the Ga:As alloy. The blue curved line represents the free energy $g(x_{\mathrm{As}})$ per atom of the alloy as a function of x_{As}. The red dashed line is the tangent to the $g(x_{\mathrm{As}})$ curve at a certain As mole fraction value x^0_{As}. As is indicated on the diagram, the Ga and As chemical potentials $\mu_{\mathrm{Ga}}(x^0_{\mathrm{As}})$ and $\mu_{\mathrm{As}}(x^0_{\mathrm{As}})$ for x^0_{As} are the values at which the tangent line crosses the $x_{\mathrm{As}} = 0$ and $x_{\mathrm{As}} = 1$ axes, respectively.

Substituting the expression for the free energy per atom of Eq. (2.13) into Eq. (2.18) and Eq. (2.17) (taking into consideration the form of g_{mix} in Eq. (2.16)) yields

$$\mu_{\mathrm{As}} = g^l_{\mathrm{As}} + kT\ln(x_{\mathrm{As}}) + (1-x_{\mathrm{As}})^2 P(x_{\mathrm{As}}) + x_{\mathrm{As}}(1-x_{\mathrm{As}})^2 P'(x_{\mathrm{As}}) \tag{2.19}$$

and

$$\mu_{\mathrm{Ga}} = g^l_{\mathrm{Ga}} + kT\ln(1-x_{\mathrm{As}}) + x^2_{\mathrm{As}} P(x_{\mathrm{As}}) - x^2_{\mathrm{As}}(1-x_{\mathrm{As}})P'(x_{\mathrm{As}}). \tag{2.20}$$

Note in Eq. (2.19) and Eq. (2.20) the logarithmic dependence of the chemical potentials with concentration (ignoring the terms containing the Redlich-Kister polynomial $P(x_{\mathrm{As}})$), similar to what was obtained for the adatom chemical potential in Eq. (2.9), and reflecting the contribution of configurational entropy to the chemical potential.

Knowing how the chemical potentials μ_{Ga} and μ_{As} depend upon the As mole

fraction x_{As} in the liquid, it is now natural to ask what value of x_{As} is that of equilibrium with the solid. In analogy to the case of the adatoms, we assume that the growth reaction at the liquid-solid interface is simply the reaction of an As atom dissolved in the liquid with a Ga liquid atom at a GaAs lattice site, as described by Eq. (2.4). Therefore, the arsenic mole fraction, x_{As}^{eq}, of equilibrium with the solid will be the one that satisfies $\mu_{\mathrm{Ga}} + \mu_{\mathrm{As}} = \mu_{\mathrm{GaAs}}$, with μ_{Ga} and μ_{As} given by Eq. (2.19) and Eq. (2.20).

The value of x_{As}^{eq} turns out to be very small at all temperatures; for $T = 600°\mathrm{C}$, x_{As}^{eq} it is only 0.18%. For this reason, it is useful to approximate Eq. (2.19) and Eq. (2.20) for small x_{As} to obtain simply

$$\mu_{\mathrm{As}} = g_{\mathrm{As}}^{l} + kT\ln(x_{\mathrm{As}}) + P(0) \tag{2.21}$$

and

$$\mu_{\mathrm{Ga}} = g_{\mathrm{Ga}}^{l}, \tag{2.22}$$

where μ_{As} is effectively the natural logarithm of x_{As}, and μ_{Ga} equals the free energy per atom of pure liquidus Ga, and is therefore independent of x_{As}. With Eq. (2.21) and Eq. (2.22) at hand, we can obtain an approximate expression for x_{As}^{eq} by solving $\mu_{\mathrm{Ga}} + \mu_{\mathrm{As}} = \mu_{\mathrm{GaAs}}$ to get

$$x_{\mathrm{As}}^{eq} = \exp\left(\frac{\mu_{\mathrm{GaAs}} - g_{\mathrm{Ga}}^{l} - g_{\mathrm{As}}^{l} - P(0)}{kT}\right). \tag{2.23}$$

As can be observed, it is somewhat analogous to the expression of the adatom concentration product of equilibrium with the solid (Eq. (2.12)). Both relations express equilibrium concentrations as a property of the solid via the exponential of the crystal chemical potential μ_{GaAs}. This expression will be of fundamental importance in modeling the drilling of Ga droplets into solid GaAs (Chapter 5).

2.1.3 Thermodynamics of the Bulk GaAs Crystal at its Surface

Having analyzed the thermodynamics of adatoms and of liquid Ga droplets, it is now the thermodynamics of the bulk GaAs crystal that is left to consider. The basic quantity to consider is the change in free energy when adding a Ga-As pair to the solid, i.e., the crystal chemical potential μ_{GaAs}. To first approximation, μ_{GaAs} is simply the free energy of formation of solid GaAs per unit cell, that is, $\mu_{\mathrm{GaAs}} = g_{\mathrm{GaAs}}$. However, in some contexts (as in Chapter 5) it is important to take into account the surface free energy per unit surface area $\gamma(\mathbf{n})$, which generally depends on the orientation of the surface $\mathbf{n}$ (the unit normal), as it is at the crystal surface where the Ga and As atoms attach to the solid. Let us now consider the surface excess chemical potential, $\Delta\mu_{\mathrm{GaAs}}$, associated to the surface free energy $\gamma(\mathbf{n})$.

The surface free energy of a crystal is the integral $\int \gamma(\mathbf{n}) dS$, extending across the whole surface of the crystal. Then the change in surface free energy upon adding an infinitesimal crystal hump at a point on the surface is [59]

$$\delta \int \gamma \, dS = \int \delta\gamma \, dS_0 + \int \gamma \delta \, dS, \tag{2.24}$$

where dS_0 is the area element of the original surface and $dS_0 + \delta dS$ is the area element of the final surface, and $\delta\gamma$ is related to the change in surface orientation upon adding the hump. It is shown in Ref. [59] that the first and second terms of Eq. (2.24) are

$$\int \delta\gamma \, dS_0 = \left(\frac{\partial^2 \gamma}{\partial n_x^2} . \frac{1}{R_x} + \frac{\partial^2 \gamma}{\partial n_y^2} . \frac{1}{R_y} \right) \delta v \tag{2.25}$$

and

$$\int \gamma \delta dS = \gamma \left(\frac{1}{R_x} + \frac{1}{R_y} \right) \delta v, \tag{2.26}$$

where δv is the change in volume of the hump, $1/R_x$ and $1/R_y$ are the principal curvatures in two perpendicular directions (the x and y axes of the tangent plane at the point in question), and n_x and n_y are the projections of the variable vector $\mathbf{n}$ on the x and y directions of the tangent plane. The contribution of the surface free energy $\gamma(\mathbf{n})$ to the GaAs crystal chemical potential is usually given in more general

tensor notation [60–62], i.e.

$$\Delta\mu_{\mathrm{GaAs}} = \Omega_{\mathrm{GaAs}} \left(\gamma(\mathbf{n})\kappa + \frac{\partial^2 \gamma(\mathbf{n})}{\partial \mathbf{n}^2} . \boldsymbol{\kappa} \right), \tag{2.27}$$

where Ω_{GaAs} is the volume of a primitive cell of GaAs, $\boldsymbol{\kappa}$ is the surface curvature tensor, defined as $\boldsymbol{\kappa} = -\nabla_S \mathbf{n}$ (where $\mathbf{n}$ is the outward pointing unit normal and ∇_S is the surface gradient), κ is the trace of the curvature tensor, and $\frac{\partial^2 \gamma}{\partial \mathbf{n}^2} . \boldsymbol{\kappa}$ is the scalar contraction of $\partial^2\gamma/\partial\mathbf{n}^2$ and $\boldsymbol{\kappa}$.

In Chapter 5, however, we will only consider the case of isotropic surface energy $\gamma(\boldsymbol{n}) = \gamma$ for simplicity. This simplifies Eq. (2.27) to just

$$\Delta\mu_{\mathrm{GaAs}} = \Omega_{\mathrm{GaAs}}\gamma\kappa. \tag{2.28}$$

If the surface is also subjected to a finite pressure p, the change in volume term in the Gibbs free energy (see Eq. (2.1)) upon raising the hump is $p\delta v$, and so $\Delta\mu_{\mathrm{GaAs}}$ will contain a term $p\,\Omega_{\mathrm{GaAs}}$ [62]. The total crystal chemical potential μ_{GaAs} is then the bulk plus the surface contributions, that is

$$\mu_{\mathrm{GaAs}} = g_{\mathrm{GaAs}} + \Delta\mu_{\mathrm{GaAs}} = g_{\mathrm{GaAs}} + \Omega_{\mathrm{GaAs}}\,(\gamma\kappa + p) \tag{2.29}$$

We will use Eq. (2.29) in Chapter 5 in modeling the drilling of Ga droplets into solid GaAs. In particular, note that substituting Eq. (2.29) into Eq. (2.23) gives an equilibrium As mole fraction μ_{As}^{eq} that depends on position. This is essential in producing the nanohole morphologies that are shown in Chapter 5.

2.2 Kinetics at GaAs(001) Surfaces

Having reviewed the thermodynamic concepts and quantities associated to GaAs surfaces, we now turn to the kinetic aspects of processes occurring at these surfaces. The nano and atomic-scale details of growth and other processes such as evaporation are known to be of considerable complexity. These include attachment and detachment of adatoms at surface steps [56], nucleation of new terraces [63], diffusion [39],

desorption [38] etc. It is out of the scope of this thesis to model the kinetics of GaAs surfaces so as to include each and every phenomenon involved in a given process (such as growth). Rather, we formulate simple kinetic models that encapsulate the major features of the ongoing processes, and that produce sufficiently satisfying results within a self-consistent framework.

In Chapter 3, as we will see, we simply measure (as a function of the sample temperature T) the rates of the main processes observed in our LEEM videos, such as the velocity v of the evaporating steps, and then fit these to Arrhenius temperature-dependences, i.e., $v = v_0 \exp(-E/kT)$ where v_0 is a pre-factor, E is an energy barrier, and k is the Boltzmann constant. Then the fitted rates of the main processes are fed into a Monte Carlo simulation code whose outcome is then compared to experiment without delving into the physics of the ongoing rate processes. In Chapter 4, however, we consider a basic reaction-diffusion model for the Ga detaching from a Ga droplet and reacting with an incoming As flux. We utilize the simple concepts explained above in Section 2.1.1 to model the collective reaction-diffusion process performed by surface Ga as it reacts with the As being deposited and more Ga is supplied by the droplets. As we will see, the model produces Ga adatom chemical potential gradients $\mu_{\mathrm{Ga}} = \mu_{\mathrm{Ga}}(r)$ from the droplet edge, that serve to explain surface phase patterns observed experimentally. In Chapter 5 we model the net mass exchange between the solid with chemical potential μ_{GaAs} as per Eq. (2.29), and the Ga droplet and adatom population. As we will see, different points on the surface will have different growth rates, producing non-trivial surface morphologies as the Ga droplet and surface are subjected to the As flux. In this section we will explain the origin of the kinetic concepts used in Chapters 4 and 5.

Let us assume a GaAs(001) surface, in some instances with nano/microscale Ga droplets (of radii $0.1\mu\mathrm{m} \rightarrow 1\mu\mathrm{m}$) distributed across it. In general the surface will be subjected to an As flux, F_{As}, which is the number of As atoms that arrive at the surface per unit surface area and time. In pratice, it is well known that As fluxes in MBE are usually dimers (As_2) or tetramers (As_4), in most cases the latter. However, the chemistry of As molecules on a GaAs(001) surface is relatively complex [26–28],

so we will assume, for the sake of simplicity, that As is present on the surface in the form of monomers, and we will consider an As monomer flux F_{As} per unit area and time. We consider Ga and As adatoms on the surface, as explained in Section 2.1.1. These are supplied by the Ga droplets, the As flux, and the bulk solid. The adatoms may diffuse, attach to a droplet, evaporate into the vacuum or react to form GaAs. Each of these kinetic processes occurs at a certain rate, and it is the combined effect of these rate processes what produces an overall mechanism of interest, such as the surface phase boundary dynamics which we will explore in Chapter 4, or the the nanohole drilling which we will study in Chapter 5. It is therefore important to consider the rates of each of these kinetic processes, as we will do in the following.

We consider Ga and As adatoms are present on the surface at concentrations C_{Ga} and C_{As} (i.e., number of adatoms per unit surface area). These can, of course, vary spatially (for example, with distance to a droplet), and in time (when opening/closing the As flux). We will now consider the rates of the different processes for a generic adatom (Ga or As).

- **Adatom desorption** Starting with desorption, it is usually considered that an adatom will desorb from the surface at a rate (or with probability per unit time) k_d. Desorption being a thermally activated process, its rate will depend upon temperature T according to the Arrhenius relation $k_d = f\exp(-E_d/kT)$, where f is the attempt frequency (of the order of atomic frequency of vibration), and $\exp(-E_d/kT)$ is the fraction of times the attempts to desorb 'succeed'. E_d is the potential barrier to be overcome by the adatom in order to detach from the surface (also called the 'activation energy'), k is the Boltzmann constant, and T is the absolute temperature. The Arrhenius factor $\exp(-E_d/kT)$ is a growing function of temperature. This can be interpreted as that the activation energy is more easily overcome by thermal excitation as the sample temperature is increased. If we now consider the total rate of adatom evaporation per unit area from a surface, this will be $k_d\,C$, where C is the adatom concentration. It can easily be shown that the average lifetime τ of an adatom before desorption from the surface relates to k_d simply as $k_d = 1/\tau$,

and so we have that the rate of evaporation per unit surface area is

$$\frac{C}{\tau}, \tag{2.30}$$

as is frequently seen in the literature.

- **Adatom Diffusion** Similarly, an adatom may 'hop' to a neighbouring lattice site with a frequency k_{diff}. As in the case of evaporation, diffusion is a thermally activated process and its frequency is assumed to have an Arrhenius temperature-dependence, i.e., $k_{diff} = f_{diff}\exp(-E_{diff}/kT)$, where f_{diff} is the attempt frequency, and E_{diff} is the activation energy. It can be shown [64] that the mean square displacement $\langle \mathbf{r}^2 \rangle$ after a time t of an atom that diffuses randomly along the surface hopping at a rate k_{diff} is $\langle \mathbf{r}^2 \rangle = l^2 k_{diff} t$, where l is the distance between neighboring sites. From this expression the tracer diffusion coefficient D^* is defined, as $D^* = l^2 k_{diff}/4$, so that $\langle \mathbf{r}^2 \rangle = 4D^* t$. Parallel to this random walk concept of diffusion is the macroscopic version, which is expressed by Fick's law. It states that given an adatom concentration gradient ∇C, there will be a net adatom diffusion current $\mathbf{J}$ so as to homogenize the adatom concentration and proportional to the concentration gradient, i.e.,

$$\mathbf{J} = -D\nabla C. \tag{2.31}$$

This expression is Fick's Law, and it defines the macroscopic or chemical diffusion coefficient D. The number of adatoms per unit time diffusing through a length element $\mathbf{ds}$ in the direction pointed by $\mathbf{ds}$ ($\mathbf{ds}$ pointing perpendicularly to the line element ds) is then the dot product $\mathbf{J}.\mathbf{ds}$. It can be shown that for low adatom coverages, i.e. low number of adatoms relative to the number of lattice sites (as we assume throughout), the tracer and the chemical diffusion coefficients are equal, i.e., $D = D^*$. Therefore, the chemical diffusion coefficient D from Fick's law will effectively have an Arrhenius temperature-dependence $D = D_0 \exp(-E_{diff}/kT)$, where $D_0 = l^2 \nu_{diff}/4$ and E_{diff} is the activation energy for hopping from one site to a neighbor site. In Chapters 4

and 5 we consider continuum models for adatoms and the GaAs(001) surface, and so we will employ Fick's law of diffusion as per Eq. (2.31).

- **Adatom Reaction (GaAs growth)** Probably the most relevant kinetic process of all is that of GaAs growth. As mentioned earlier, crystal growth is a rather complex matter, and several mechanisms such as island nucleation and adatom attachment to steps may be at play all at once. Here we simply assume that growth occurs as a consequence of the encounter and reaction of a Ga atom and an As atom at a lattice site, to form a GaAs 'molecule' at the surface, i.e., Ga + As $\rightarrow$ GaAs. The frequency of encounters of a Ga and a As adatom at given site will be proportional to the product of the adatom concentrations $C_{\mathrm{Ga}}C_{\mathrm{As}}$. The total number of reactions per unit area and time is thus

$$k_r C_{\mathrm{Ga}} C_{\mathrm{As}}, \tag{2.32}$$

where k_r is a non-trivial, temperature-dependent reaction rate constant containing the density of sites for reaction.

Eq. (2.32) gives the rate of reaction of Ga and As to form GaAs. However, we are interested in the *net* rate of GaAs growth. Therefore we must take into account the rate at which the bulk solid decomposes into Ga and As adatoms, i.e., GaAs $\rightarrow$ Ga + As, and subtract it from Eq. (2.32). The net rate of growth, R_{gr}, is thus

$$R_{gr} = k_r C_{\mathrm{Ga}} C_{\mathrm{As}} - R_{dec}, \tag{2.33}$$

where R_{dec} is the rate of GaAs decomposition. Writing the adatom concentrations of Eq. (2.33) in terms of chemical potential, as per Eq. (2.9) we get

$$R_{gr} = k_r \nu_{\mathrm{Ga}} \nu_{\mathrm{As}} \exp\left(\frac{\mu_{\mathrm{Ga}} + \mu_{\mathrm{As}} - E_{\mathrm{Ga}} - E_{\mathrm{As}}}{kT}\right) - R_{dec}. \tag{2.34}$$

In such a way as the rate of the Ga + As $\rightarrow$ GaAs reaction depends upon the adatom chemical potentials μ_{Ga} and μ_{As}, the rate of the backward reaction GaAs $\rightarrow$ Ga + As should depend upon the crystal chemical potential μ_{GaAs}.

Applying what is known as the *principle of detailed balance*, which essentially states that in equilibrium, the net rate of the process ought to be zero, we have that when the adatom population is in equilibrium with the solid, i.e., when $\mu_{\mathrm{Ga}} + \mu_{\mathrm{As}} = \mu_{\mathrm{GaAs}}$, then $S = 0$. Substituting these into Eq. (2.34) yields

$$R_{dec} = k_r \nu_{\mathrm{Ga}} \nu_{\mathrm{As}} \exp\left(\frac{\mu_{\mathrm{GaAs}} - E_{\mathrm{Ga}} - E_{\mathrm{As}}}{kT}\right). \tag{2.35}$$

We can then write the net rate of growth of Eq. (2.34) as

$$R_{gr} = k_r \nu_{\mathrm{Ga}} \nu_{\mathrm{As}} \left[\exp\left(\frac{\mu_{\mathrm{Ga}} + \mu_{\mathrm{As}} - E_{\mathrm{Ga}} - E_{\mathrm{As}}}{kT}\right) - \exp\left(\frac{\mu_{\mathrm{GaAs}} - E_{\mathrm{Ga}} - E_{\mathrm{As}}}{kT}\right)\right]. \tag{2.36}$$

We can also write Eq. (2.36) in terms of adatom concentrations as

$$R_{gr} = k_r \left[C_{\mathrm{Ga}} C_{\mathrm{As}} - (C_{\mathrm{Ga}} C_{\mathrm{As}})_{eq}\right], \tag{2.37}$$

where we recall the expression for the equilibrium product of adatom concentrations $(C_{\mathrm{Ga}} C_{\mathrm{As}})_{eq}$ of Eq. (2.12). These expressions for the net rate of GaAs growth will be employed in Chapters 4 and 5 to model the motion of surface phase boundaries on GaAs(001) and the evolution of the GaAs(001) surface during droplet etching, respectively.

- **GaAs growth at the Ga liquid/GaAs solid interface** Similarly, we may derive an analogous expression for growth at the liquid-solid interface of a Ga droplet and the GaAs(001) substrate. Given the low As content in a Ga droplet, the frequency with which an As atom dissolved in the droplet will arrive upon a lattice site at the interface will simply be proportional to be As content x_{As}. At that point the As atom is able to react with one of the numerous Ga atoms surrounding it to form solid GaAs, as per Ga + As $\rightarrow$ GaAs. Similarly, the GaAs substrate may dissolve into Ga and As a per GaAs $\rightarrow$ Ga + As. Reasoning analogously as for the case of the adatoms, the

net rate of the forward (growth) reaction per unit surface area will be

$$R_{gr} = k_l \left(x_{\mathrm{As}} - x_{\mathrm{As}}^{eq} \right), \tag{2.38}$$

where k_l is a rate constant, and x_{As}^{eq} is the As mole fraction of equilibrium with the solid, as given by Eq. (2.23). This expression will be of use in modeling the dynamics of droplet etching in Chapter 5.

- **Continuity equations for adatoms on GaAs** Here we will now derive a mass balance or continuity equation for adatoms undergoing the above-explained processes of diffusion, desorption and reaction. We will consider Ga adatoms, but the same concepts apply to As. If we consider a region of the surface contained within a closed loop with length element **ds** (outward pointing), the net rate of change of Ga atoms within the loop will be given by

$$\frac{d}{dt} \int C_{\mathrm{Ga}} dA = - \int \mathbf{J}.\mathbf{ds} + \int \left[-k_r \left[C_{\mathrm{Ga}} C_{\mathrm{As}} + (C_{\mathrm{Ga}} C_{\mathrm{As}})_{eq} \right] - \frac{C_{\mathrm{Ga}}}{\tau_{\mathrm{Ga}}} + F_{\mathrm{Ga}} \right] dA, \tag{2.39}$$

where dA is the surface area element enclosed within the loop, $\mathbf{J}$ is the Ga adatom current given by $\mathbf{J} = -D_{\mathrm{Ga}} \nabla C_{\mathrm{Ga}}$, and F_{Ga} is the Ga flux arriving upon the surface (number of atoms per unit area and time). The $\int \mathbf{J}.\mathbf{ds}$ accounts for Ga adatoms diffusing out of the loop, and the rest of terms within the area integral account for the Ga adatoms being lost by reaction with As, desorption from the surface, and those being adsorbed on the surface by the incoming flux. Applying the divergence theorem to the closed loop integral $\int \mathbf{J}.\mathbf{ds}$ we have $-\int \mathbf{J}.\mathbf{ds} = \int D_{\mathrm{Ga}} \nabla^2 C_{\mathrm{Ga}} dA$, and pulling the time derivative on the left hand side inside the integral, we have

$$\int \frac{\partial C_{\mathrm{Ga}}}{\partial t} dA = \int \left[D_{\mathrm{Ga}} \nabla^2 C_{\mathrm{Ga}} - k_r \left[C_{\mathrm{Ga}} C_{\mathrm{As}} + (C_{\mathrm{Ga}} C_{\mathrm{As}})_{eq} \right] - \frac{C_{\mathrm{Ga}}}{\tau_{\mathrm{Ga}}} + F_{\mathrm{Ga}} \right] dA. \tag{2.40}$$

As Eq. (2.40) applies for any closed loop, we ought to have

$$\frac{\partial C_{\mathrm{Ga}}}{\partial t} = D_{\mathrm{Ga}} \nabla^2 C_{\mathrm{Ga}} - k_r \left[C_{\mathrm{Ga}} C_{\mathrm{As}} + (C_{\mathrm{Ga}} C_{\mathrm{As}})_{eq} \right] - \frac{C_{\mathrm{Ga}}}{\tau_{\mathrm{Ga}}} + F_{\mathrm{Ga}}. \tag{2.41}$$

Eq. (2.41) is the mass balance equation for surface Ga. We will use it in Chapter 4 to describe phase boundary dynamics on GaAs(001) in the vicinity of a Ga droplet. Usually during droplet epitaxy, no Ga flux is used $F_{\mathrm{Ga}} = 0$ and the temperatures are low enough ($300 - 500°\mathrm{C}$) to make evaporation of Ga negligible, i.e., $C_{\mathrm{Ga}}/\tau_{\mathrm{Ga}} \approx 0$. This leaves

$$\frac{\partial C_{\mathrm{Ga}}}{\partial t} = D_{\mathrm{Ga}} \nabla^2 C_{\mathrm{Ga}} - k_r \left[C_{\mathrm{Ga}} C_{\mathrm{As}} + (C_{\mathrm{Ga}} C_{\mathrm{As}})_{eq} \right], \tag{2.42}$$

for standard droplet epitaxy experiments.

- **Ga adatom attachment and detachment from a Ga droplet**

  Last but not least we must consider Ga exchange between a droplet and the adatom population. Ga adatoms diffusing along the GaAs(001) surface may encounter a Ga droplet and attach to it at the droplet contact line, thereby becoming part of the Ga droplet. If we consider a length element of the contact line, the frequency of Ga adatoms making contact with the droplet at that line element will be proportional to the Ga adatom concentration C_{Ga}. Therefore, the rate of Ga adatom attachment to a droplet, per unit contact line length is

$$k_D \, C_{\mathrm{Ga}}, \tag{2.43}$$

  where k_D is a temperature-dependent rate constant. Again, we are interested in the *net* rate of Ga attachment to the droplet, so we must consider the rate at which Ga from the droplet detaches from the contact line and becomes Ga adatoms. Applying again the principle of detailed balance, analogously as done previously with GaAs growth in Eq. (2.33), we get that the net rate of Ga attachment to a Ga droplet (per unit contact line length) is

$$k_D \left(C_{\mathrm{Ga}} - C^l_{\mathrm{Ga}} \right), \tag{2.44}$$

  where C^l_{Ga} is the Ga adatom concentration of equilibrium with liquid Ga, i.e., the adatom concentration that makes the adatom chemical potential μ_{Ga} equal

the chemical potential of Ga in the droplet. Using the relation between adatom chemical potential and adatom concentration of Eq. (2.10), C^l_{Ga} writes

$$C^l_{\mathrm{Ga}} = \nu_{\mathrm{Ga}} \exp\left(\frac{g^l_{\mathrm{Ga}} - E_{\mathrm{Ga}}}{kT}\right), \tag{2.45}$$

where we assume that the chemical potential of Ga in the droplet is simply the free energy per atom of formation pure liquidus Ga g^l_{Ga}, as done previously in Eq. (2.22), and in line with the assumption of low As solubility in Ga droplets.

As we will see in Chapter 4, the above-explained concepts of Ga attachment-detachment at the droplet contact line will serve to set a boundary condition for the reaction-diffusion governing the Ga adatoms on the surface (see Eq. (2.42)). Arsenic exchange between the droplets and the surface is neglected because of the low As content in Ga droplets and to the short diffusion length of As adatoms at temperature above 300°C (due to the short residence time τ_{As} before desorption above these temperatures).

2.3 GaAs(001) Surface Phases and their Stability

Understanding the structure of GaAs(001) surfaces is paramount in investigating the mechanisms of epitaxial growth [65]. Therefore, a lot of effort has been devoted to investigating the atomic structure of these surfaces under UHV conditions [1, 2, 29, 66–76]. By means of *in situ* diffraction techniques such as RHEED, GaAs(001) surfaces have been observed to display a variety of periodicities at the atomic scale. Let us now consider the origin of these surface periodicities.

A nominal (001) surface, as shown in Fig. 2.2, be it As terminated or Ga terminated will have 'dangling' bonds, i.e., the uppermost atoms will be left with unsaturated bonds. Such configurations are energetically unfavorable. Surfaces can thus present atomic configurations different to that corresponding to the bulk solid, in which the unsaturated bonds are filled as best as possible. Such structures are called surface reconstructions or surface phases, and the surface will generally exhibit the reconstruction that minimizes the system's free energy. However, the stability

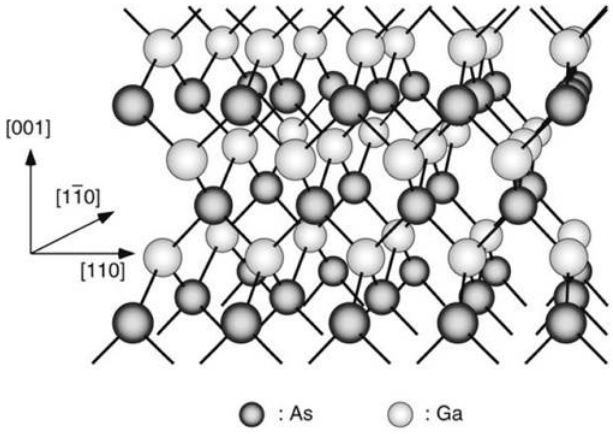

Figure 2.2: Schematic diagram of a GaAs crystal. As can be seen, it can be viewed as a sequence of Ga and As layers along the (001) direction. The atoms of the uppermost layer are left with two dangling bonds each. Reprinted from Ref. [1]

.

of the surface phases generally depends upon the experimental conditions (T and ambient stoichiometry), so under different conditions, minimized free energy may be reached by a different reconstruction. It is then usual to observe phase transitions upon changing the conditions in the growth chamber.

The reconstruction the surface presents is of critical importance to crystal growth, as the growth mechanism will be completely different on two different reconstructions [65]. Under the conditions in which MBE growth of GaAs(001) is usually performed ($T \approx 580$°C and high As to Ga flux ratios) the surface exhibits the (2×4) reconstruction, but there are many other reconstructions of the GaAs(001) surface. Chapters 3 and 4 present experimental and theoretical work on the stability of the different phases of GaAs(001). In this section we will introduce the most relevant surface phases of the GaAs(001) surface and we will elaborate on the concept of surface phase stability.

Surface phases are usually named after their periodicity relative to that of the bulk crystal [77]. The (2×4) reconstruction is named in such a way because the unit cell of the surface lattice is 4 times larger than the periodicity of the underlying bulk lattice in the [1 1 0] direction, and 2 times larger than the underlying bulk periodicity in the [1 $\bar{1}$ 0] diretion (which is perpendicular to the [1 1 0] direction). [77]. Fig. 2.3 shows a schematic of the atomistic details of the $\beta2(2 \times 4)$ model. There are more models of the (2×4) reconstruction (hence the $\beta2$ prefix), but the $\beta2(2 \times 4)$ is

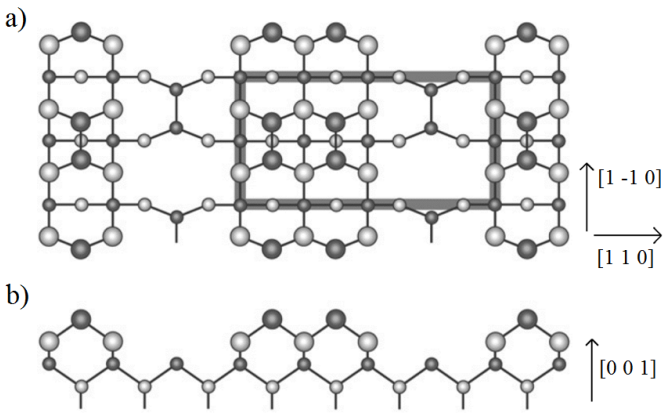

Figure 2.3: Schematic diagrams of the $\beta 2(2\times 4)$ model reconstruction. a) is a birds-eye view of the surface, while b) is a cross-section with the [1 -1 0] direction pointing into the page. The dark circles represent As atoms, while the light circles represent Ga atoms. Reprinted from Ref. [1].

the best accepted of them all. Fig. 2.3a) shows a bird's eye view of the surface, with the (2×4) unit cell marked on it, while Fig. 2.3b) shows a profile of the surface along the $[1\ \bar{1}\ 0]$ direction. As can be seen, the major characteristics of the $\beta 2(2 \times 4)$ reconstruction are, firstly, that it is an As-terminated surface. Second, it has monolayer-deep trenches along the $[1\ \bar{1}\ 0]$ direction of the surface, and, thirdly, the As rows in the trenches and upon the crests dimerize along the $[1\ \bar{1}\ 0]$ in order to saturate the dangling bonds. As mentioned earlier, this reconstruction is of great technological importance, as it is the one that is usually prepared for MBE homoepitaxy on GaAs(001). There are however many more reconstructions of the GaAs(001) surface. Probably the best-known ones are the As-rich $c(4 \times 4)$ and the Ga-rich $c(8 \times 2)$ phases.

At standard growth temperatures ($T \approx 580°\mathrm{C}$), the (2×4) reconstruction can generally be seen under As-flux. However, in the absence of flux, it is usually the $c(8 \times 2)$ phase that is present at such temperatures [4]. This manifests clearly that phase stability on GaAs(001) depends upon the Ga-As ambient stoichiometry in the growth chamber. This phenomenon is explained within the context of surface thermodynamics and phase diagrams. Now we will explain the basic elements of phase stability of GaAs(001). A more detailed explanation can be found in Ref. [78].

Let us consider a GaAs(001) slab in contact with reservoirs of Ga and As at chemical potentials μ_{Ga} and μ_{As} respectively. In practice these reservoirs can be

thought of as the ambient vapour in the chamber. The fact that they are reservoirs means that they can exchange Ga and As atoms with the slab without the reservoir chemical potentials being affected. Let us suppose that the GaAs slab presents a certain reconstruction that we take as a reference reconstruction (say the $\beta 2(2\times 4)$ reconstruction for instance). The free energy of the system G is then the free energy of the slab plus the free energy of the reservoirs, that is

$$G = G_{slab} + N_{\mathrm{Ga}}^{res}\mu_{\mathrm{Ga}} + N_{\mathrm{As}}^{res}\mu_{\mathrm{As}}, \tag{2.46}$$

where N_{Ga}^{res} and N_{As}^{res} are the (very large) number of Ga and As atoms contained in either reservoir.

Let us consider now that we take ΔN_{Ga} Ga atoms from the Ga reservoir, as well as ΔN_{As} atoms from the As reservoir and place them on the surface to produce a different reconstruction (say the $c(8\times 2)$ reconstruction). The change in the system's free energy will thus be

$$\Delta G = \Delta G_{slab} - \Delta N_{\mathrm{Ga}}\,\mu_{\mathrm{Ga}} - \Delta N_{\mathrm{As}}\,\mu_{\mathrm{As}}. \tag{2.47}$$

This equation enables us to analyze the relative stability of either phase for given ambient conditions, i.e., given μ_{Ga} and μ_{As}. If $\Delta G < 0$ then the new phase is the more stable one of the two, and if $\Delta G > 0$ then the original phase is the more stable one of the two. However, such conditions may change for different values of the ambient chemical potentials μ_{Ga} and μ_{As}. For simplicity we assume that the reservoirs are in equilibrium with the bulk GaAs crystal, i.e., $\mu_{\mathrm{Ga}} + \mu_{\mathrm{As}} = g_{\mathrm{GaAs}}$, where g_{GaAs} is the free energy of formation per unit cell of bulk GaAs. This leaves only one free parameter (μ_{Ga} for instance). Substituting the equilibrium condition into Eq. (2.47) yields

$$\Delta G = \Delta G_{slab} - \Delta N_{\mathrm{As}}\,g_{\mathrm{GaAs}} + (\Delta N_{\mathrm{As}} - \Delta N_{\mathrm{Ga}})\mu_{\mathrm{Ga}}. \tag{2.48}$$

Therefore, knowing ΔG_{slab}, g_{GaAs} and the difference in stoichiometry ΔN_{Ga} and ΔN_{As} between either phase, Eq. (2.48) provides and indicator of the relative stability

of either phases, as a function of ambient μ_{Ga}. In practice Eq. (2.48) is used per unit surface area, so that ΔG and ΔG_{slab} are free energies per unit area, and ΔN_{Ga} and ΔN_{As} number of atoms per unit area.

This is exactly the approach taken by researchers of the GaAs(001) reconstructions. Atomistic models are proposed for the different reconstructions observed experimentally. One of the reconstructions is usually taken as reference, and the difference in free energy of each reconstruction relative to the reference is computed via Eq. (2.48). For simplicity, the T-dependence of ΔG_{slab}, g_{GaAs} is usually neglected and total energies are used instead. Those are the difference in formation energy ΔE_{slab} per unit area of either slab, and the formation energy E_{GaAs} per unit cell of bulk GaAs, respectively. This is equivalent to assuming a GaAs(001) at absolute zero, i.e., at $T = 0$K. Eq. (2.48) then reads

$$\Delta G = \Delta E_{slab} - \Delta N_{\mathrm{As}}\, E_{\mathrm{GaAs}} + (\Delta N_{\mathrm{As}} - \Delta N_{\mathrm{Ga}})\mu_{\mathrm{Ga}}. \tag{2.49}$$

Researchers compute the difference in formation energy of either slab ΔE_{slab} via Density Functional Theory (DFT) methods. A ΔG versus μ_{Ga} linear function is then defined for each phase, where $\Delta N_{\mathrm{As}} - \Delta N_{\mathrm{Ga}}$ is the gradient and $\Delta E_{slab} - \Delta N_{\mathrm{As}} E_{\mathrm{GaAs}}$ is the y-intercept. The ΔG versus μ_{Ga} lines may then be plotted on a phase diagram at $T = 0$K as that shown in Fig. 2.4.

Phase diagrams like that of Fig. 2.4 provide a clear explanation as to the dependence of the the GaAs(001) surface phases with ambient stoichiometry in the growth chamber. For given μ_{Ga}, the stable reconstruction will be that that minimizes the free energy ΔG. Under As-rich conditions, for example at $\mu_{\mathrm{Ga}} = -0.6\,\mathrm{eV}$ in Fig. 2.4, the equilibrium phase will be the $c(4\times4)\beta$ reconstruction. As μ_{Ga} is increased, there comes a point where the $c(4\times4)\beta$ line crosses the $\beta2(2\times4)$, and the latter becomes the stable phase. Experimentally, one would observe a phase transition upon reaching this crossover point. As μ_{Ga} is increased further, first $c(8\times2)$ becomes the equilibrium phase and eventually the (4×6) phase does so. As can be observed, the stable phases at higher μ_{Ga} have a more negative gradient $\Delta N_{\mathrm{As}} - \Delta N_{\mathrm{Ga}}$ on the phase diagram, i.e, Ga-richer ambient conditions favor Ga-richer reconstructions,

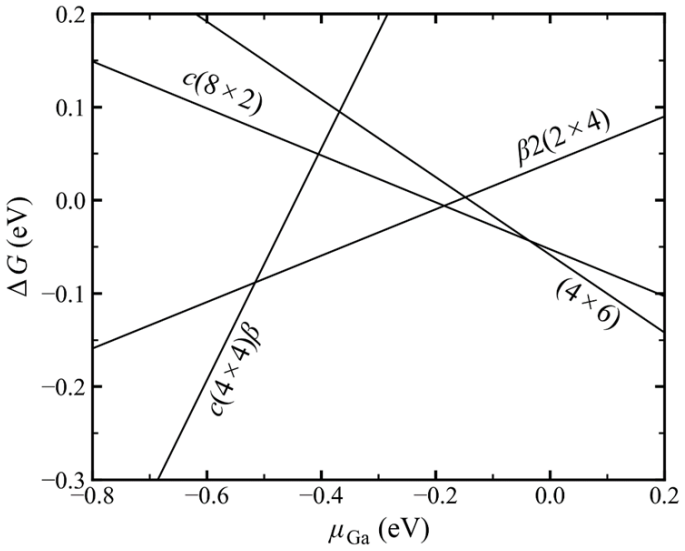

Figure 2.4: DFT-calculated surface phase diagram plotting free energy ΔG versus ambient Ga chemical potential μ_{Ga} for four important reconstructions of the GaAs(001) surface at $T = 0$K. ΔGs are with respect to the $\alpha 2(2 \times 4)$ surface and are computed per unit (1×1) cell. This has been adapted from Ref. [2].

and As-richer conditions favor As-richer reconstructions.

The transition from $c(8 \times 2)$ to $\beta 2(2 \times 4)$ upon opening the As flux to prepare the surface for growth can now be explained. At growth temperatures ($T \approx 580°$C), As evaporates readily from the surface, i.e., the lifetime before desorption τ_{As} for As adatoms is a lot smaller than the lifetime before desorption τ_{Ga} for Ga adatoms. This leaves behind a Ga-rich adatom population on the GaAs surface, i.e., a high ambient μ_{Ga}. For this reason the Ga-rich $c(8 \times 2)$ surface is observed at these temperatures. However, on turning on the As flux the As adatom population on the GaAs surface increases and hence μ_{As} increases. The numerous As adatoms react with the Ga adatoms and hence the Ga density decreases. The ambient μ_{Ga} is hence decreased, which takes us to the left on the phase diagram of Fig. (2.4). Under these As-richer (or Ga-poorer) conditions the $\beta 2(2 \times 4)$ reconstruction becomes the one that minimizes the free energy, and is hence the equilibrium reconstruction for these conditions.

In summary, phase stability on the GaAs(001) surface depends upon the ambient stoichiometry to which the surface is exposed to. Ga-rich phases are observed under Ga-rich conditions and As-rich phases are seen under As-rich conditions. Concretely, the stable phase is the one that minimizes the system's free energy for given

conditions. The effects of finite temperature such as configurational entropy or vibrational modes of the different reconstructions are neglected in DFT computations, and therefore phase diagrams describe surfaces at $T = 0$K. Interestingly, in Chapter 3 we will explain our findings of a novel phenomenon where, using LEEM, we observe metastable domains of a (6×6) phase aside the stable $c(8 \times 2)$ phase on heating the GaAs(001) surface under vacuum above $\sim 580°$C, where we would expect to see the $c(8 \times 2)$ reconstruction only. As we will see, this is due to the fact that evaporation of GaAs(001) into the vacuum becomes important at these temperatures. Additionally, we will see in Chapter 4 how finite temperature (entropic) effects do affect the GaAs(001) phase diagram, and we superimpose the lines of (6×6) and (3×6) phases given some interesting experimental results in our LEEM-MBE system.

2.4 Experimental Methods

In this section we will introduce the main experimental techniques that were used in this work. The key experiments were performed in an ultrahigh-vacuum (UHV) low energy electron microscope (LEEM), especially modified for III-V MBE. We will first explain the basic general principles of the LEEM technique. Then we will introduce the components of our LEEM-MBE system. After this we will explain our method for planarizing the GaAs(001) surface before observing it with LEEM. Last we will explain a novel technique developed in our laboratory that exploits so called 'dark-field' imaging to spatially resolve and identify regions of the GaAs(001) surface exhibiting different surface reconstructions. This technique is the essence of the experimental results of Chapters 3 and 4.

2.4.1 The LEEM Technique

Low energy electron microscopy (LEEM) is a technique that is highly suited for surface science of electrically conducting crystals under growth conditions. In this Section we will review the basic concepts of the LEEM principle and how these make the unique characteristics of the technique. More detail can be found in Ref. [3].

In LEEM, electron emission is stimulated by a coherent, monoenergetic electron

beam that is incident on the surface at normal angle. This beam is originated by an electron gun and is accelerated to the microscope potential (typically around $15 \rightarrow 20$ keV). Before impinging upon the sample, the electron beam is collimated by a series of apertures and lenses in the illumination column. It then passes through the beam separator. This component contains a magnetic field that deflects the beam and directs it toward the sample. The beam is then focused to a point on the back focal plane of the objective lens. In the objective, the beam is focused to a parallel beam and is de-accelerated to the desired incident energy (typically below 30 eV). According to the curve of electron mean free paths in inorganic compounds [79], the penetration depth of electrons impinging on the surface at 10 eV is around 20 monolayers. When tuning the electron energy up to 50 eV, the penetration depth goes as low as ≈ 3.5 monolayers. For higher energies than these, the electron mean free path rises monotonically. This makes LEEM a surface-sensitive technique. A schematic diagram summarising the LEEM principle is shown in Fig. 2.5.

The backscattered electrons are then reaccelerated to the microscope potential and are focused by the objective. In the case of a crystalline sample, electrons will be diffracted and thus backscattered at specific angles. Electrons emitted at the same angle will be focused to the same point in the back focal plane. This produces diffraction patterns on the back focal plane. The reflected beam is deflected into the imaging column by the beam separator and, after passing through a series of lenses an image is formed after impinging on a microchannel plate image intensifier and a phosphor screen.

Either the whole diffraction pattern may be viewed, or one of the diffracted beams could be selected using a contrast aperture. The former mode would be low energy electron diffraction (LEED), and the latter would be LEEM imaging. When the specular or (00) spot is filtered, the imaging is named bright-field imaging, as this beam tends to be the more intense. However, another of the diffracted beams may be filtered instead. This kind of imaging is named dark-field imaging, and, as we will see in Chapters 3 and 4 it is a useful tool to spatially resolve and identify areas of the surface with different surface structures.

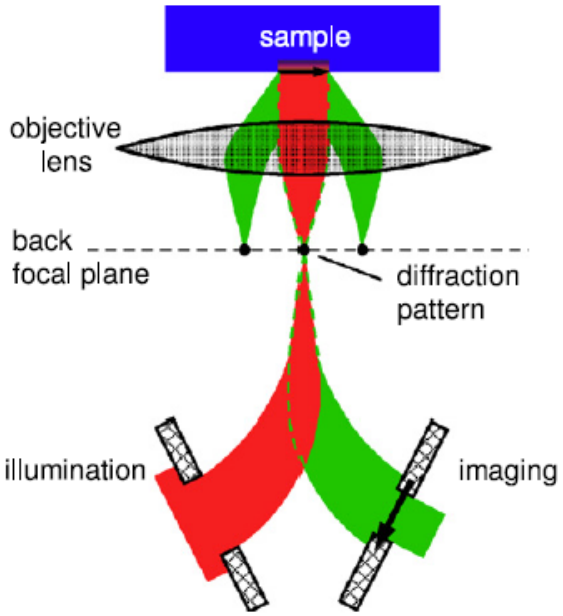

Figure 2.5: Schematic diagram explaining the LEEM technique. Reprinted from Ref. [3]

In contrast to the widely practiced scanning electron microscopy (SEM), LEEM is a non-scanning technique, in which information is obtained simultaneously at every point in the image. Furthermore, given the low energy of the incident electrons, the reflected intensity is very high. This enables the acquisition of real-time *in-situ* imaging at video rates, which is probably the trademark characteristic of the LEEM technique.

LEEM/LEED also offers several advantages over the more conventional reflection high energy electron diffraction (RHEED) technique for structural analysis of crystal surfaces during epitaxial growth. In RHEED, a beam of electrons with energies of around 30 keV is produced by an electron gun and is made to impinge on the surface at very small angles (typically less than 5°). The electrons then interact with the surface atoms and are scattered by these, producing a diffraction pattern upon reaching a phosphor screen located directly opposite the electron gun. While RHEED is a very useful technique for monitoring growth rates and surface structures, it can only give averaged-out information of the surface. With LEED, on the other hand, it is possible to obtain diffraction information of microscale regions of the surface as contrast apertures of different sizes can be used. Moreover, one can previously image the surface using LEEM before selecting what region to analyze

using LEED.

When it comes to contrast, there are basically two kinds. Diffraction contrast and phase contrast (here the word 'phase' refers to the displacement of two plane waves that have the same frecuency). Diffraction contrast occurs if different regions of the surface have different reflectivities. For example, if there are two phases present on the surface (this may happen, due to the long range elastic interaction between phase domains [6]), these may have different reflectivities, and therefore a bright-field LEEM image would show contrast between regions corresponding to different phases. Fig. 2.6 is a bright-field LEEM image of a GaAs(001) surface under vacuum. As can be observed there is marked contrast defining regions of dark and light intensities. These regions correspond to the (6×6) and $c(8\times2)$ reconstructions respectively. The (6×6) reconstruction decorates the steps, and, as it has a lesser reflectivity for the incident electron energy in use, it appears darker than the $c(8\times2)$ regions farther from the steps.

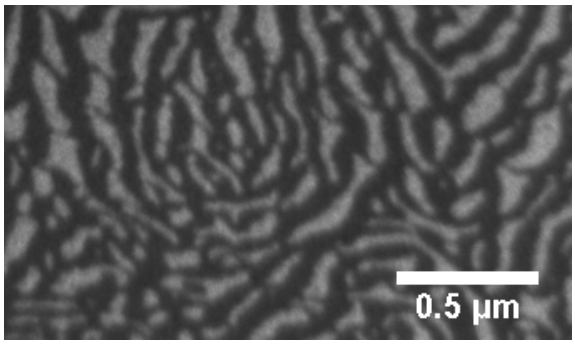

Figure 2.6: Bright-field LEEM image of a GaAs(001) surface under vacuum. The electron energy is 8.6 eV. Two surface phases, the (6×6) and the $c(8\times2)$, are present simultaneously on the surface can be contrasted due to the different reflectivities of either phase to the incident electrons.

Phase contrast occurs as a consequence of the interference of electrons reflected from the surface with phase shifts relative to one another. For example, step contrast is a type of phase contrast generated by the interference of electrons reflected from either side of an atomic step. These electrons will have a phase shift relative to one another given the difference in path length taken by either of them. For the electron energies used in LEEM, the wavelength of the electrons will be of the order of the step height. Therefore by carefully tuning the electron energy, the phase difference and hence the interference of the electrons can be tuned so as to provide sharp step

contrast. Fig. 2.7 shows a bright field image of a GaAs(001) surface under vacuum. As can be observed, dark lines corresponding to atomic steps can be clearly resolved.

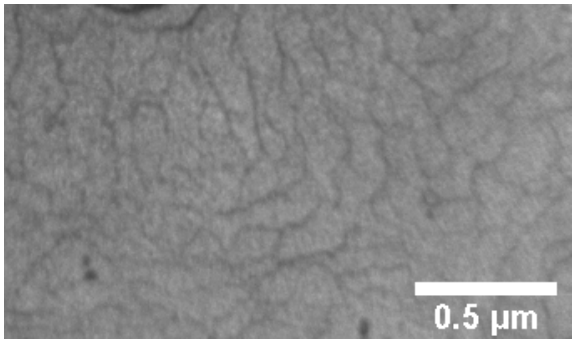

Figure 2.7: Bright-field LEEM image of a GaAs(001) surface under vacuum. The electron energy is 8.6 eV. As can be observed, atomic steps (the dark lines) are clearly resolved.

Because of the mechanism of step contrast explained above, LEEM is said to have atomic resolution in the direction perpendicular to the surface. Spatial resolution in the plane of the surface is not as high, but it can come down to around 5 nm. Together with the fact that LEEM can be operated at chamber pressures of up to $\sim 10^{-6}$ Torr and at sample temperatures up to ~ 2000°C, LEEM is an optimal tool to investigate semiconductor and metallic surfaces under growth conditions.

2.4.2 The LEEM-MBE System

LEEM has been used to study many metal surfaces such as molybdenum [80] or lead [81] as well as semiconductor surfaces (mosty silicon [82]). Our system is an Elmitec LEEM microscope with MBE effusion cells incorporated onto it. It was designed by Prof David Jesson at Monash University and is the only one in the world that is capable of imaging III-As surfaces under realistic growth conditions.

Fig. 2.8 shows a photograph of our LEEM-MBE system. As can be seen at the top-right, the electron beam is generated by an electron gun. The beam goes through the illumination column, and it is redirected $\sim 60°$ toward the main chamber where the sample resides. Gallium and arsenic fluxes can be supplied to the sample by opening the As cracker source (middle-left) or the Ga source (middle-right). The electron beam reflected from the sample is re-directed by the beam separator toward the imaging column, and the image formed is recorded by the CCD camera located

at the end of the imaging column.

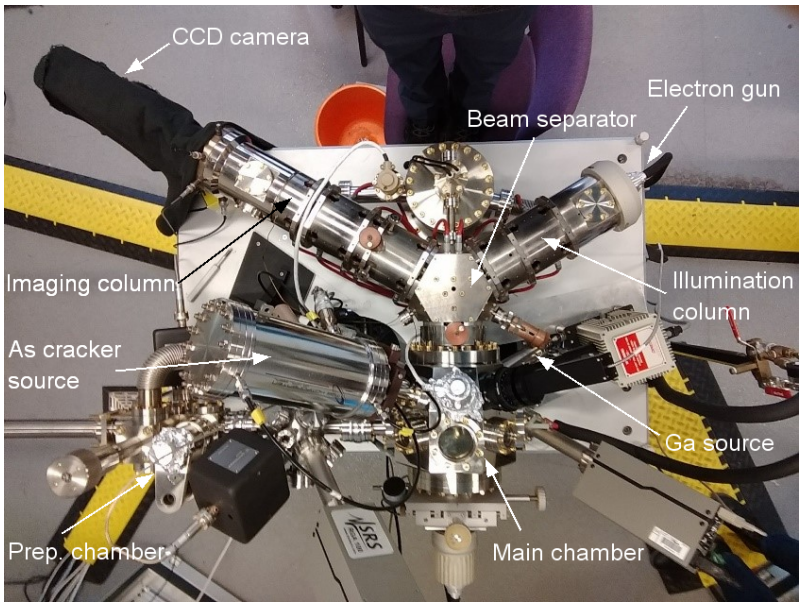

Figure 2.8: Top view of our LEEM-MBE system at Cardiff University.

Important results have been achieved in this system concerning the behaviour of Ga droplets on heated GaAs(001) surfaces [37, 83], growth mechanisms have been observed [39] and novel surface phases have been identified [4]. As we will see in Chapters 3 and 4, unprecedented results concerning novel forms of phase coexistence have been observed using this system, and controversial issues concerning surface phase stability have been addressed by experiments in our LEEM-MBE instrument.

2.4.3 Sample Preparation

One important step in investigating the GaAs(001) surface using LEEM is the preparation of the surface. In conventional MBE systems, a GaAs(001) surface is usually prepared for subsequent growth experiments by a procedure that follows two steps. The first is to remove the surface oxide by annealing the sample at a moderately high temperature (around 580°C) for around 2 hours. This, however, leaves a rough surface with a high density of pits that is unsuitable for further experiments. The subsequent step is, therefore, the growth of a GaAs buffer layer, in order to planarise the surface and prepare it for further growth experiments.

In our LEEM-MBE system we cannot prepare GaAs(001) surfaces following the standard steps because growing thick layers of GaAs would contaminate the objec-

tive lens too quickly. Therefore we take a slightly different approach to prepare a GaAs(001) surface for imaging. After degassing our samples during 24 hours in the preparation chamber and annealing it at 580°C during 2 hours in the main chamber, we heat the sample to around 650°C to produce Ga droplets on the surface and let them run across it [37]. The running droplets leave smooth GaAs(001) trails behind them as a result of drilling of the droplets into the GaAs solid. Fig. 2.9 shows one such smooth trail of GaAs(001) that is left behind as the Ga droplet moves to the left.

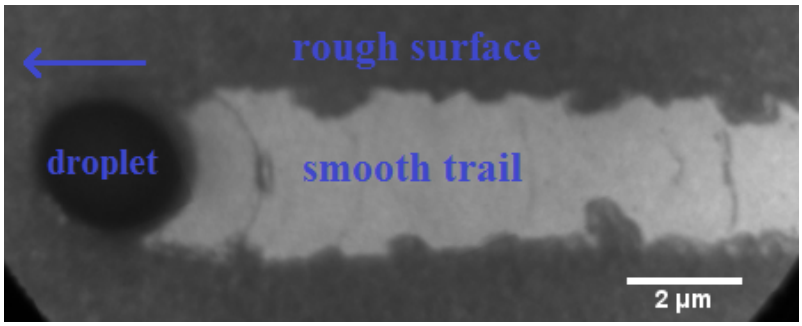

Figure 2.9: Bright-field LEEM image of a Ga droplet on a GaAs(001) surface. A rough surface surrounds the droplet except for a smooth trail that is left behind as the droplet moves. The arrow indicates the direction in which the droplet is moving.

Having used this method of sample preparation consistently through the years, let us consider each of its steps in physical terms. Firstly, we will address how Ga droplets are formed when heating the sample. Let us consider now a heated GaAs(001) surface. At steady state, Ga and As evaporate from the surface at equal rates. This means that

$$\frac{C_{\mathrm{Ga}}}{\tau_{\mathrm{Ga}}} = \frac{C_{\mathrm{As}}}{\tau_{\mathrm{As}}}, \tag{2.50}$$

where τ_{Ga} and τ_{As} are the lifetimes of Ga and As adatoms before desorption. Rearranging and introducing the temperature-dependence of the lifetimes gives

$$\frac{C_{\mathrm{Ga}}}{C_{\mathrm{As}}} = \frac{\tau_{\mathrm{Ga}}}{\tau_{\mathrm{As}}} = \frac{f_{\mathrm{As}}}{f_{\mathrm{Ga}}} \exp\left(\frac{E_{Ga,d} - E_{As,d}}{kT}\right), \tag{2.51}$$

where f_{Ga} and f_{As} are the attempt frequencies for desorption of Ga and As respectively, and $E_{Ga,d}$ and $E_{As,d}$ are the activation energies. As arsenic has a higher barrier for desorption than Ga does, i.e. $E_{As,d} > E_{Ga,d}$, with increasing T As desorbs

more readily than Ga. Therefore $\tau_{\mathrm{Ga}}/\tau_{\mathrm{As}}$ increases and hence $C_{\mathrm{Ga}}/C_{\mathrm{As}}$ increases, as per Eq. (2.51). This means that the GaAs(001) surface becomes more Ga-rich with increasing T. Fig. 2.10 shows a plot from Ref. [4] of Ga adatom chemical potential as a function of T aside the chemical potential μ^l_{Ga} $(= g^l_{\mathrm{Ga}})$ of liquid Ga. At low T, the Ga adatom chemical potential lies below that of liquid Ga, i.e., $\mu_{\mathrm{Ga}} < \mu^l_{\mathrm{Ga}}$. However, with the increasingly Ga-rich surface, μ_{Ga} approaches μ^l_{Ga} until $\mu_{\mathrm{Ga}} = \mu^l_{\mathrm{Ga}}$ at a certain temperature T_c close to 650°C (see Fig. 2.10). For temperatures higher than T_c droplets may form on the surface, since $\mu^l_{\mathrm{Ga}} < \mu_{\mathrm{Ga}}$, i.e., a Ga adatom as part of liquid Ga is energetically more favorable than Ga as an adatom. This explains how droplets may form on the GaAs(001) simply by annealing above T_c under vacuum. This critical temperature is the maximum temperature for congruent evaporation of Ga and As from the surface. It thus receives the name of congruent evaporation temperature of GaAs(001), and lies around ~ 650°C.

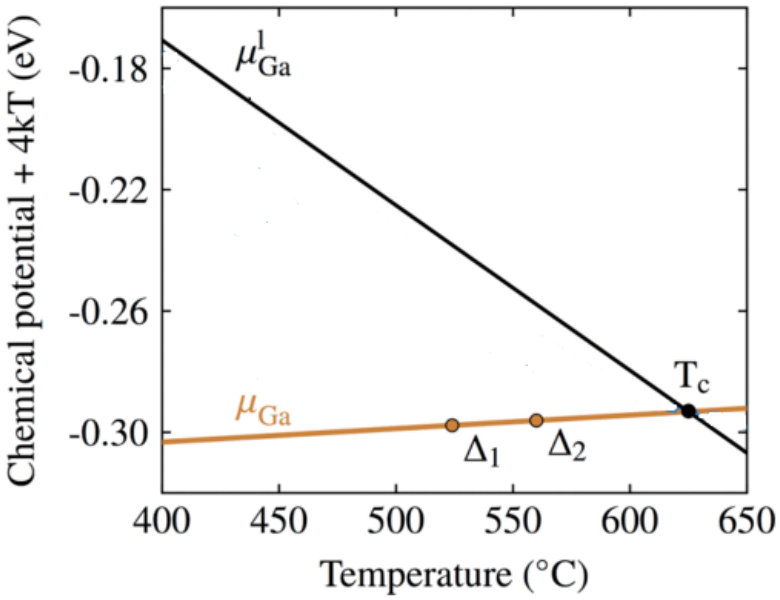

Figure 2.10: Ga chemical potential graph versus temperature T. The brown/orange line corresponds to the Ga adatom chemical potential μ_{Ga}. The dark line corresponds to the chemical potential of liquid Ga, μ^l_{Ga}. As can be seen μ_{Ga} surpasses μ^l_{Ga} at a certain temperature T_c. Note that $\mu_{\mathrm{Ga}} + 4kT$ is plotted instead of simply μ_{Ga}. This is simply because μ_{Ga} in practice contains a contibution of vibrational entropy of approximately $4k$ (neglected in Section 2.1.1), which makes μ_{Ga} decrease with T although C_{Ga} increases. $\mu_{\mathrm{Ga}} + 4kT$ is thus used in order for it to be a better measure of the Ga adatom concentration C_{Ga}. This figure has been adapted from Ref. [4].

Having understood how droplets form upon annealing GaAs(001) above congruent evaporation temperature T_c, we still ought to understand why they run across

the surface and leave smooth GaAs(001) trails behind. This is explained in detail in Ref. [37] but here we will provide a brief explanation.

Initially, the droplet sits on the surface surrounded by a GaAs surface with Ga adatom chemical potential μ_{Ga} defined by the Ga and As evaporation kinetics. This is a symmetric situation in which the droplet will not experience a net force at the contact line. However, if the droplet is spontaneously displaced to one side by a thermal fluctuation, the freshly exposed surface will be at chemical potential μ^l_{Ga} (the chemical potential of liquidus Ga), given the droplet acts as a reservoir for Ga. In this situation, the symmetry is broken as the surface Ga chemical potential will be μ_{Ga} on one side, and μ^l_{Ga} on the other. As explained in Section 2.3, the surface free energy depends upon the ambient chemical potential. Therefore it will be different on either side of the droplet. On the side toward which the droplet has moved we denote the surface free energy will by γ, while on the side of the freshly exposed surface we denote it by γ^l. This difference in surface free energy on either side of the droplet gives a net force on the contact line that is given by

$$F = \left(\gamma - \gamma^l\right) d, \tag{2.52}$$

where d is the total length of the droplet contact line. If the surface free energy of the freshly exposed surface is lower than the that of the rest of the surface, i.e., if $\gamma > \gamma^l$, then the force F will be in the direction of the displacement, and the droplet will run across the surface. In Ref. [37] it is shown that this is indeed the case. Furthermore it is shown that $\left(\gamma - \gamma^l\right) = \alpha \left(T - T_c\right)^2$, where α is a proportionality constant. Therefore, the force F on the droplet depends on temperature as

$$F = \alpha \left(T - T_c\right)^2 d. \tag{2.53}$$

Note that $F = 0$ at $T = T_c$, as the surface will be at μ^l, and thus the general surface and freshly exposed surface will have the same structure and surface free energy, i.e., $\gamma = \gamma^l$.

As we will see in Chapter 5, Ga droplets exchange material with the GaAs

surface beneath them. The droplets then leave behind smooth trails of GaAs(001) as they run along. Once enough of the surface has been smoothed, the droplets are made to disappear by lowering T appreciably below T_c. Under these conditions the surface chemical potential μ_{Ga} is below the Ga liquidus chemical potential μ^l_{Ga} (as can be appreciated in Fig. 2.10) and hence the droplets shed their Ga to the adatom population, which eventually desorbs into the vacuum. After a few hours (typically overnight), the microscale Ga droplets have disappeared completely, leaving behind a GaAs(001) surface with smooth trails on which we perform our LEEM observations.

2.4.4 Surface Phase Discrimination using Selective Energy Dark Field Techniques

As explained in Section 2.4.1, when observing a crystalline sample in a LEEM instrument, electrons will be diffracted and backscattered at specific angles. Electrons emitted at the same angle will be focused to the same point in the back focal plane, where a diffraction pattern is produced. This technique for diffraction is named low energy electron diffraction (LEED), and it is widely used in LEEM instruments to examine the structure of the surface under study given the surface periodicity is manifested in the diffraction pattern.

The specular beam tends to be the most intense of the backscattered beams. Therefore, the (00) spot is the one that is filtered in conventional LEEM imaging, and is called bright-field imaging. However, a diffracted beam other than the (00) spot can be filtered. This sort of imaging is named dark-field imaging. Though less intense than bright-field imaging, dark-field imaging is particularly useful in identifying regions of the surface corresponding to a certain phase when more than one phase is present (in Chapters 3 and 4 we will see that it is possible to have more than one surface phase simultaneously).

Fig. 2.11(c) and (d) show dark-field LEEM images of a $c(8 \times 2)$-reconstructed GaAs(001) surface containing a region of (6×6). In the case of Fig. 2.11(c), it is a spot corresponding to the (6×6) pattern that is filtered for imaging (as indicated in (a)). For this reason, the region of the surface corresponding to the (6×6) re-

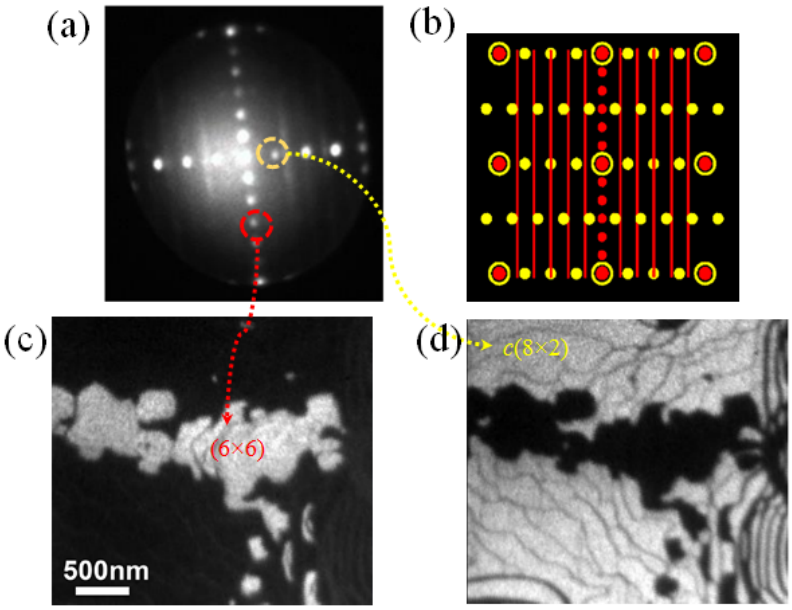

Figure 2.11: (a) Representative LEED pattern from a GaAs(001) surface showing a superposition of (6×6) and $c(8 \times 2)$ patterns. (b) Schematic diagram showing the superposition of (6×6) (in red) and $c(8 \times 2)$ (in yellow) LEED patterns. (c) Dark field image of a GaAs(001) surface obtained from filtering the (0,3/6) spot of the diffraction pattern. (d) Dark field image of a GaAs(001) surface obtained from filtering the (1/4,0) spot of the LEED pattern. (a) was acquired by Dr. Daniel Gomez Sanchez. (b), (c), and (d) were reprinted from Ref. [5]

construction appears bright, while the rest of the surface is dark. In Fig. 2.11(d), in contrast, it is a spot of the $c(8 \times 2)$ diffraction pattern that is filtered (the one indicated in (a)). Therefore, the region of the surface covered in $c(8 \times 2)$ appears bright, while the rest appears dark. Note that Figs. 2.11(c) and (d) are complementary images of one another, since the surface contains only the $c(8 \times 2)$ and (6×6) reconstructions. This shows the convenience of dark-field imaging in identifying and spatially resolving regions of a surface exhibiting different reconstructions.

As mentioned earlier, diffraction spots tend to be significantly less intense that the specular (00) spot. In a study published in Ref. [5], our group has further developed a technique that combines energy selection and dark-field imaging. It was found that the energy of the electrons impinging the sample (i.e., the sample voltage) can then be fine-tuned in order to maximize the intensity of the LEED spots. Imaging at this maximizing electron energy provides strong contrast between regions of differing surface structure, giving rise to images as those in Fig. 2.11(c) and (d).

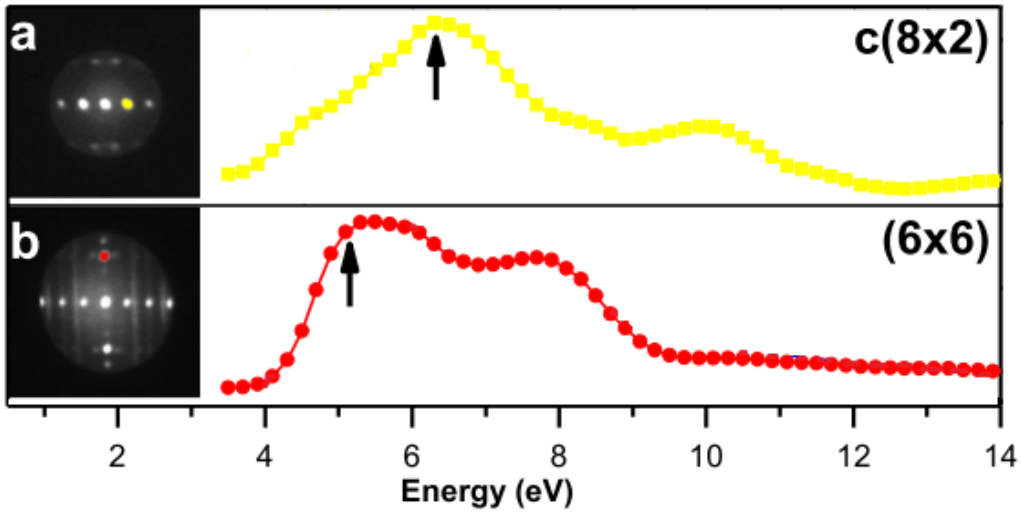

Figure 2.12: I(V) curves performed on the diffraction spots highlighted on the LEED patterns on the left.(a)(1/4,0) spot of $c(8 \times 2)$. (b) (0,3/6) spot of the (6×6). The arrows indicate the optimal energies of the I(V) curves. These are 6.2 eV for the $c(8 \times 2)$ spot, and 5.0 eV for the (6×6) spot. Reprinted from Fig. [5].

These maximizing electron energies are found by scanning through the full range of sample voltages V and registering the diffraction spot intensity I, thereby producing what is know as an $I(V)$ curve. The I(V) curve of the (0,3/6) spot of the (6×6) and that of the (1/4,0) spot of the $c(8 \times 2)$ are shown in Fig. 2.12. As can be observed, the $c(8 \times 2)$ spot reaches the maximum energy at 6.2 eV, while the (6×6) does so at 5.0 eV. It is therefore at these electron energies that dark-field imaging is optimised. In fact, the images in Figs. 2.11(c) and (d) are taken at these optimal energies. We name this novel dark-field technique selective energy dark field (SEDF). As we will see in Chapters 3 and 4, SEDF proves to be a powerful technique to investigate surfaces showing several reconstructions simultaneously.

Chapter 3

Surface Phase Metastability during Langmuir Evaporation

In this chapter we present a piece of work that was undertaken recently by our group regarding a novel form of surface phase coexistence on GaAs(001). This work is published in K. Hannikainen, D. Gomez, J. Pereiro, Y. R. Niu, and D. E. Jesson, *Phys. Rev. Lett.* **123**, 186102 (2019). In summary, we directly imaged the spontaneous formation of metastable surface phase domains on GaAs(001) during Langmuir evaporation. Eventually, these metastable phases transform to the thermodynamically stable parent phase, producing a dynamic phase coexistence with a temperature dependent, time-averaged coverage. Monte Carlo simulations were used to identify the key kinetic processes and investigate the interplay between phase metastability and evolving surface morphology. This is used to explain the measured temperature dependence of the time-averaged coverage.

3.1 Introduction

As was argued in the previous Chapter, given certain ambient conditions in the growth chamber, the stable GaAs(001) surface phase is the one that minimizes the system's free energy for those conditions. Therefore it is this and only this equilibrium phase that is expected to be observed experimentally, provided it is kinetically accessible from the surface's initial state and sufficient time is let for the

system to relax.

Surprisingly, it is possible to observe thermodynamically stable phase coexistence on a crystal surface, where two phases are present side-by-side on the surface in a stable fashion. In the early 2000s, this was shown to occur during the Si(111)-(7×7) to (1×1) surface phase transition with temperature [6] (note that on Si there is no variation of the ambient stoichiometry as it is a monocomponent crystal, and so other factors such as thermal vibrations of the surface lattice ought to be what determines stability). Instead of observing a sharp phase transition from (7×7) to (1×1) upon attaining the thermodynamic phase transition temperature T_c, something quite different was observed. On the stepped and slightly misoriented (111) surface, consecutive stripes of the (7×7) and (1×1) phases were seen to coexist, as shown in the LEEM image of Fig. 3.1. The (7×7) stripes are bounded by a step on one side (the upper side of the step), while their other boundary lies in the middle of the terrace. These boundaries are labeled S and T respectively on Fig. 3.1. In Ref. [6] it is argued that this phase coexistence is due to the long-range elastic and electrostatic interactions between the phase domains. These interactions are such that having the two phases coexisting in the above manner in a certain proportion minimizes the free energy. Having one phase or the other would present a higher energy configuration. At lower temperatures the proportion of (7×7) is higher, but, upon increasing the temperature and going into the regime where the (1×1) is the thermodynamically stable phase, the (1×1) stripes progressively take over the terraces between successive steps, as is shown in Fig. 3.2. This temperature dependence of the phase coverage can be visualized in Fig. 3.2.

In the GaAs(001) system we see an analogous phenomenon occur. At $T = 580°\mathrm{C}$ (a typical temperature for MBE growth), the surface exhibits the Ga-rich $c(8 \times 2)$ reconstruction in the absence of fluxes [4]. As the sample is cooled, the adatom population becomes As-richer (see Eq. (2.51)), and one eventually observes a (6×6) phase (the (6×6) line does not appear on the phase diagram of Fig. 2.4; this will be addressed in Chapter 4). However, the phase transition does not occur abruptly as one would expect. As in the case of Si, the (6×6) coverage increases gradually

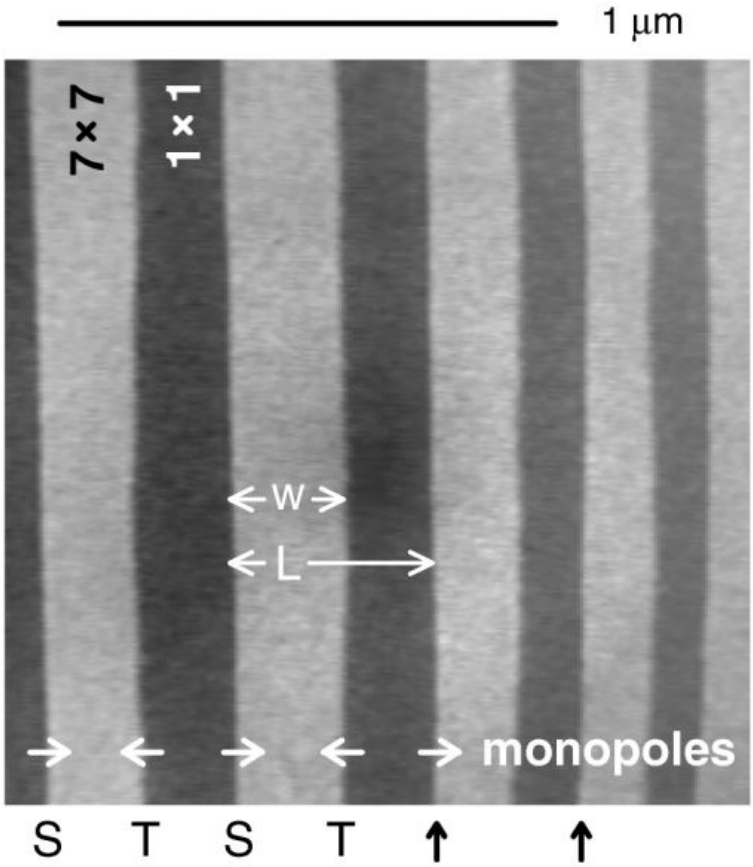

Figure 3.1: Bright-field LEEM image of an Si(111) surface. Dark and light stripes are seen to coexist, corresponding to the (1×1) and (7×7) reconstructions respectively. The phase boundaries occur at steps (S) and in the middle of terraces (T). The steps ascend toward the right. The white arrows show the orientation of the elastic force at the phase boundaries (force 'monopoles') due to differences of surface stress between either reconstruction. Reprinted from Ref. [6].

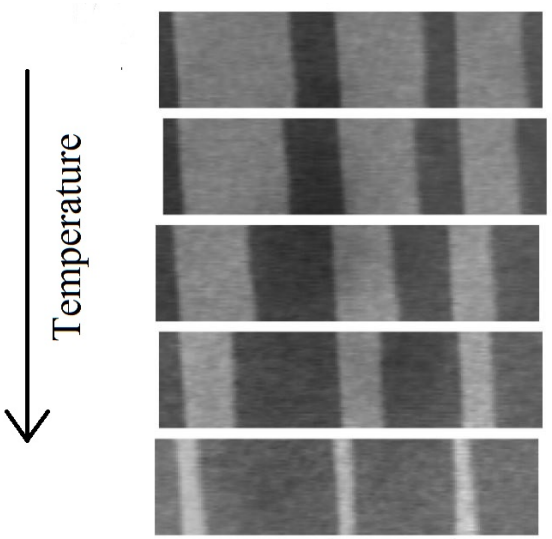

Figure 3.2: Bright-field LEEM images of a Si(111) terrace at different temperatures. At the lower temperatures the (7×7) stripes appear wide. Upon increasing the temperature, the phase boundaries in the middle of the terraces move so as to provide thinner (7×7) stripes and wider (1×1) stripes. Approximately a range of 15°C is spanned. The horizontal width of the images is 1 μm. Reprinted from Ref. [6].

as the sample is cooled. This can be clearly appreciated in the bright-field LEEM images of Fig. 3.3, where the bright surface corresponds to $c(8 \times 2)$ and the dark surface corresponds to (6×6). In Fig. 3.3(a) (at $T \sim 600$°C) the surface displays a $c(8 \times 2)$ reconstruction only. As the temperture is decreased ((b) and (c)), it can be observed that (6×6) appears pinned to the steps, and the width of the (6×6) stripes gets larger with decreasing temperature. At sufficiently low temperature the (6×6) takes over the whole surface (Fig. 3.3(d)). Therefore, thermodynamic coexistence of two phases occurs also on GaAs(001) as a consequence of long range interactions between the phase domains, analogous to the case of Si in Ref. [6].

In this piece of work, however, we find a completely novel form of phase coexistence between the (6×6) and $c(8 \times 2)$ phases when heating GaAs(001) above $T \approx 580$°C. As we will see, this novel form of phase coexistence has nothing to do with the thermodynamic coexistence known to date, but rather it is intrinsically linked to the kinetics of Langmuir evaporation (free evaporation into the vacuum), which becomes important at elevated temperatures.

Langmuir evaporation has been extensively investigated throughout the years [38,52,84–87]. It is the non-equilibrium evaporation occuring when heating a surface

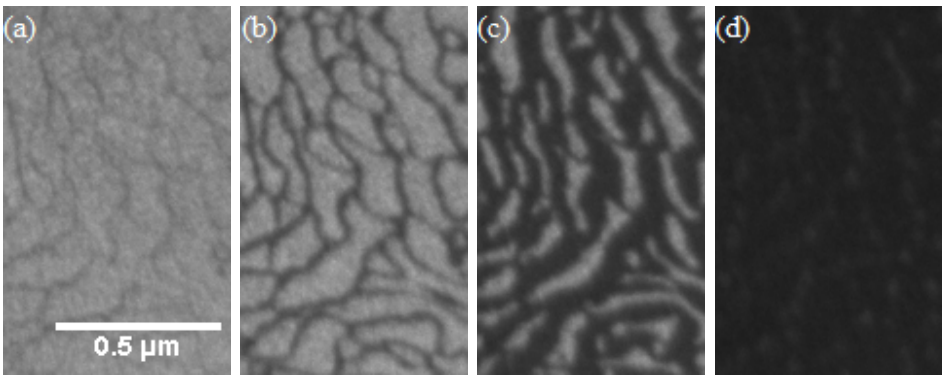

Figure 3.3: Bright-field LEEM images of the GaAs(001) surface under vacuum at different temperatures ranging from (a) $T \sim 600°C$ to (d) $T \sim 500°C$, and showing the $c(8 \times 2)$ to (6×6) surface phase transition. At the highest temperature (panel (a)) the surface exhibits a $c(8 \times 2)$ reconstruction. As it is cooled (panels (b) and (c)) the $c(8 \times 2)$ begins coexisting along with the (6×6) phase, with an increasing coverage of the latter phase. At the lowest temperature (panel (d)), the (6×6) covers the surface completely. This is why the entire surface appears dark. These images were acquired by Dr. Daniel Gomez Sanchez using our LEEM-MBE system at Cardiff University.

under vacuum. Not only is it of fundamental scientific importance, but it is directly relevant to the processing and growth of thin films and nanostructures across a wide range of technologies [38, 52, 67, 84–91]. In this piece of work we investigate the GaAs(001) surface using LEEM, and we observe a surprising new feature occuring during Langmuir evaporation. We see metastable surface phases form spontaneously when unstable subsurface layers are exposed by evaporation. These metastable phases eventually convert to the thermodynamically stable parent phase, thereby producing a temperature-dependent, time-averaged metastable phase coverage. This dynamic phase coexistence has important implications in the application of phase diagrams, since these neglect evaporation and in which a single phase is usually assumed to be present. It is likely that this phenomenon of phase metastability, which is linked to evaporation is relevant for the optimization of thin film growth conditions across a wide range of materials.

3.2 Experimental details

Our experiments were carried under ultrahigh vacuum, in the LEEM-MBE system described in Chapter 2, which is especially modified for III-V MBE [36]. The

temperature was calibrated by observing Ga droplet generation [52] and various surface phase transformations [1]. As explained in Chapter 2, we prepare an undoped GaAs(001) sample by degassing at 300 °C for 24 h and subsequently annealing at 580 °C for 2 h to remove the surface oxide. In order to produce smooth regions of GaAs(001), the sample was heated above the congruent evaporation temperature to 650 °C in order to generate Ga droplets of radius $\sim 2\,\mu$m. As delineated in Chapter 2, these are let to run across the surface [37, 92], leaving a smooth GaAs(001) trail behind which we can use for our imaging experiments [93]. Finally, the Ga droplets were completely removed by annealing below the congruent evaporation temperature at 570 °C.

3.3 Main Results

The sample was then heated above 580 °C for our imaging experiments. At these temperatures the surface is expected to exhibit the well-studied $c(8 \times 2)$ reconstruction, which is widely accepted to be stable under these conditions [1,4,71,73]. Figure 3.4 contains snapshots taken from a LEEM movie [1] of GaAs(001) at 598 °C. These were acquired under bright-field imaging conditions at an incident electron energy of 8.6 eV. At the initial instant, panel (a) displays uniform, bright intensity corresponding to the expected $c(8 \times 2)$ reconstruction. Two atomic steps, which are receding due to evaporation, are indicated by the arrows. These steps are of bilayer height [94], and they separate $c(8 \times 2)$ reconstructed terraces. Surprisingly, after 384 s, a dark patch appears in the center of the terrace (panel (b)) and grows (panels (c) and (d)). As was explained in Chapter 2, different surface phases generally have different reflectivities with respect to the incoming electrons. Therefore the dark contrast indicates the probable presence of a phase different to the $c(8 \times 2)$. The dark patch continues to grow until $t = 1416$ s when a small region of $c(8 \times 2)$ phase nucleates within the dark patch (panel (e)). The $c(8 \times 2)$ region then grows at the expense of the dark phase until it is completely consumed, and only $c(8 \times 2)$ remains

[1] See the supplemental material of Ref. [40] at https://journals.aps.org/prl/supplemental/10.1103/PhysRevLett.123.186102 for a LEEM movie of GaAs(001) Langmuir evaporation.

bounded by a bilayer height step loop.

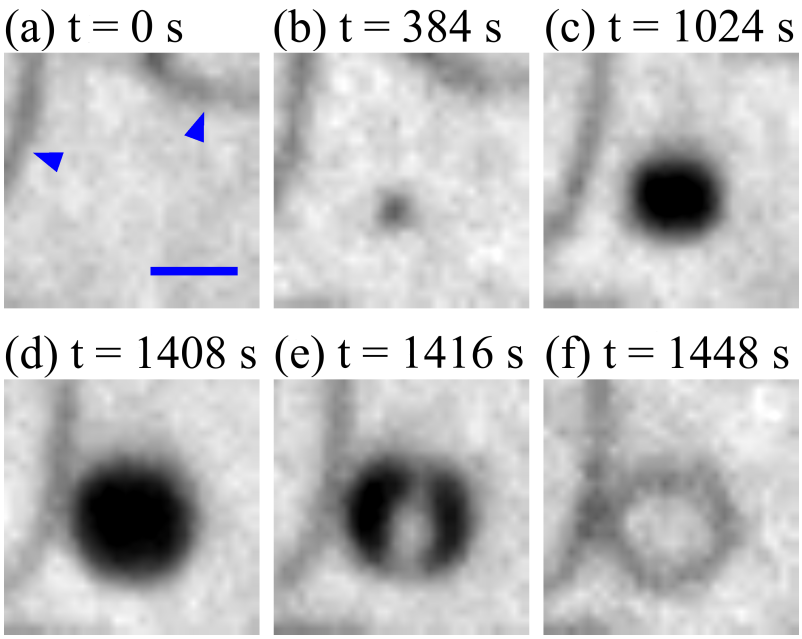

Figure 3.4: Snapshots taken from a LEEM movie revealing the fundamental mechanism of surface phase metastability. The $c(8\times2)$ phase appears bright, whilst (6×6) and steps (indicated with arrows in (a)) appear dark. The scale bar in (a) is $0.1\,\mu$m and the sample temperature is 598 °C. These images have been smoothed utilizing standard interpolation methods.

Suspecting this dark phase could correspond to (6×6) we performed a different experiment in order to find an optimal location for the contrast aperture, i.e., one that filters only electrons diffracted by the (6×6) structure, only to then perform (6×6) dark-field imaging on our original experiment. In this side experiment, a GaAs(001) sample was cooled to around 540°C, where we know (6×6) exists aside the $c(8 \times 2)$ phase in a thermodynamically stable manner, and a LEED pattern of the surface was acquired. This LEED pattern is shown in Fig. 3.5(c), and, as can be observed, it presents an expected superposition of $c(8 \times 2)$ and (6×6) patterns. A schematic diagram showing superimposed (6×6) and $c(8 \times 2)$ LEED diagrams is shown in Fig. 3.5(d), where the blue spots correspond to the $c(8 \times 2)$ phase and the pink spots correspond to the (6×6) phase. The position of the $(0, 1/6)$ spot of the (6×6) pattern was conveniently chosen, given it is far from overlapping a spot corresponding to the $c(8 \times 2)$. This spot is encircled in blue in 3.5(c).

Reproducing our original experiment to observe again metastable patches, we increased the sample temperature to 580°C and performed SEDF-imaging (see Chap-

ter 2) on our sample, placing the contrast aperture at the convenient position (located during the previous experiment described above) and tuning the electron energy to 3.5 eV. The result was that the domains that appeared dark during bright-field imaging appeared bright when switching to dark field, thereby confirming that they correspond to the (6×6) reconstruction. On the other hand, the rest of the surface, corresponding to the $c(8 \times 2)$ phase appeared dark as was expected. This can be seen in the bright-field and dark-field images of the GaAs(001) surface shown in Fig. 3.5(a) and (b) respectively.

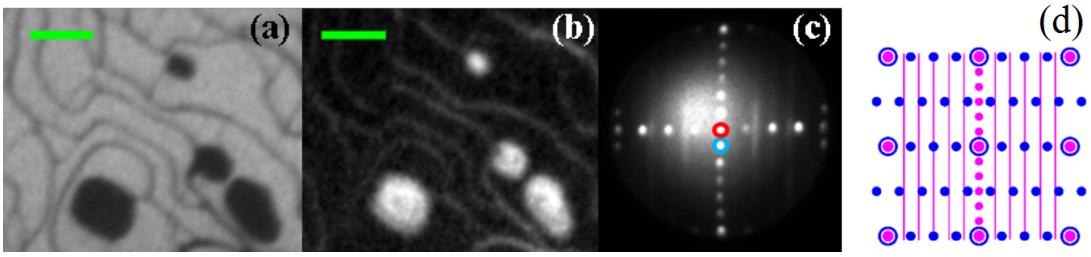

Figure 3.5: (a) BF image obtained at 8.6 eV from the $(0, 0)$ spot encircled in red in (c). (b) DF image obtained at 3.5 eV from the $(0, 1/6)$ spot encircled in blue in (c). (c) Representative LEED pattern of GaAs(001) revealing a superposition of $c(8 \times 2)$ and (6×6) patterns and indicating the diffraction spots used to obtain the images in (a) and (b). (d) Schematic pattern showing a superposition of $c(8 \times 2)$ (blue) and (6×6) (pink) LEED patterns. The scale bars in (a) and (b) are 0.3 μm.

The nucleation and growth of (6×6) patches, followed by subsequent annihilation by $c(8 \times 2)$ occurs as discrete events across the entire surface when heating the GaAs(001) surface above $T \approx 580°$C. This produces a dynamic phase coexistence between (6×6) and $c(8 \times 2)$ domains with a time-averaged coverage of (6×6). Note again that this dynamic phase coexistence is entirely dissimilar to the thermodynamic phase coexistence explained previously (that of Fig. 3.3), and is intrinsically linked to the processes occuring during Langmuir evaporation.

To explain the appearance of the (6×6) patches in Fig. 3.4, we must consider the mechanisms of Langmuir evaporation. The nucleation and growth of surface macrovacancies (Lochkeim formation) is known to play an important role in the evaporation of surfaces [95–97]. Here, surface vacancies typically nucleate into stable monolayer height clusters in a terrace (on generic crystal surfaces), and the resulting step loop expands as atoms desorb from the surface, causing the macrovacancy to grow. This mechanism is consistent with our observations in Fig.3.4, but with one

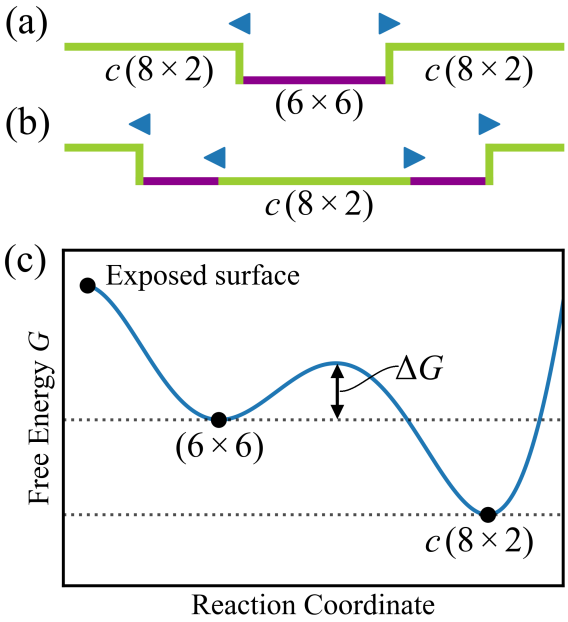

Figure 3.6: Cross-sectional schematic of Lochkeim formation and surface phase metastability. (a) A Lockheim forms in the $c(8 \times 2)$ phase (green line) and bilayer height steps propagate as atoms evaporate into the vacuum. The freshly exposed surface is the (6×6) phase (purple line). (b) $c(8\times2)$ nucleates within the (6×6) phase and the phase boundaries propagate until only $c(8 \times 2)$ is present. (c) Schematic representation of the change in surface free energy (per unit area) of the exposed surface. The exposed surface is unstable and transforms into the metastable (6×6) phase. An activation energy barrier ΔG exists for the conversion of the metastable (6×6) to the thermodynamically stable $c(8 \times 2)$.

important exception. The subsurface layer being unveiled by the macrovacancy in panel (b) presents a (6×6) reconstruction rather than the stable $c(8 \times 2)$. This is illustrated schematically in Fig. 3.6(a). To explain this, we note that the freshly exposed surface during macrovacancy nucleation is in an unstable state and does not necessarily have to transform directly into the most thermodynamically stable state. Rather, it can transform into a metastable intermediate state as conjectured by Ostwald [98–101] (see Fig. 3.6(c)). It is likely that the route to (6×6) from the freshly exposed, unstable surface will be influenced by surface strain generated by the initial small step loop. However, the atomic-scale details of the initial nucleation process is below our instrumental resolution. Eventually, the metastable (6×6) phase converts to the stable $c(8 \times 2)$ phase via the nucleation of $c(8 \times 2)$ within the (6×6) phase (panels 3.4(e), 3.6(b)and 3.6(c)). The $c(8 \times 2)$ phase then rapidly grows, leaving behind a bilayer height step loop on pure $c(8 \times 2)$ (panel 3.4(f)).

To quantify this dynamic mechanism we have measured the time-averaged cov-

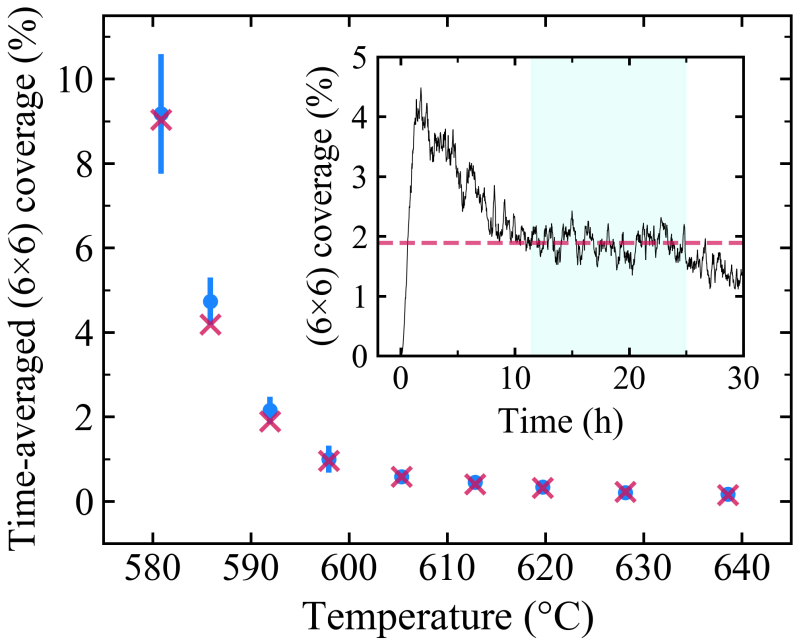

Figure 3.7: Time-averaged (6×6) coverage as a function of temperature. The circles are experimental values and the crosses were calculated from the MC simulations. The inset shows the time evolution of the (6×6) coverage produced by the Monte Carlo simulation at 592 °C. The dashed line shows the time-averaged coverage obtained from the shaded region (see text). Error bars are computed as standard deviations from the mean.

erage of (6×6) as a function of temperature T. This is displayed in Fig. 3.7. It shows the percentage (on average) of the surface that is covered by (6×6). The data was averaged over progressively shorter times and surface areas with increasing T due to the faster evaporation kinetics at higher temperatures. This ranged from 3 h/15 μm^2 at the lowest T (581 °C) to 30 min/3 μm^2 at the highest (639 °C). Below 580 °C, the kinetics of evaporation became too slow to obtain time-averaged data. It can be seen that the (6×6) coverage decreases from ~ 9 % at 580 °C to around 0.1 % at 640 °C. The existence of (6×6) in this temperature range is surprising as it is generally assumed that only one phase, $c(8 \times 2)$, is present. It is likely that the transient nature and relatively small time-averaged (6×6) coverage explains why this surface phase metastability has not been observed previously.

3.4 Monte Carlo modeling

We have developed a Monte Carlo (MC) simulation model to explain the temperature dependence of the coverage. It is governed by a set of simple rules derived from

our LEEM movies. Here we describe the fundamental concepts on which the model is based. For a detailed description of the methodology used see Appendix B.

We consider a 10 μm square portion of a GaAs(001) surface, held at temperature T and subject to periodic boundary conditions. Point-like Lochkeime nucleate on the surface at a uniform rate of J_w per unit area. The macrovacancy step loop associated with the Lochkeim is then expanded at a uniform velocity v, as GaAs evaporates, revealing a bilayer deep, circular (6×6) terrace. This resembles Fig. 3.4(a)-(d) and the cross-sectional schematic in Fig. 3.6(a). The nucleation of $c(8\times2)$ on this terrace (Fig. 3.4(e), 3.6(b)) is taken to occur at a rate ρ per unit area. Since our movies show that the transformation of (6×6) to $c(8\times2)$ is fast on the timescale of all other evaporation-related kinetic processes, including Lochkeim formation and (6×6) terrace growth, we allow an instantaneous conversion of (6×6) to $c(8 \times 2)$ across the entire (6×6) terrace.

These simple rules adequately describe the fundamental process of (6×6) phase metastability shown in Fig. 3.4. However, to obtain a full, quantitative agreement with the experimentally observed coverage, our LEEM movies indicate that we must also incorporate several secondary processes into the MC model:

(i) We observe that Lochkeime form more readily on (6×6) than on $c(8 \times 2)$ (see Fig. 3.8). We therefore introduce an additional rate J_b for the rate of Lochkeim formation per unit area of (6×6). In accordance with observation, J_b is taken as uniform across a (6×6) domain but only up to one Lochkeim is allowed to form per (6×6) terrace. In addition, we observe that when this mechanism results in an 'inverted wedding cake' of (6×6) terraces, it is always the outer (highest) terrace which first transforms to $c(8 \times 2)$ (propagation of the stable phase stops at the step). This may reflect some stabilization of the inner (6×6) domains by surface stress.

(ii) When a $c(8 \times 2)$ terrace attains a critical radius R_c, one or more Lochkeime form at the center of the terrace (see Fig. 3.9). We note that an analogous phenomenon has been observed during the epitaxial growth of Ag [63]. For simplicity, we assume only one Lochkeim nucleation event per critically-sized $c(8 \times 2)$

terrace. This mechanism serves to maintain inverted wedding cake structures when (6×6) domains transform to $c(8 \times 2)$ before undergoing Lochkeim nucleation.

(iii) (6×6) domains may coalesce such that a single nucleation event at rate ρ transforms the entire terrace to $c(8 \times 2)$ (see Fig. 3.10).

(iv) When a (6×6) domain coalesces with a $c(8 \times 2)$ terrace, it rapidly transforms to $c(8 \times 2)$ (see Fig. 3.11), as the latter propagates to cover the whole combined terrace. This conversion to $c(8 \times 2)$ is incorporated in the model as an instantaneous event.

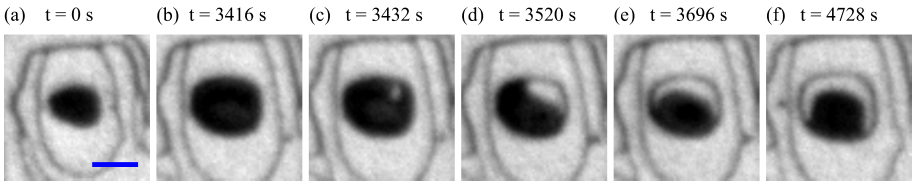

Figure 3.8: Sequence of LEEM images taken from a movie of a (6×6) terrace transforming to $c(8 \times 2)$. This initiates in panel (c) and continues through panels (d) and (e) until the transformation completes in (f), revealing a lower central (6×6) terrace. This indicates that multiple layers of (6×6) exist as inverted wedding cake structures and that Lochkeime form more readily on (6×6) than on $c(8 \times 2)$. Furthermore, we find it is always the outermost (uppermost) (6×6) terrace that transforms to $c(8 \times 2)$ first. The sample temperature is $T = 586\,^{\circ}\mathrm{C}$, and the scale bar is $0.2\,\mu\mathrm{m}$.

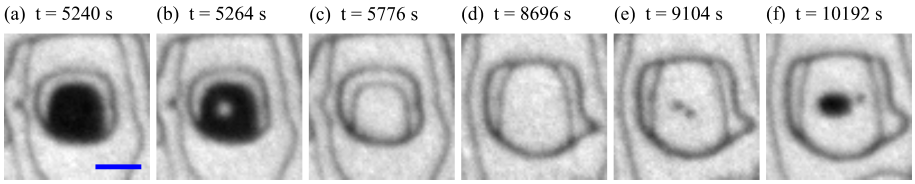

Figure 3.9: (Continued from Fig. 3.8) Sequence showing that one or more Lochkeime (in this case up to three) form almost simultaneously around the middle of a $c(8 \times 2)$ terrace upon it reaching a critical terrace radius R_c (panel (e)). The sample temperature is $T = 586\,^{\circ}\mathrm{C}$, and the scale bar is $0.2\,\mu\mathrm{m}$.

3.5 Discussion

As opposed to feeding arbitrary values for the rates, we measured J_w, J_b, ρ, and v directly from the LEEM movies at nine different temperatures in the $580 - 640\,^{\circ}\mathrm{C}$

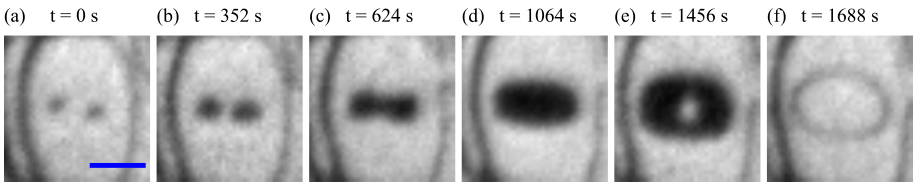

Figure 3.10: Sequence of LEEM images taken from a movie showing the coalescence of two (6×6) terraces, forming a larger (6×6) terrace. The combined (6×6) terrace transforms to $c(8\times2)$ as a single domain (panel (e), (f)). The sample temperature is $T = 592\,^{\circ}\mathrm{C}$, and the scale bar in (a) is $0.15\,\mu$m.

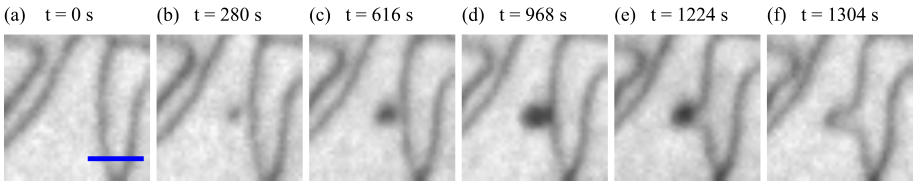

Figure 3.11: Sequence of LEEM images obtained from a movie showing that a (6×6) terrace transforms to $c(8\times2)$ on coalescing with a $c(8\times2)$ terrace. The sample temperature is $T = 586\,^{\circ}\mathrm{C}$, and the scale bar is $0.15\,\mu$m.

range (Fig. 3.12). To a good approximation, the step velocity is independent of the nature of the phases either side of the step. So only one velocity is used for all steps at a given T. Step bunching can affect the velocity, but this has a negligible effect on the simulations and so is neglected. J_b and ρ are determined from the measured distribution of (6×6) terrace size during respective Lochkeim and $c(8\times2)$ nucleation (See Appendix A). The measured value of $R_c = 0.17\,\mu$m is found to be approximately constant over the temperature range of interest.

We fit the T-dependence of J_w, J_b, ρ and v to the standard Arrhenius form, $x = x_0 \exp(-E_a/kT)$ where x_0 and E_a are the respective pre-factor and energy barrier with k equal to Boltzmann's constant (see Fig. 3.12). The determined pre-factors and energy barriers contained in the Fig. 3.12 caption are used in the MC simulations. However, these values should not be interpreted physically since it is well appreciated that non-Arrhenius temperature dependence can arise during the complex kinetic processes associated with evaporation [97]. Rather, the Arrhenius form used here should be viewed as a convenient fit to the measured data. Also, it ought to be mentioned that the linear fits shown in Fig. 3.12 are not exact least-squares fits to the experimental data. Rather they are only approximate fits within the experimental error bars.

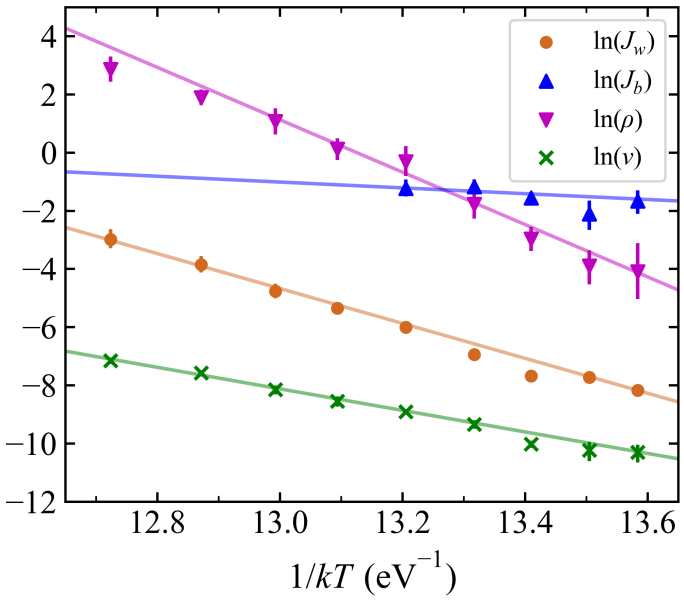

Figure 3.12: Measured rates of the key kinetic processes used in the MC simulations as a function of T. $\ln(J_w)$, $\ln(J_b)$, $\ln(\rho)$ and $\ln(v)$ are plotted against $1/kT$ with J_w, J_b and ρ in units of $\mu m^{-2}s^{-1}$ and v in μms^{-1}. The respective pre-factors of J_w, J_b, ρ and v obtained from the linear fits to the measured data are $7.0 \times 10^{31}\,\mu m^{-2}s^{-1}$, $1.6 \times 10^{5}\,\mu m^{-2}s^{-1}$, $2.0 \times 10^{51}\,\mu m^{-2}s^{-1}$ and $2.3 \times 10^{17}\,\mu ms^{-1}$ and the respective energy barriers are 6.0 eV, 1.0 eV, 9.0 eV and 3.7 eV (see text).

MC simulations were run for the nine temperatures corresponding to the LEEM measurements (see the MC simulation movie [2]). They begin with a pristine $c(8 \times 2)$ surface (with no steps or metastable (6×6) patches) exposed to the vacuum. As the simulations proceed, Lochkeime begin forming all across the surface and the (6×6) coverage initially increases rapidly. The absence of steps on the initial surface prevents many of these (6×6) patches to phase-transform by coalescence with $c(8 \times 2)$ terraces. As time passes the surface fills with steps and coalescence of terraces is enhanced. For this reason, the initial excess (6×6) coverage eventually decays and settles in to a steady state. The coverage and surface morphology associated with this steady state are used to compare with experiment. For the three lowest temperatures, rather than a strict steady state, we find a long-period decrease in (6×6). Fig. 3.13 shows the evolution of the coverage at low T ($T = 581°C$), intermediate T ($T = 592°C$), and high T ($T = 639°C$). As can be seen the low and intermediate T graphs show a long-period decrease in (6×6) coverage. This is the consequence of multilayer evaporation, and will be explained later. However, this

[2] See the supplemental material of Ref. [40] at https://journals.aps.org/prl/supplemental/10.1103/PhysRevLett.123.186102 for a Monte Carlo simulation movie of surface phase metastability during Langmuir evaporation

long decay is experimentally inaccessible and the shaded quasi-steady-state plateau region is used to determine the coverage for the three lowest temperature cases.

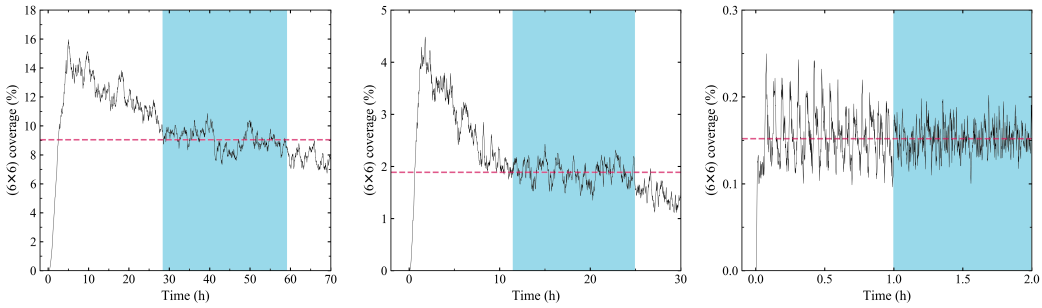

Figure 3.13: (6×6) coverage versus time graphs for the $T = 581°$C MC simulation (left), the $T = 592°$C simulation (middle), and the $T = 639°$C simulation (right). The shaded regions are the steady-state regions that are used to calculate time-averaged coverages. As can be seen this plateau is limited (for the low and intermediate T simulations), but it is indefinite for the high T simulation, as strict steady is obtaind in the latter case. The calculated time-averaged (6×6) coverages are 9.04% (left), 1.89% (middle), and 0.15% right.

The time-averaged (6×6) coverage evaluated by MC is compared with experiment in Fig. 3.7. Excellent agreement is found across the entire temperature range. Note that the fits in Fig. 3.12 were carefully tuned within the error bars to optimize agreement with experiment. To explain the decrease in (6×6) coverage with increasing T we compare snapshots of the experimental and simulated surface morphology at low, intermediate and high temperatures in Fig. 3.14. Again, the general reproduction of the salient experimental features by the simulations is very good. Fig. 3.15 shows the full 10μm $\times$ 10μm surfaces for our MC simulations at low T ($T = 581°$C), intermediate T ($T = 592°$C), and high T ($T = 639°$C). Both experiment and simulation indicate that there is a clear change in surface morphology intrinsically linked to the varying (6×6) coverage with T. By combining the MC simulation of surface morphology in Figs. 3.14 and 3.15 with the measured rates of the key kinetic processes in Fig. 3.12, we can now explain the link between evolving morphology and the T-dependent (6×6) coverage measurements in Fig. 3.7.

At low T, it can be seen from Fig. 3.12 that $J_b > \rho$. This means that Lochkeim nucleation is more likely to occur on metastable (6×6) domains before they transform to $c(8 \times 2)$. Furthermore, the relatively high J_b/v ratio in this regime produces densely packed concentric (6×6) terraces, and gives rise to a surface populated

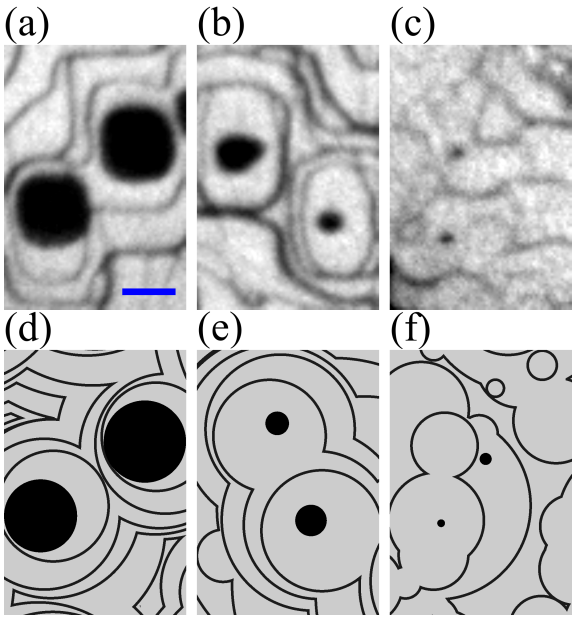

Figure 3.14: Snapshots of evolving surface morphology taken from LEEM movies at (a) 581 °C, (b) 598°C and (c) 639 °C and MC simulation movies at (d) 581 °C, (e) 598 °C and (f) 639 °C. Dark areas correspond to (6×6) terraces. The scale bar in (a) is 0.2 μm. The simulation panels were chosen out of several simulation images in order to optimise correspondence with the experimental panels.

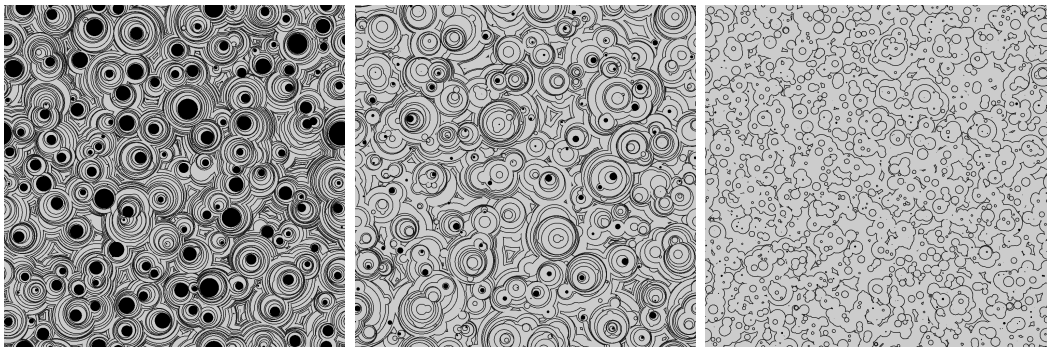

Figure 3.15: Snapshots of our MC simulations at $10\mu\text{m} \times 10\mu\text{m}$ panel at $T = 581$°C (left), $T = 592$°C (middle), and $T = 639$°C (right). The panels are $10\mu\text{m} \times 10\mu\text{m}$.

with inverted wedding cakes resulting from multi-layer evaporation, as shown in Figs. 3.14(a),(d), and Fig. 3.15(left). Note that the outer (upper) (6×6) terrace of an inverted wedding cake is of an annular shape and provides a limited surface area for $c(8 \times 2)$ nucleation. This tends to preserve these inverted wedding cake structures which are responsible for the high (6×6) coverage measured at low T in Fig. 3.7.

These inverted wedding cake structures at low T are also responsible for the long-period attaining of the steady state and the long-term decrease in (6×6) coverage (see Fig. 3.15(left)). The reason is that neighbouring wedding cake structures end up merging together to form one sole wedding cake structure after several consecutive coalescence events of terraces belonging to either structure. This mechanism of wedding cake coalescence results in a decreasing density of progressively deeper inverted wedding cakes, which explains the progressive (6×6) coverage drop after the initial peak. The coverage eventually settles as the density of wedding cakes reaches its quasi-steady-state value. However this steady state is only 'quasi', as the mechanism of wedding cake coalescence becomes more progressive but does not cease. This explains the long-term decrease in (6×6) coverage that can be seen in Fig. 3.15(left) and (right).

With increasing T, ρ increases faster than the step velocity v (Fig. 3.12) so that outer (6×6) domains transform to $c(8 \times 2)$ at smaller sizes (panels 3.14(b)-(c), 3.14(e)-(f), 3.15(centre) and (right)). Added to this, the rapidly increasing ρ approaches J_b. This means that more (6×6) terraces phase-transform without having had a new Lochkeim nucleate within them. In these instances, the next (6×6) patch will not form until the terrace reaches the critical radius R_c. This renders the wedding cake structures less pronounced (see Figs.3.14(b), (c), as well as Fig. 3.15(centre)) and decreases the overall time-averaged (6×6) coverage with increasing T (Fig. 3.7).

Eventually, ρ surpasses J_b at higher T (Fig. 3.12) and so fewer (6×6) domains undergo a second Lochkeim nucleation event during their shorter lifetime. Furthermore, the large value of J_w in this regime facilitates terrace coalescence. As

discussed earlier, coalescence can also further decrease the overall (6×6) coverage via the mechanisms (iii) and (iv) described in the previous section. As a consequence of this enhanced terrace coalescence, evaporation proceeds in a layer-by-layer mode at high T, where fewer atomic layers are exposed at the surface (see panels 3.14(c), 3.14(f), and 3.15(right)). In contrast to the low T case, this layer-by-layer fashion for the evaporation ensures a long-term steady state. The enhanced rate of $c(8 \times 2)$ nucleation and the absence of inverted wedding cake structures explains the low (6×6) coverage in this regime.

The observation of surface phase metastability during Langmuir evaporation is surprising but the phenomenon should, in fact, occur quite widely. An unstable subsurface layer, suddenly exposed by evaporation, does not necessarily have to transform directly into the most thermodynamically stable state. Instead, the unstable surface can transform into a metastable intermediate state, as empirically described by Ostwald [98]. Figures 3.14 and 3.15 illustrate the intricate interplay between the kinetic processes of Langmuir evaporation and phase metastability which determines the time-averaged coverage as a function of T (Fig. 3.7). Such phase coexistence is a result of kinetics, not thermodynamics. It is totally different from the coexistence resulting from long-range electrostatic and elastic interactions between surface domains [6, 102], which was presented above in Section 3.1.

3.6 Conclusions

In summary, we have observed surface phase metastability during Langmuir evaporation of GaAs(001). This gives rise to a dynamic phase coexistence which has previously gone unnoticed, possibly due to a lack of real-time imaging of this surface. The direct observation of metastable phases provides new insights into the kinetic processes of Langmuir evaporation. Evaporation is dominated by inverted wedding cake structures at low T, creating a significant time-averaged metastable-phase coverage. With increasing T, such structures become less pronounced, with a concomitant decrease in (6×6) coverage as evaporation tends towards a layer-by-layer mode. Often, for purposes of growth, a single surface phase is required.

Since surface phase metastability is likely to occur across a wide range of materials systems and may occur analogously during epitaxial growth as new islands nucleate. It might therefore have broad technological relevance for the growth and processing of thin films under vacuum.

Chapter 4

Mapping the Surface Phase Diagram of GaAs(001) using Droplet Epitaxy

In this chapter we map the surface phase diagram of GaAs(001) by combining droplet epitaxy with low energy electron microscopy imaging techniques. This work is published in C. X. Zheng, K. Hannikainen, Y. R. Niu, J. Tersoff, D. Gomez, J. Pereiro, and D. E. Jesson *Physical Review Materials* **3**, 124306 (2019). We interpret the phase patterns produced during droplet epitaxy using a simple model which links the spatial coordinates of phase boundaries to the free energy. Based on the observed sequential order of the phases away from the droplet edge, it is possible to obtain important new information on surface phase stability. This can be used to augment existing $T = 0\,\mathrm{K}$ phase diagrams generated by density functional theory calculations. We establish the existence of a (3×6) phase, and confirm, that the controversial (6×6) phase is thermodynamically stable over a narrow range of chemical potential.

4.1 Introduction

Droplet epitaxy has emerged as a flexible technique for growing quantum dots and more complex nanostructures [103]. In this technique, nano/microscale metal liquid

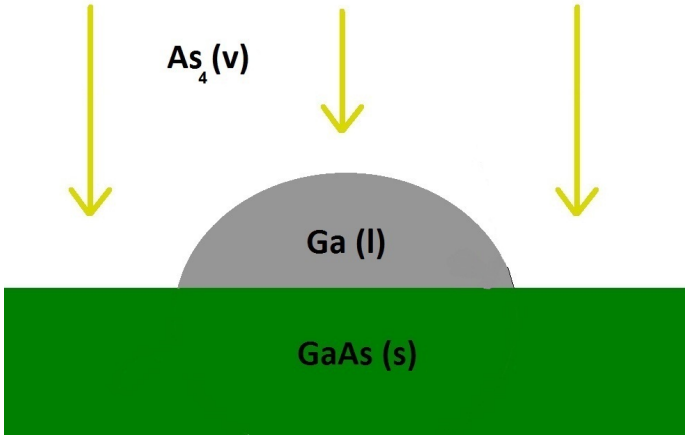

Figure 4.1: Schematic illustration of the principle of droplet epitaxy. Ga droplets are depostited on a GaAs(001) surface. These are subsequently subjected to an As_4 flux which crystallizes them. The conditions of this crystallization determine the morphology of the nanostruture that is formed.

droplets of group III are first deposited on a III-V semiconductor surface, for example Ga on GaAs(001). Then exposure to a group-V flux, such as As_4, results in the formation of an epitaxial GaAs quantum structure. This is schematically illustrated in Fig. 4.1.

Depending on the conditions of a droplet epitaxy experiment, one can achieve a certain nanostructure morphology or another. For instance, quantum dots can be achieved using low temperatures $T \sim 200°C$ and high As fluxes [7,104–108]. The low temperature limits Ga diffusion from the droplet, and the high As flux crystallizes the Ga in the immediate vicinity of the droplet. This produces GaAs mounds virtually confined to the same area as that where the Ga droplet sat. Fig. 4.2(a) shows an array of quantum dots grown in this manner. However, the low temperature at which crystallization occurs produces poor crystalline quality.

Utilizing slightly higher temperatures ($T \approx 300°C$) and more moderate As fluxes, Ga diffusion from the droplet is enhanced and the lower As flux increases the Ga diffusion length before reacting with As to form GaAs. This produces nanometric ringlike GaAs structures around the droplet known as quantum rings [8,109,109–115, 115]. Semiconductor nanometric rings are interesting nanostructures as electrons confined within them undergo a topology related quantum interference effect called the Aharonov-Bohm effect [116]. The magnetic properties of quantum rings are particularly interesting, as these can induce persistent current within the ring [117].

Different types of ring morphologies can be grown by tuning the growth conditions. Even multiple rings can be grown, as those shown in Fig. 4.2(b). In this particular experiment (see Ref. [8]), the droplet was annealed under As flux at 4 different temperatures: 250, 300, 325, 350 °C. The first 3 temperatures for 20 seconds, and the last for 20 min, to ensure the crystallization of the droplet. Each annealing temperature produced each one of the GaAs rings. The ring closest to the droplet was produced at the lowest temperature, and each successive ring was produced with each increase in temperature. This is because, as was explained in Section 2.2, adatom diffusion is enhanced with increasing temperature, so that Ga adatoms are able to diffuse farther on the surface before being crystallized.

Annealing Ga droplets at high temperature ($T \sim 550°\text{C} \rightarrow 600°\text{C}$) and a low As flux (merely the As background pressure in the growth chamber) produces nanohole morphologies like that shown in Fig. 4.2(c). Under these conditions, the Ga from the droplet diffuses readily and is crystallized all across the surface. While this happens GaAs is deposited at the contact line, and the droplet drills into the GaAs surface simultaneously, thereby producing the observed nanohole morphology. This technique is named local droplet etching (LDE). The physical mechanism by which it occurs will be explained in more detail in Chapter 5. In contrast to *ex situ* etching techniques, LDE is an impurity and defect-free technique for 'nanopatterning' given it occurs under epitaxial growth conditions. Arrays of nanoholes produced by LDE can be used as templates for subsequent filling with quantum dots [11, 118]. This method of quantum dot fabrication is a good alternative to the well-known Stranski-Krastanov method when the dot and the substrate form a lattice-matched system. Its most attractive feature is that it produces high-temperature strain-free quantum dots. [11, 119, 120].

In this work we adapt the droplet expitaxy technique as a novel tool for mapping the surface phase diagram of GaAs(001) by combining it with advanced LEEM imaging [5]. As was metioned in Chapter 1, the GaAs(001) surface is of great importance for electronic applications and has been intensively studied over the years (see, e.g., Refs. [1, 2, 66–76]). Surface phases with different structures and

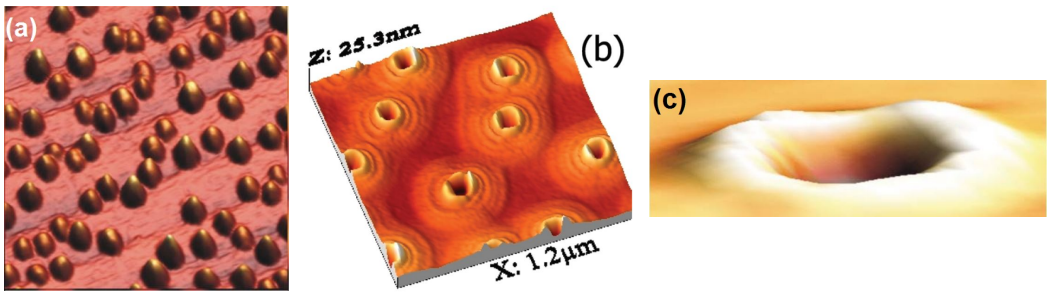

Figure 4.2: (a) AFM image of an array of GaAs quantum dots produced by droplet epitaxy. The width of the panel equals 450 nm. Reprinted from Ref. [7]. (b) AFM image of a sample displaying multiple concentric quantum ring structures prepared by droplet epitaxy. The inner ring is priduced by GaAs deposition at the contact line, whilst the outer rings are produced by Ga diffusing out from the droplet and reacting with the incoming As flux. Up to four outer rings are produced by annealing the sample at 250, 300, 325, and 350°C. Each ring corresponds to one temperature, the innermost one corresponding to the lowest temperature and the outer ring corresponding to the highest temperature. Reprinted from Ref. [8]. (c) AFM image of a nanohole prepared by high temperature ($T = 540$°C) annealing of a Ga droplet under a low As background pressure. The width of the panel corresponds to ≈ 400 nm. Reprinted from Ref. [9].

different compositions are used in the growth of optoelectronic materials, InGaAs quantum devices, and dilute magnetic semiconductors by molecular beam epitaxy (MBE). This has led to significant efforts to understand and control the stability of surface phases as a function of experimental conditions. As was decribed in Section 2.3, the conventional approach is to calculate the Gibbs surface free energy as a function of Ga surface chemical potential μ_{Ga} (or equivalently As chemical potential μ_{As}, since the sum is fixed [52, 78]). Then μ_{Ga} (or μ_{As}) can be related to experimental conditions (see, for example [2, 78]). However, μ_{Ga} is difficult to control experimentally since it depends sensitively on temperature [37] and material deposition [121]. In a recent publication [4], efforts were made to control μ_{Ga} by slowly varying the substrate temperature in the presence of Ga droplets [4]. In this study, the Ga-rich (4×6) (see phase diagram in Fig. (2.4)) was observed coexisting with an ultrarich novel $c(2 \times 12)$ phase using LEED. It is argued that the surface approaches equilibrium with the Ga droplets (at liquidus Ga chemical potential μ^l_{Ga}) and hence increases in Ga-richness when cooling below ~ 530°C. This is due to a smaller activation barrier for Ga attachment/detachment than for Ga evaporation from the surface. However, key questions still remain regarding phase stability across

the wider range of μ_{Ga}, extending towards and including the As-rich regime.

During droplet epitaxy under standard conditions, there usually forms a gradient of Ga adatom chemical potential with distance from the Ga droplet. Using LEEM we can directly observe a sequence of distinct surface phases reflecting the spatially varying chemical potential. By determining which phases occur, and their ordering from the droplet edge, we can map out the surface phase diagram across a wide range of continuously varying μ_{Ga} at fixed temperature. In this way we will establish the existence of a (3×6) phase. As we will see, additional experiments, combined with theoretical modeling of the chemical potential gradient, allow us to confirm that the controversial (6×6) phase is thermodynamically stable over a narrow range of chemical potential. These phases are absent in the theoretical $T = 0\,\mathrm{K}$ phase diagram, and we will discuss how thermal effects may stabilize them at experimental temperatures.

Although we apply a novel combination of LEEM and droplet epitaxy to specifically study the GaAs(001) surface, the methods presented here should be general and are highly complementary to density functional theory (DFT) calculations. As such, we believe this specific study presents a novel method for mapping surface phase diagrams across a wide range of material systems. This includes other technologically important III-V compounds, such as nitrides.

4.2 Sample Preparation

Our experiments were performed in the ultrahigh-vacuum (UHV) LEEM-MBE system [36] described in Section 2.8. Temperatures were measured using an infrared pyrometer calibrated to the congruent evaporation temperature of 625 °C [52, 121]. As was explained in Chapter 2, we degass an undoped GaAs(001) sample at 300 °C for 24 h and then annealed at 580 °C for 2 h to remove the surface oxide. We planarise the surface by annealing above the congruent evaporation temperature at 650 °C and producing Ga droplets of radius $\sim 1\,\mu$m. These are then allowed to run across the surface [37,92], creating smooth planar (001) regions on which we perform our droplet epitaxy imaging experiments [93].

4.3 Results and Discussion

4.3.1 Droplet Epitaxy Phase Patterns

Figure 4.3 contains a bright field LEEM image of a Ga droplet on GaAs(001) under an As_4 flux of 10^{-5} Torr beam effective pressure (BEP) at 550 °C. As can be observed, there is a stationary, dark concentric ring surrounding the droplet enclosed by boundaries I and II. The ring is slightly elliptical, due to anisotropic Ga surface diffusion on GaAs (001). The contrast is a consequence of the spatial variation in surface phases, which produce variations in incident electron reflectivity, as was explained in Section 2.4.1 (see, for example, Ref. [122]). We term this contrast variation a droplet epitaxy phase pattern (DEPP). By means of microspot low energy electron diffraction (μLEED) we identify the inner bright region as corresponding to the $c(8 \times 2)$ structure. We further identify the outer bright region as $\beta 2(2 \times 4)$ and the dark ring itself as a (3×6) surface reconstruction. However, as we show below, we find boundary I is also associated with a narrow region of (6×6) phase.

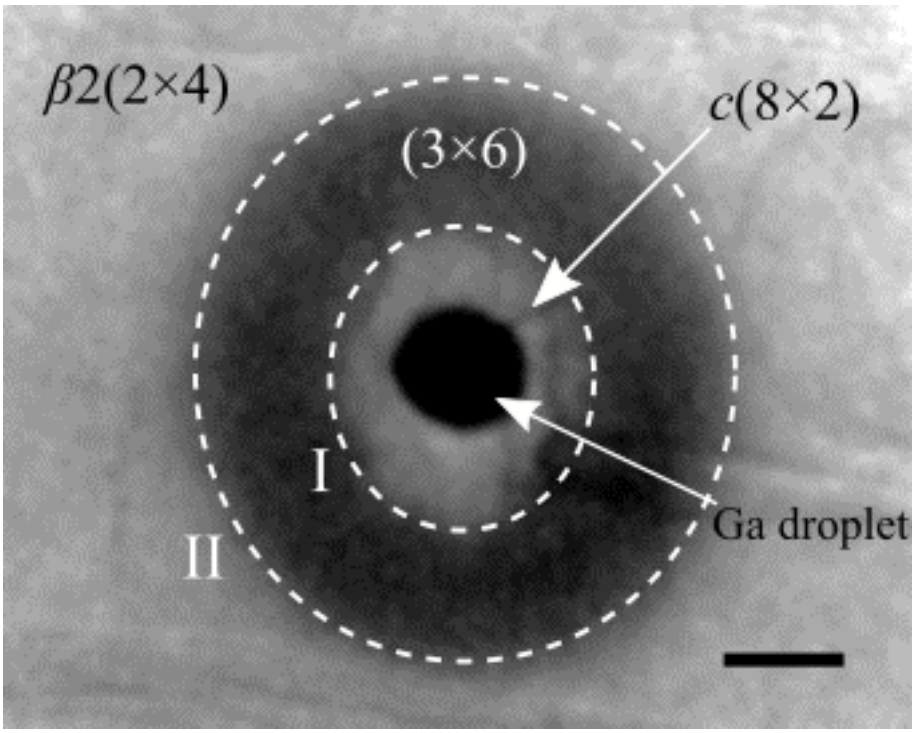

Figure 4.3: Droplet epitaxy phase pattern (DEPP) of GaAs(001). The bright-field contrast spatially separates surface phases surrounding a central droplet. The scale bar corresponds to 2 μm.

To explain the origin of this phase pattern and establish the link to surface free

energy, we consider a simple model for DEPP formation. The Ga droplet acts as a source of Ga adatoms which interact with the surface and any As adatoms. To calculate the Ga adatom concentration surrounding the droplet, let us consider a random array of droplets of radius r_D (assumed constant throughout the course of the experiment), with typical nearest neighbor distance $2L$ (with $L \gg r_D$). The droplet array is subjected to an As flux F_{As} and the reaction-diffusion equation for the Ga concentration outside the droplet at radial coordinate r and time t is,

$$\frac{\partial C_{\mathrm{Ga}}}{\partial t} = D_{\mathrm{Ga}} \left(\frac{\partial^2 C_{\mathrm{Ga}}}{\partial r^2} + \frac{1}{r} \frac{\partial C_{\mathrm{Ga}}}{\partial r} \right) - k_r \left[C_{\mathrm{Ga}} C_{\mathrm{As}} - (C_{\mathrm{Ga}} C_{\mathrm{As}})_{eq} \right]. \tag{4.1}$$

This equation was derived previously in Section 2.2; C_{As} and C_{Ga} are the respective As and Ga surface adatom concentrations and D_{Ga} is the Ga diffusion coefficient. k_r is a reaction rate constant governing the reaction between As and Ga to form GaAs solid and $(C_{\mathrm{Ga}} C_{\mathrm{As}})_{eq}$ is the adatom concentration product in equilibrium with the solid. We neglect Ga adatom desorption into the vacuum. As a reasonable approximation, the geometric distribution of the droplet array renders Eq. (4.1) with radial symmetry and we impose the boundary condition $\partial C_{\mathrm{Ga}}/\partial r = 0$ at $r = L$.

Above 350 °C, the As residence time τ_{As} is short [39], much shorter than other relevant timescales. Compared to desorption, reaction with Ga is only a small perturbation (which we neglect) to the As concentration. We therefore treat the As density as uniform, with steady-state value $C_{\mathrm{As}} = F_{\mathrm{As}} \tau_{\mathrm{As}}$ for sufficiently large flux F_{As}. Furthermore, we can assume it comes instantly into steady state with flux (on a timescale τ_{As}). This is equivalent to $\tau_{\mathrm{As}} \ll \tau_{\mathrm{Ga}} = 1/(k_r C_{\mathrm{As}})$ where τ_{Ga} is the Ga adatom mean lifetime before reaction with As.

Given $L_{\mathrm{Ga}} = \sqrt{D_{\mathrm{Ga}} \tau_{\mathrm{Ga}}}$ is the Ga diffusion length before reacting with As, then for $L \gg L_{\mathrm{Ga}}$, one can show that the steady-state solution to Eq. (4.1), i.e. with $\partial C_{\mathrm{Ga}}/\partial t = 0$, is

$$C_{\mathrm{Ga}}(r) = B K_0(r/L_{\mathrm{Ga}}) + \frac{(C_{\mathrm{Ga}} C_{\mathrm{As}})_{eq}}{F_{\mathrm{As}} \tau_{\mathrm{As}}}, \tag{4.2}$$

where B is a constant for given temperture T and flux F_{As} (see Appendix B). Here, K_0 is a modified Bessel Function of the second kind [123]. In the limit of fast Ga

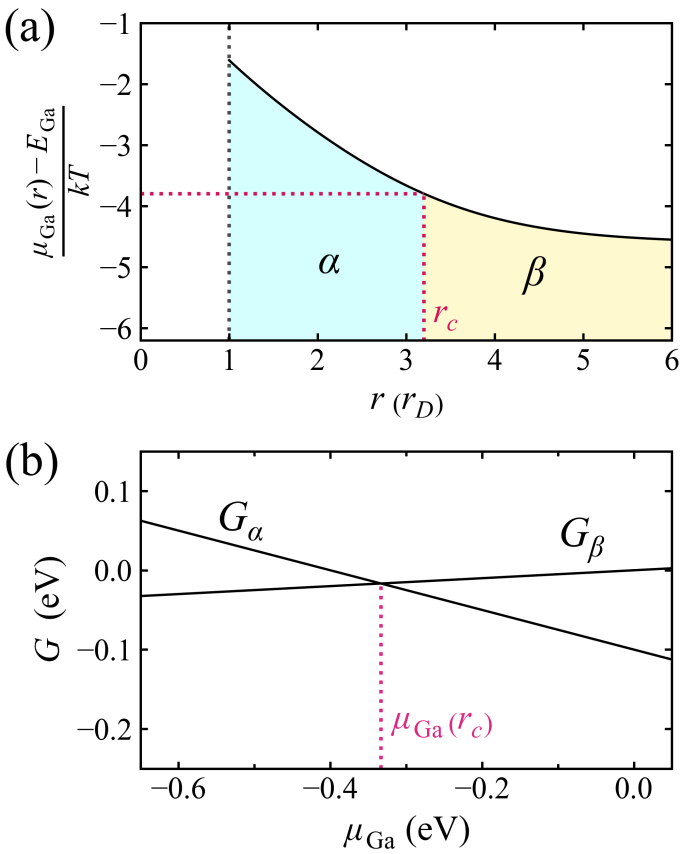

Figure 4.4: (a) Ga chemical potential at radial position r away from the droplet edge located at r_D. For illustration we have taken $C^l_{\rm Ga}/\nu_{\rm Ga} = 0.2$, $C^L_{\rm Ga}/\nu_{\rm Ga} = 0.01$ and $r_D/L_{\rm Ga} = 1$ (see Appendix A). (b) Schematic representation of the free energy G (per (1×1) unit cell) of phases α and β plotted as a function of $\mu_{\rm Ga}$. The phases have the same free energy at $\mu_{\rm Ga}(r_c)$ corresponding to radial position r_c in (a).

attachment/detachment from the droplet edge, the droplet shrinkage is diffusion limited and $C_{\rm Ga}|_{r=r_D} = C^l_{\rm Ga}$ where $C^l_{\rm Ga}$ is the Ga adatom concentration in equilibrium with the liquid Ga droplet (as given in Section 2.2). Using the relationship between the surface adatom concentration and chemical potential derived in Chapter 2, that is, $\mu_{\rm Ga} = E_{\rm Ga} + kT\ln\left(C_{\rm Ga}/\nu_{\rm Ga}\right)$ [56], the Ga chemical potential at radial position r and temperature T, for flux $F_{\rm As}$ is simply,

$$\mu_{\rm Ga}\left(r\right) = E_{\rm Ga} + kT\ln\left(\frac{BK_0\left(r/L_{\rm Ga}\right)}{\nu_{\rm Ga}} + \frac{\left(C_{\rm Ga}C_{\rm As}\right)_{eq}}{\nu_{\rm Ga}F_{\rm As}\tau_{\rm As}}\right), \tag{4.3}$$

which is plotted in Fig. 4.4(a). Here, k is Boltzmann's constant and we assume the Ga adatoms may sit at $\nu_{\rm Ga}$ equivalent surface sites per unit area, of energy $E_{\rm Ga}$. For simplicity, we neglect vibrational entropy contributions.

The incoming As flux therefore reacts with surface Ga to form GaAs. Ga adatoms

are replenished by the droplet which acts as a source of Ga adatoms. This results in a monotonically decreasing Ga chemical potential as a function of radial distance from the droplet edge, as illustrated in Fig. 4.4(a). The spatial phase pattern observed in Fig. 4.3 can now be explained using this simple model, as follows. Consider first a radial position r_c associated with the boundary between phases α and β, as represented schematically in Fig. 4.4(a). Such a boundary might approximate experimental boundaries I or II in Fig. 4.3, for example. This is associated with a chemical potential $\mu_{\mathrm{Ga}}(r_c)$ such that the surface free energies (per (1×1) cell) of the two phases are equal,

$$G_\alpha\left(\mu_{\mathrm{Ga}}\left(r_c\right)\right) = G_\beta\left(\mu_{\mathrm{Ga}}\left(r_c\right)\right), \tag{4.4}$$

as shown schematically in Fig. 4.4(b). In other words, one will observe a phase boundary where the Ga chemical potential gradient attains a critical value where the free energy lines corresponding to two phases cross each other on the surface phase diagram. Thus, the real-space position of phase boundaries around droplets can be used to map surface free energies as a function of chemical potential.

DEPPs, as contained in Fig. 4.3, provide a continuously varying [124] and monotonically decreasing μ_{Ga} and are, therefore, a perfect tool for carefully and extensively exploring μ_{Ga} phase space. However, the structure of the surface within the dark ring (see Fig. 4.3) may be difficult to analyse even when using μLEED. In order to improve our spatial μLEED resolution we can make use of the time dependence of DEPP formation and hence the varying width of the dark ring.

4.3.2 Time-Dependent Droplet Epitaxy Phase Patterns; Improved Resolution

To explain how the resolution of the technique can be improved we consider the time-dependent droplet epitaxy experiment contained in Fig. 4.5. Panel (a) shows a droplet and smooth planar trail region, created by previous droplet motion, which we utilize for our imaging experiments [93]. Initially, the sample is at 550 °C with the As

shutter closed. Under these conditions the entire trail region is composed of the Ga-rich $c(8 \times 2)$ phase. If it were not for the presence of the droplets, the surface might have shown some (6×6) at these temperatures [4]. However, the droplets supply the surface with Ga, increasing the steady-state surface μ_{Ga}. Upon opening the As shutter at $t = 0$, boundaries I and II can be seen moving inwards towards the droplet (Fig. 4.5(b)). The radial position of boundaries I and II is shown in Fig. 4.6(b) as a function of time. At $t = 33\,\mathrm{s}$ they approach their steady-state positions, at which point the As is turned off. The boundaries then move outwards along the trail (Fig. 4.5(c)), as displayed in Fig. 4.6(b). An experimental LEEM movie of phase boundary motion dynamics when the As flux is turned on and off, corresponding to the sequence of Fig. 4.5 can be found in the supplementary material of Ref. [41] at https://journals.aps.org/prmaterials/supplemental/10.1103/PhysRevMaterials.3.124603.

Time-resolved μLEED data can be acquired as the different phases move along the trail. The illumination aperture used to collect μLEED data can be strategically placed at a given trail position to obtain diffraction information as a function of time. Experimentally, we find that improved chemical potential resolution and phase identification occurs when the aperture is placed at a position away from the droplet edge, as indicated in Fig. 4.5(a). Furthermore, when the As flux is turned off and the phase boundaries move outward, their motion is slower than when the As is turned on (and they move inward). This results in improved time resolution when the As flux is turned off.

Fig. 4.6(a) displays the μLEED diffraction patterns (i) to (iv) obtained from the illumination aperture position indicated in Fig. 4.5(a). The patterns were acquired at the corresponding times indicated by the crosses in Fig. 4.6(b). We also show schematic diffraction patterns for clarity, where large circles indicate the positions of (1×1) spots. Diffraction patterns (iv), (iii) and (i) correspond to the $\beta 2(2 \times 4)$, (3×6) and $c(8 \times 2)$ phases, respectively, which is consistent with Fig. 4.3. However, we surprisingly obtain a new diffraction pattern at time (ii), close to the passing of boundary I. The observed μLEED diffraction pattern is a superposition of (6×6) and $c(8 \times 2)$ phases as shown in Fig. 4.6(a). This indicates the presence of an

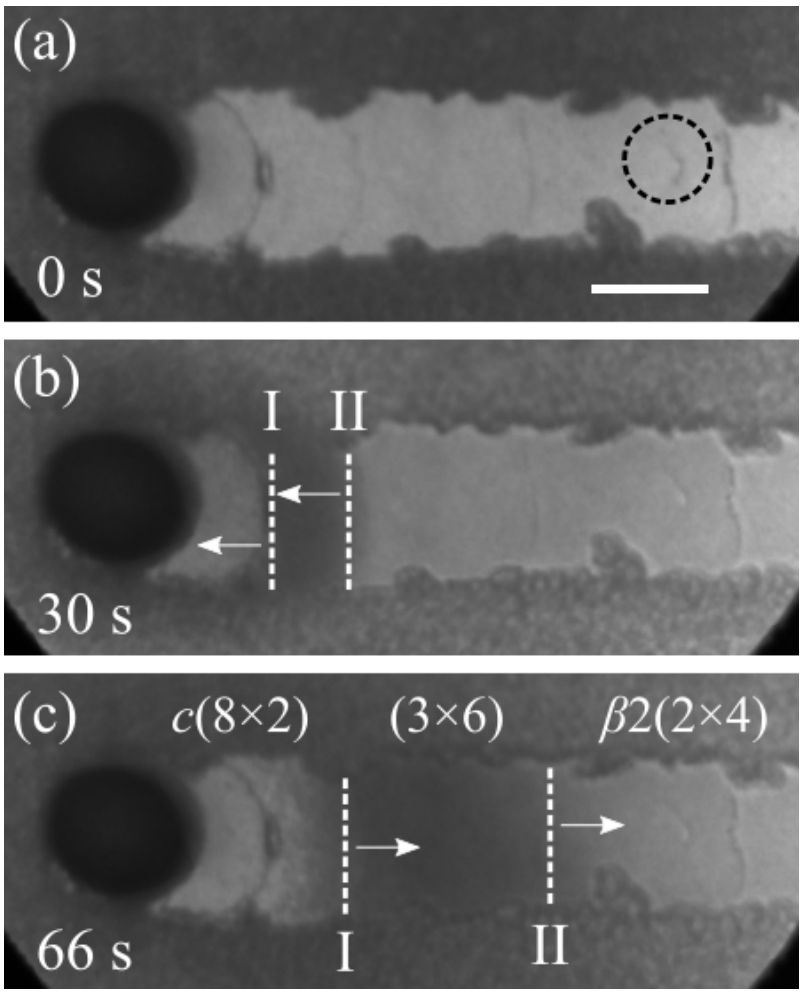

Figure 4.5: Bright field LEEM image of a Ga droplet and smooth trail region of GaAs(001). (a) at $t = 0\,\mathrm{s}$ before the As flux is turned on. (b) 30 s after the As flux is turned on and (c) 33 s after the As flux is turned off (i.e. 66 s after it was first turned on). The black dashed circle in (a) indicates the position of the illumination aperture, and the scale bar corresponds to $2\,\mu\mathrm{m}$. The sample temperature is 550 °C.

additional (6×6) phase in this region.

In order to understand the phase boundary motion on turning As on and off and the apparent improvement in μ_{Ga} resolution away from the droplet edge, we turn to the reaction-diffusion equation of Eq. (4.1). Initially, before the As flux is turned on, the surface is in quasi-equilibrium with the liquid Ga droplets and the Ga adatom density is equal to C^l_{Ga} across the entire surface. This corresponds to the initial, uniform Ga adatom chemical potential profile $\mu^0_{\mathrm{Ga}}(r) = \mu^l_{\mathrm{Ga}}$ at $t = 0$ as shown in Fig. 4.7(a). This flat initial chemical potential profile lies above critical chemical potentials $\mu^{\mathrm{I}}_{\mathrm{Ga}}$ and $\mu^{\mathrm{II}}_{\mathrm{Ga}}$ (represented by dotted lines), which respectively correspond to boundaries I and II (see Fig. 4.3 and 4.5(c)). Therefore, the entire trail for zero As flux displays the $c(8 \times 2)$ reconstruction (Fig. 4.5(a)) (see also [4]).

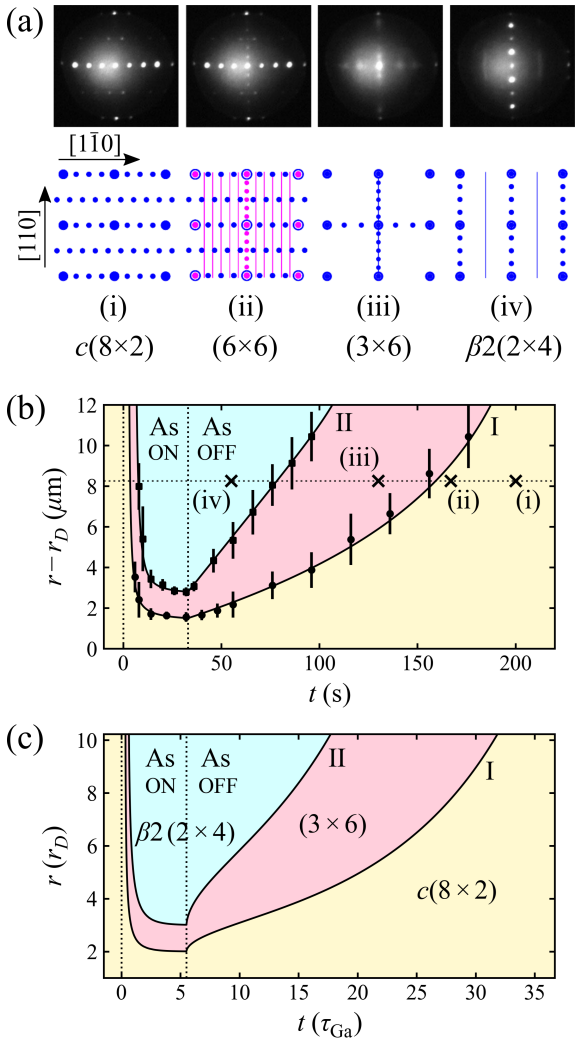

Figure 4.6: (a) Time-resolved μLEED data collected from the illumination aperture shown in Fig. 4.5(a) located 8 μm from the droplet. Schematic diffraction patterns are also shown, where large circles indicate the positions of (1×1) spots. (b) Measured r vs t trajectories of phase boundaries I and II, when turning the As flux on and off. The horizontal dotted line marks the position of the aperture in Fig. 4.5(a), with the crosses corresponding to the acquisition times of the LEED data contained in (a). The dotted vertical lines represent the times at which the As shutter was opened and closed. (c) Theoretical trajectories of boundaries I and II calculated from Eq. 4.1 (see Appendix 2). Time is given in units of reaction time $\tau_{\mathrm{Ga}} = (k_r F_{\mathrm{As}} \tau_{\mathrm{As}})^{-1}$, and radial coordiante r is given in droplet radii r_D. The computational parameters are set to the representative values of $C^l_{\mathrm{Ga}}/\nu_{\mathrm{Ga}} = 0.25$, $C^L_{\mathrm{Ga}}/\nu_{\mathrm{Ga}} = 5 \times 10^{-3}$, $\rho_D = 0.1$, and $\rho_L = 7$. The chemical potentials defining boundaries I and II give stationary boundary positions at $r_{\mathrm{I}}/r_D = 2$ and $r_{\mathrm{II}}/r_D = 3$, respectively.

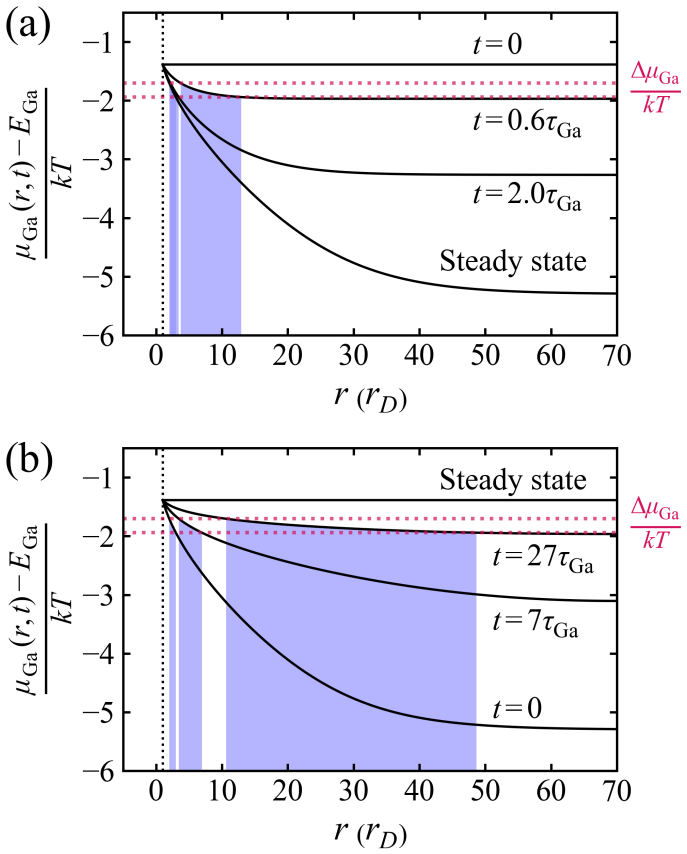

Figure 4.7: Ga chemical potential profiles $\mu_{\mathrm{Ga}}(r,t)$ after turning the As flux (a) on, and (b) off. The droplet edge is located at $r = r_D$. The critical chemical potentials $\mu^{\mathrm{I}}_{\mathrm{Ga}}$ and $\mu^{\mathrm{II}}_{\mathrm{Ga}}$ corresponding to boundaries I and II are represented by the upper and lower horizontal dashed lines, respectively. The shaded regions represent the evolving real-space region Δr corresponding to $\Delta\mu_{\mathrm{Ga}} = \mu^{\mathrm{I}}_{\mathrm{Ga}} - \mu^{\mathrm{II}}_{\mathrm{Ga}}$ (each shaded region relates to one instantaneous $\mu_{\mathrm{Ga}}(r,t)$-profile, where time is displayed in units of $\tau_{\mathrm{Ga}} = (k_r F_{\mathrm{As}} \tau_{\mathrm{As}})^{-1}$ in both (a) and (b)). We set the computational parameters to the representative values of $C^{l}_{\mathrm{Ga}}/\nu_{\mathrm{Ga}} = 0.25$, $C^{L}_{\mathrm{Ga}}/\nu_{\mathrm{Ga}} = 5 \times 10^{-3}$, $\rho_D = 0.1$, and $\rho_L = 7$ (see the Appendix). The values of $\mu^{\mathrm{I}}_{\mathrm{Ga}}$ and $\mu^{\mathrm{II}}_{\mathrm{Ga}}$ give stationary boundary positions at $r_{\mathrm{I}}/r_D = 2$ and $r_{\mathrm{II}}/r_D = 3$, respectively.

Before opening the As flux, the As concentration is that of quasi-equilibrium with the solid, that is, $C^0_{\rm As} = (C_{\rm Ga}C_{\rm As})_{eq}/C^l_{\rm Ga}$. Upon turning on the As flux at $t = 0$, we assume the As concentration $C_{\rm As}$ increases instantly to $F_{\rm As}\tau_{\rm As}$ given the fast timescale of As evaporation. Under these conditions we solve the reaction-diffusion Eq. (4.1) for $C_{\rm Ga}(r,t)$ (and hence $\mu_{\rm Ga}(r,t)$) at later times $t > 0$ (see Appendix B for details). This means setting $C_{\rm As} = F_{\rm As}\tau_{\rm As}$ in Eq. (4.1) and an initial $C_{\rm Ga}$-profile equal to $C^l_{\rm Ga}$. See the movie simulating the time evolution of $\mu_{\rm Ga}$ profiles in the supplemental material of Ref. [41] at https://journals.aps.org/prmaterials/supplemental/10.1103/P

Figure 4.7(a) shows the evolution of the Ga chemical potential profiles $\mu_{\rm Ga}(r,t)$ upon turning on the As flux. As can be observed, far from the droplet the Ga chemical potential decreases with time as the incoming As reacts with surface Ga, on a timescale determined by the reaction time $\tau_{\rm Ga} = (k_r F_{\rm As}\tau_{\rm As})^{-1}$. However, the droplet readily replenishes the surface with Ga. This pins the chemical potential at the droplet edge at the liquidus value $\mu^l_{\rm Ga}$. Eventually, $\mu_{\rm Ga}(r,t)$ crosses $\mu^{\rm I}_{\rm Ga}$ at some distance from the droplet. At this instant, boundary I appears at radial coordinate $r_{\rm I}$ such that $\mu_{\rm Ga}(r_{\rm I},t) = \mu^{\rm I}_{\rm Ga}$. As $\mu_{\rm Ga}(r,t)$ continues to decreases with time, $r_{\rm I}$ and boundary I move inwards toward the droplet. Similarly, boundary II appears at $r_{\rm II}$ at a later time (where $\mu_{\rm Ga}(r_{\rm II},t) = \mu^{\rm II}_{\rm Ga}$) and also moves inwards along the trail with time. Eventually, both boundaries reach their steady-state positions (cf. Figs 4.3 and 4.4) when the steady-state $\mu_{\rm Ga}(r,t)$ profile is attained.

When the As flux is turned off, we assume that the As adatom concentration $C_{\rm As}$ goes instantly from $F_{\rm As}\tau_{\rm As}$ back to its original zero-flux value $C^0_{\rm As}$. This assumption is consistent with the fast timescale of As evaporation, i.e., a small $\tau_{\rm As}$. In calculating now the evolving Ga adatom concentration profiles $C_{\rm Ga}(r,t)$ (and hence the chemical potential profiles $\mu_{\rm Ga}$), we note that the $C_{\rm As}$ in Eq. (4.1) is now $C_{\rm As} = C^0_{\rm As}$, and the initial Ga concentration profile is now the $C_{\rm Ga}(r)$ of Eq. (4.2).

As can be observed in Fig. 4.7(b), $\mu_{\rm Ga}(r,t)$ begins to rise as the bulk solid and the droplets supply the surface with Ga. This causes the phase boundary positions $r_{\rm I}(t)$ and $r_{\rm II}(t)$ to move away from the droplet. Eventually both phase boundaries accelerate and disappear as soon as $\mu_{\rm Ga}(r,t)$ exceeds $\mu^{\rm II}_{\rm Ga}$ and $\mu^{\rm I}_{\rm Ga}$, leaving behind a

stable $c(8 \times 2)$ surface.

Having calculated the evolving chemical potental profiles $\mu_{\mathrm{Ga}}(r,t)$ when turning the As flux on and off, one can easily calculate theoretical boundary trajectories $r_{\mathrm{I}}(t)$ and $r_{\mathrm{II}}(t)$. These are simply given by equations $\mu_{\mathrm{Ga}}(r,t) = \mu_{\mathrm{Ga}}^{\mathrm{I}}$ and $\mu_{\mathrm{Ga}}(r,t) = \mu_{\mathrm{Ga}}^{\mathrm{II}}$. The solutions are shown in Fig. 4.6(c).

When the As flux is first turned on, the chemical potential profile $\mu_{\mathrm{Ga}}(r,t)$ first crosses $\mu_{\mathrm{Ga}}^{\mathrm{I}}$ at a large distance from the droplet. At this point, $\mu_{\mathrm{Ga}}(r,t)$ is almost tangential to $\mu_{\mathrm{Ga}}^{\mathrm{I}}$ which means that boundary I propagates rapidly with time (Fig 4.6(c)). However, as the boundary approaches the droplet it encounters a gradient in $\mu_{\mathrm{Ga}}(r,t)$ and therefore slows down. It gradually converges to a stationary position, determined by the steady-state $\mu_{\mathrm{Ga}}(r)$ given by Eq. (4.3). All of these qualitative characteristics of the calculated boundary trajectories in Fig. 4.6(c) as As flux is turned on are in excellent agreement with the experimental data in Fig. 4.6(b).

When As is turned off, it can be clearly seen from Fig. 4.6(b) and (c) that the As-off trajectories are not time-reversals of the As-on trajectories. Furthermore, the overall timescale of the evolution is notably longer, as manifested by the larger τ_{Ga}, which is now $\tau_{\mathrm{Ga}}^{0} = 1/(k_r C_{\mathrm{As}}^{0})$. This is because the initial disequilibrium between the adatom population and the solid is smaller, i.e. the initial rate of GaAs decomposition is smaller than the initial rate of crystal growth when turning the As flux on. In addition, the outgoing boundaries do not accelerate until far from the droplet. This reflects the contrasting geometries of the initial μ_{Ga}-profiles when As is turned on or off. Also, the re-supply of surface Ga from the droplets in the absence of As flux progressively flattens out the $\mu_{\mathrm{Ga}}(r,t)$ profile, whereas in As-on evolution the initially flat chemical potential profile quickly curves close to the droplet (see Fig. 4.7(a) and (b)). Note that this slower As-off boundary evolution provides improved time resolution compared with the As-on boundary dynamics when obtaining the μLEED diffraction patterns contained in Fig. 4.6(a). Again, the overall simulated behavior of the boundary trajectories when As is turned off (Fig. 4.6(c)) is in good qualitative agreement with experiment (Fig. 4.6(b)).

Figure 4.7 shows clearly why the chemical potential resolution increases with

distance from the droplet. Consider the chemical potential range $\Delta\mu_{\mathrm{Ga}} = \mu_{\mathrm{Ga}}^{\mathrm{I}} - \mu_{\mathrm{Ga}}^{\mathrm{II}}$ which corresponds to the stability of the (3×6) phase. For a given $\mu_{\mathrm{Ga}}(r,t)$, this will correspond to a region in real-space $\Delta r = r_{\mathrm{II}} - r_{\mathrm{I}}$. For small $\Delta\mu_{\mathrm{Ga}}$ we have $\Delta r = \Delta\mu_{\mathrm{Ga}}/|\partial\mu_{\mathrm{Ga}}/\partial r|$, where $\partial\mu_{\mathrm{Ga}}/\partial r$ is the gradient within Δr. At As-on steady state, this region lies close to the droplet, and the steep gradient gives a narrow Δr, as can be seen in Fig. 4.7(a). Such a spatially narrow ring is difficult to fully resolve with μLEED. However, by observing DEPPs before steady state is attained, the lower μ_{Ga}-gradient associated with incoming or outgoing boundaries when As is turned on or off translates into a wider Δr in real-space (see Figs. 4.7(a) and (b)), thus improving the resolution. This explains why improved phase discrimination occurs when the illumination aperture is placed at a position away from the droplet, as indicated in Fig. 4.5(a). We may therefore utilize the time dependence of the adatom concentration to control the chemical potential gradient, and hence improve the resolution of the DEPP technique.

4.3.3 Mapping the Surface Phase Diagram of GaAs(001) using Time-Dependent DEPPs

To study the structure of boundary I in more detail we can now take advantage of the time dependence of the DEPP technique. Combining this with selected energy dark-field (SEDF) LEEM [5] (see Section 2.4.4) we can combine dark-field images corresponding to different surface phases and assign colors to phase-specific intensities, thereby providing a composite surface phase map [5]. Fig. 4.8 displays such a map where blue, green, orange and yellow correspond to $\beta 2(2 \times 4)$, (3×6), (6×6) and $c(8 \times 2)$ phases, respectively. This map has been obtained following the As flux being turned on as the phase boundaries move towards the droplet. This map optimally reveals the sequential order of the phases and also clearly resolves boundary I in more detail. It clearly shows a stable (6×6) region, as well as a region of phase intermixing between the (6×6) and $c(8 \times 2)$ phases. In this section we show how such information can provide important new insight into the GaAs(001) phase diagram.

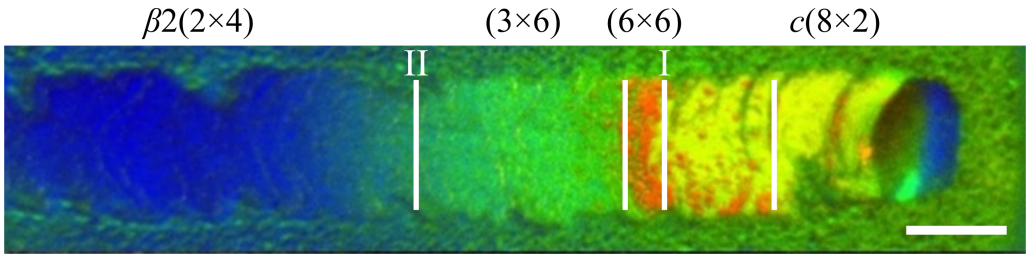

Figure 4.8: SEDF LEEM image where blue, green, orange and yellow correspond to $\beta 2(2 \times 4)$, (3×6), (6×6) and $c(8 \times 2)$ phases, respectively (see [5]). This map clearly resolves boundary I in more detail, revealing a stable (6×6) region and phase intermixing between the (6×6) and $c(8 \times 2)$ phases. The scale bar corresponds to 2 μm. Ga droplet on right.

As mentioned earlier in Section 2.3, GaAs(001) exhibits many surface reconstructions [1, 2, 66–76]. This is because the structure of surface is sensitive to the experimental conditions in the chamber. As explained in Section 2.3, in attempting to understand the stability of various phases, the standard procedure is to calculate the zero temperature formation free energies of the different structures using DFT, and plot these against Ga chemical potential μ_{Ga} (see, for example, [1, 10, 52, 78]). An example of such a phase diagram is that of Fig. 2.4 in Chapter 2. The aim is then to relate μ_{Ga} to experimental conditions [78]. However, the fine control of μ_{Ga} in conventional experiments is difficult due to the sensitivity of chemical potential to temperature and deposition. In addition, uncertainty as to whether surfaces have attained equilibrium due to kinetic limitations are also major limiting factors [1]. However, the DEPPs contained in Figs 4.3 and 4.8 provide a continuous and monotonically decreasing μ_{Ga} [124] and therefore are a convenient tool for carefully exploring the μ_{Ga} phase space. As we will now demonstrate, this can provide important new information on surface free energy and resolve key issues in GaAs(001) surface thermodynamics.

The (6×6) phase observed in Fig. 4.13(a) is very controversial [1, 10, 69, 73, 76, 125]. However, it can be easily prepared. For example, one can first heat the surface to about $\sim 600^{\circ}$C to observe the $c(8 \times 2)$ structure (in the absence of droplets or fluxes), and then cool it below $\sim 525^{\circ}$C to see the pure (6×6) structure [1, 4]. However, the atomic structure and energetics of the (6×6) structure are not well understood [10, 73, 125]. Several models for the structure have been proposed, such

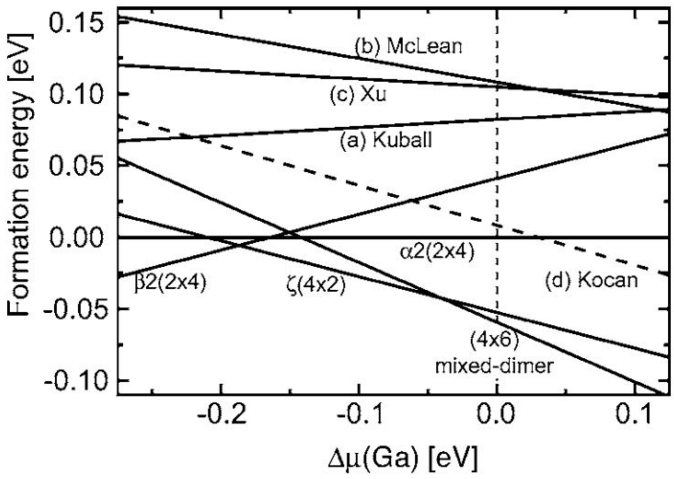

Figure 4.9: Phase diagram of the GaAs(001) surface containing the DFT-calculated formation energy lines of the McLean, Xu, Kuball, and Kocan models of the (6×6) structures. As can be seen, none of these structures are stable for any value of μ_{Ga}. Reprinted from Ref. [10].

as those of Kuball [125], McLean [69], Xu [126] or Kocan [127]. However, all of these structures present very high formation energies, and are unstable for all values of μ_{Ga}. This can be clearly seen in the phase diagram Fig. 4.9.

As shown in Fig. 4.9, the Kocan model is the structure with lowest free energy. The atomic configuration of this structure is shown in Fig. 4.10. It consists of crests of Ga-As dimers running along the $[1\bar{1}0]$ direction, separated by troughs. The $\times 6$ periodicity along the [110] is given by the distance between the crests, while the periodicity in the $[1\bar{1}0]$ is given by the atomic arrangement within the troughs.

Variants of the Kocan model have been considered with different proportions of missing As-As dimers within the troughs [10]. The structure with one out of four As-As dimers missing presents the lowest formation energy compared with other structural models proposed to date, and produces a (12×6)-sized unit cell. The atomic configuration of this (12×6) variant of the Kocan model is shown in Fig. 4.11.

The DFT-calculated free energy line of this (12×6) structure is shown in the phase diagram of Fig. 4.12 (see Ref. [10]). It also shows the lines corresponding to the models with other proportions of missing As-As dimers. The standard Kocan (6×6) unit cell can have up to two As-As dimers (see Fig. 4.10). Therefore, the phase diagram of Fig. 4.12 shows the free energy lines of the structures containing zero, one

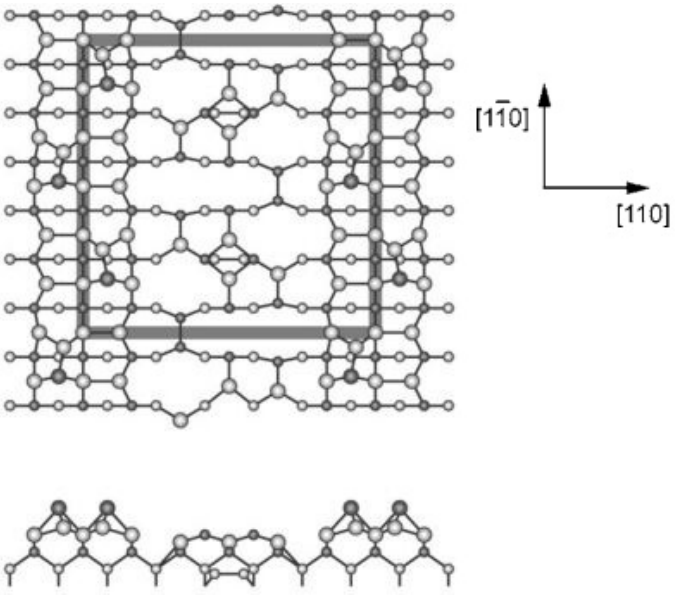

Figure 4.10: Atomic configuration corresponding to the Kocan model for the (6×6) structure. Empty circles correspond to Ga atoms, while filled circles correspond to As atoms. The top panel shows a bird's eye view of the surface. Bigger circles correspond to atoms that are higher up in the crystal lattice (i.e., closer to the reader). The square represents a (6×6) unit cell. The bottom panel shows a profile of the surface, cutting through the $[1\bar{1}0]$ direction. Reprinted from Ref. [1].

or both As-As dimers. As can be seen, the (12×6) structure (corresponding to one missing As-As dimer out of every four) has the lowest free energy compared to the the rest of (6×6) structures. However, this structure is still not stable for any value of μ_{Ga}. It has therefore been speculated that the (6×6) phase is metastable [125], especially since it has never previously been seen under As flux [1].

Our results, however, provide compelling evidence that the (6×6) phase is indeed stable, and not just metastable. Typically, a metastable phase will only show up when sweeping μ_{Ga} in one direction. However, the (6×6) phase is observed both in diffraction and real space during the droplet trail experiments in Fig. 4.5 when As is turned on and off. Indeed we see the same sequence of phases at a given location, including (6×6), whether μ_{Ga} is increasing or decreasing with time.

Figure 4.8 suggests that at high μ_{Ga} (6×6) transforms to $c(8 \times 2)$ via a region of phase coexistence between (6×6) and $c(8 \times 2)$ [6]. At lower Ga chemical potential (6×6) transforms to a (3×6) phase (Fig. 4.8). This (3×6) phase is stable over a relatively large range of μ_{Ga} and yet has not received wide attention in the literature. In particular, no detailed model has been proposed for this structure. Instead, a wide

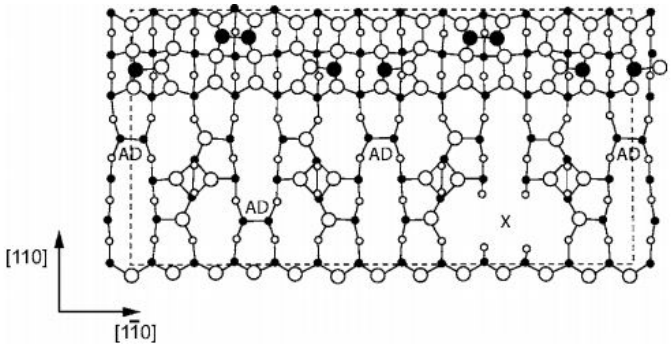

Figure 4.11: Atomic configuration corresponding to a unit cell of the (12×6) variant of the Kocan model. Empty circles correspond to Ga atoms, while filled circles correspond to As atoms. Bigger circles correspond to atoms that are higher up in the crystal lattice (i.e., closer to the reader). The As-As dimers within the troughs are denoted by 'AD', whilst the missing As-As dimer is represented by an 'X'. As can be seen, 1 out of 4 As-As dimers are missing. This presents the lowest free energy model for the (6×6) structure conceived to date. Reprinted from Ref. [10].

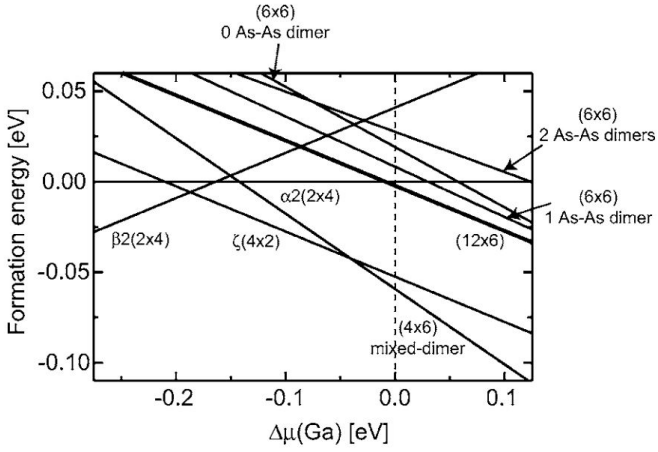

Figure 4.12: Phase diagram of GaAs(001) containing the formation energy lines for different variants of the Kocan model for the (6×6) structure. Reprinted from Ref. [10].

variety of reconstructions based around $(n\times6)$ periodicities have been discussed (see, for example, [1, 69, 73]). One possibility is that the many phases reported may not have attained equilibrium which is based around a (3×6) periodicity as displayed in Fig. 4.8. It is likely that other phase variants have similar free energies as a function of μ_{Ga} which may explain the wide ranging observations in the literature. At lower μ_{Ga}, it can be seen that the (3×6) phase converts to the well-known $\beta2(2\times4)$ structure (Fig. 4.8).

The radial sequence of phases observed in the DEPP (Fig. 4.3 and 4.8) directly reveals the sequence of phases occurring as a function of μ_{Ga}. With this information, we can superimpose these phases on DFT phase diagrams via Eq. (4.4). Consider first the (3×6) phase. Since no (4×6) or $\beta2(2\times4)$ structures exist on the high μ_{Ga} side, its free energy line must intersect $c(8\times2)$ somewhere between A and B in Fig. 4.13(b). We choose a reasonable point to illustrate, and label it D. Similarly, at lower μ_{Ga}, the phase transforms to $\beta2(2\times4)$ with no $c(4\times4)\beta$ or $c(8\times2)$ phases visible. The (3×6) free energy line must therefore intersect $\beta2(2\times4)$ somewhere between B and C. We label this point E. It is therefore possible to approximately superimpose the (3×6) free energy line on the phase diagram (Fig. 4.13(b)) as shown. Similarly, the (6×6) phase lies in between $c(8\times2)$ and (3×6). It must therefore intersect with (3×6) between points D and E, and cross $c(8\times2)$ between points A and D, allowing us to approximately add the (6×6) free energy line to the DFT calculation as shown in Fig. 4.13(b).

Finally, it is important to directly address the apparent discrepancy between our results and published calculations of surface energy in Figs. 4.9 and 4.12. Figures 4.13(a) and 4.6(b) show a sequence of phases $\beta2(2\times4)\rightarrow(3\times6)\rightarrow(6\times6)\rightarrow c(8\times2)$ with increasing μ_{Ga}, while theoretical calculations show $\beta2(2\times4)\rightarrow c(8\times2)$ [1, 2]. As previously discussed, variants of the (6×6) structure have been investigated in detail using DFT [1, 10]. However, all structures considered to date have a higher energy than $\beta2(2\times4)$ or $c(8\times2)$ for all μ_{Ga}. Of course, the calculations are based on DFT at $T=0\,\mathrm{K}$, while the experiments are at temperatures $\sim550\,^{\circ}\mathrm{C}$. Therefore it is natural to consider whether entropy could stabilize the (6×6) phase [10]. As

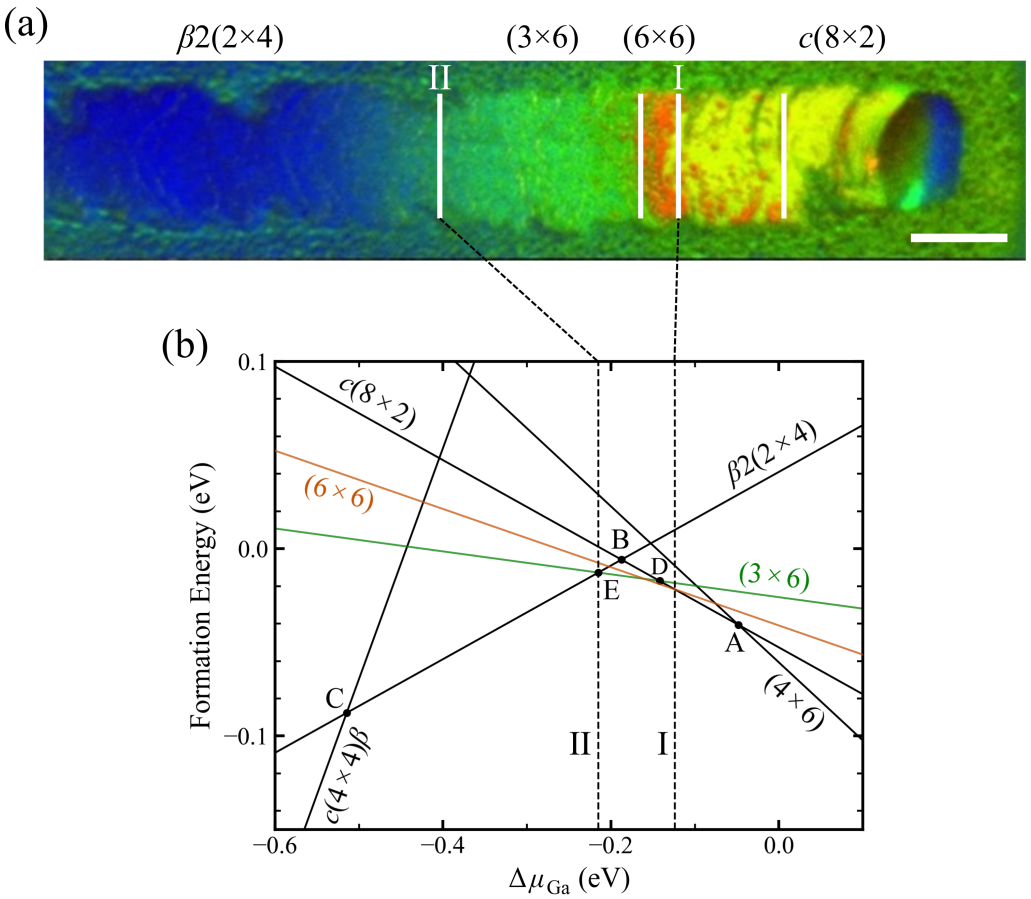

Figure 4.13: (a) The same image as that of Fig. 4.8 (b) Existing DFT calculation of the GaAs (001) phase diagram (black lines) [1, 2], plotting formation energy with respect to the $\alpha 2(2 \times 4)$ surface per (1×1) unit cell against relative Ga chemical potential $\Delta\mu_{\mathrm{Ga}}$ with respect to Ga bulk at 0 K. From the image in panel (a) we can schematically superimpose the formation energy lines of the (3×6) and (6×6) phases as shown, to suggest a surface phase diagram at 530 °C. The dashed vertical lines are the chemical potential values defining boundaries I and II. The scale bar in (a) is 2 μm.

mentioned previously, the most favorable (6×6)-like structure calculated at $T = 0\,\mathrm{K}$ is (12×6) [10]. However, the proposed structure (Fig.4.11) has the same slope (composition) as $c(8 \times 2)$ and so cannot be the final answer. In particular, Fig. 4.13 constrains the slope of (6×6) to be less Ga-rich than the proposed (12×6) so that it can intersect $c(8 \times 2)$ and (3×6) appropriately. Note, however, that some of the dimers upon the crests along the $[1\bar{1}0]$ direction of the (12×6) structure are As-As dimers, and not Ga-As dimers as those of the standard Kocan model of Fig. 4.10. Therefore, As-richer versions of the (12×6) structure of Fig. 4.11 can be constructed by replacing Ga-As dimers by As-As dimers. In fact, there is experimental evidence of there being (6×6) structures with different stoichiometries. In Ref. [76], Ohtake defines a low-temperature and a high-temperature version of the (6×6) strucuture. In the latter, there is an estimated $78\% \pm 11\%$ of Ga-As dimers upon the crests (the rest being As-As dimers). In the former, however, there is only an estimated $13\% \pm 8\%$ of Ga-As dimers. Therefore, relatively As-rich versions of the (12×6) structure of Fig. 4.11 can be conceived. In fact, the superimposed (6×6) free energy line in the phase diagram of Fig. 4.13(b) has been given the slope corresponding to the (12×6) structure of Fig. 4.11 with only 10% of Ga-As dimers, and has been lowered roughly 50 meV/(1×1) cell with respect the (12×6) line of Fig. 4.12 to render it stable. The combination of Ga-As and As-As dimers upon the crests of the structure, as well as the missing As-As dimers within the troughs provide configurational entropy [1, 10]. With $kT \sim 70\,\mathrm{meV}$, it seems reasonable to envisage that such structural elements could contribute sufficient configurational entropy to stabilize (6×6).

4.4 Conclusion

In summary, we have combined LEEM imaging and μLEED techniques to map surface phases around liquid Ga droplets during droplet epitaxy. This can be used to approximately map the GaAs(001) phase diagram and is highly complementary to existing DFT calculations. The method reflects phase stability at finite temperature and so naturally incorporates the influence of entropy. We envisage DEPPs will be

used to map surface free energy for a wide range of technologically important III-V materials, including nitrides.

Chapter 5

Dynamics of Local Droplet Etching

5.1 Introduction

Local Droplet Etching (LDE) emerged in the mid 2000s as a variant of the general droplet epitaxy technique that produces nanoholes in the place of the droplets [42, 48, 128]. It consists of high-temperature annealing of group III droplets ($T \sim 500 \rightarrow 600°C$ for the case of Ga) on III-As surfaces under a low As pressure in MBE reactors. The main application of LDE is to produce nanohole templates for filling with lattice-matched and hence strain-free quantum dots [49, 50, 118].

Since the early 1990s, the state-of-the-art method of production of quantum dots has been the Stranski-Krastanov method [129]. In this technique, the formation of quantum dots occurs during heteroepitaxial growth of one material on another which produces a lattice mismatch. In III-Vs, the classic example is growing InAs on GaAs(001), followed by subsequent capping with GaAs. During deposition, InAs begins growing in an epitaxial fashion and forming what is known as the wetting layer. However, the lattice mismatch between the GaAs and InAs systems makes the InAs layer accumulate strain. This continues until a critical thickness is achieved, and strain relaxation converts the 2-dimensional layer into 3-dimensional islands (quantum dots) accross the surface.

The Stranski-Krastanov method to produce quantum dots been highly success-

ful, and has thus been used widely throughout the years [130–132]. It does, however, have a number of drawbacks. Most importantly, the nature of the Stranski-Krastanov method requires the substrate material and the wetting layer material to be lattice-mismatched. This limits the possibilities of material combinations for quantum dot formation. Secondly, the residual strain induces an associated piezoelectric fields within the quantum dots. Thirdly, the strain that forms within the wetting layer will tend to produce misfit dislocations in the quantum dots formed. Lastly, the unavoidable intermixing of the wetting layer material with the underlying substrate, as well as with the capping layer.

The advent of LDE has enabled the community to address some of the limitations of the Stranski-Krastanov method. The basic procedure for GaAs quantum dot formation using LDE is the following: Firstly, a ∼500 nm $Al_xGa_{(1-x)}As$ (with $x \sim 0.3$) buffer layer is grown on GaAs(001). Next, Ga or Al droplets are formed on the surface by opening the Ga or Al shutter and depositing Ga or Al on the surface. The droplets form as per the Volmer-Weber growth mode [52]. The temperature at which this deposition is performed determines the density of droplets [133]. Concretely, the density of droplets decreases with increasing temperatures. For the case of Ga droplets, one can get a density of nanodroplets of around $100\mu m^{-2}$ depositing at $T = 150°C$. However, depositing Ga at the same flux and during the same amount of time (and hence depositing the same Ga coverage) but at a temperature of $T = 250°C$ yields a density of nanodroplets of just $\sim 1\mu m^{-2}$ [133]. This enables the experimentalist to select the density of droplets, and hence the density of quantum dots. Furthermore, the size of the droplets can be tuned by selecting a deposition time, i.e., a longer deposition time would produce larger droplets. This is a clear advantage over the Stranski-Krastanov method, as in the latter it is more difficult to control the density and size of dots. After the formation of droplets, metal deposition is shut down, and the substrate temperature is tuned to etching temperatures. In contrast to quantum dot or quantum ring formation, LDE is typically carried out at relatively high temperatures in the $T \approx 550°C \rightarrow 600°C$ regime. The sample is annealed at this temperature for a length of time of seconds/minutes usually with

the As shutter closed. This is because, for nanohole drilling, low As fluxes are needed, and the background As vapor in a standard MBE reactor is usually more than sufficient. After the droplets have been completely crystallised and an array of nanoholes is left on the surface, these are filled with GaAs. The final step is to grow another AlGaAs layer on top in order to produce the quantum well within the GaAs dot. Note that such GaAs dots are strain-free, and would not have been able to be grown as per the Stranki-Krastanov method given this is a lattice-matched system.

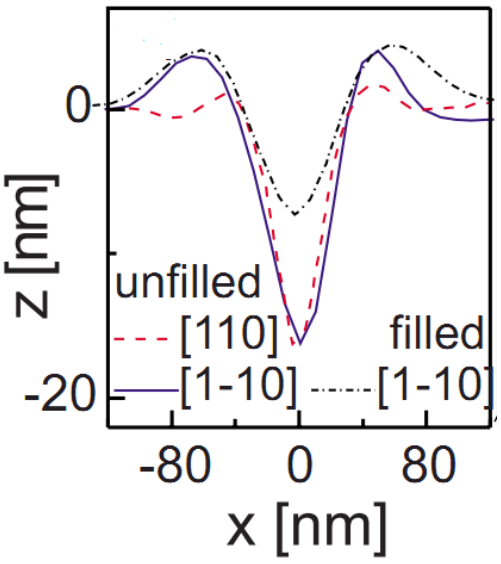

Figure 5.1: AFM linescans of a nanohole on AlGaAs both before (red, purple) and after (black) being filled with the GaAs dot. Reprinted from Ref. [11].

Therefore the mechanism LDE has been studied experimentally extensively throughout the years using different group III metals such as such as Ga, In or Al and on different III-V surfaces [9, 12, 42–47]. Also kinetic models of the mechanism of etching have been developed that address the phenomenology of nanohole formation in a precise manner [134, 135]. However, the mechanisms of mass transport during etching are not yet completely understood [47], and there still remain open questions such as the origin of the ring immediately outside the hole (see Fig. 5.1) or the necessity of a finite flux for drilling to occur [12]. Here we present a simple model for the case of Ga droplet etching of GaAs. It is based on the thermodynamic and kinetic concepts presented in Chapter 2. As we will see, the simulations that we produce are able to explain the formation of nanoholes from a purely physical

standpoint, and addresses the remaining open questions.

5.2 Theoretical Formalism

In this section the basic elements of the theory that underpin the simulations are presented. In our model we consider an array of identical Ga droplets on GaAs(001), distributed uniformly across the surface, with n nanoscale droplets per unit surface area. The surface is then annealed at high temperature ($T \sim 600^{\circ}$C) under an As flux. Mass transport between the vacuum, the solid, the adatom population and the droplet are considered, and the evolution of the surface is integrated. We consider the surface under and in the vicinity of one such droplet, and describe it mathematically as a surface of revolution about the axis of the droplet, i.e., by a function $h(r)$ which gives the height of the surface as a function of radial coordinate r. We assume a small-slope approximation in which $\mathrm{d}h/\mathrm{d}r \approx 0$ at all times, and so r represents 'distance along the surface'. Also, in line with the small slope approximation, the surface is displaced only in the vertical direction as the simulation proceeds. The rates of these processes determine the evolution of the system and the final morphology of the structure formed. The final surface geometries are then compared with experimental results.

5.2.1 Vapor-Solid growth; Ga and As adatoms

We begin by considering mass exchange between the adatom population and the solid during the droplet etching experiments. For this, we must calculate the Ga and As concentrations, C_{Ga} and C_{As} across the surface between the droplets. Knowing these we can then calculate the local growth velocity using Eq. (2.37) (Chapter 2) and integrate the evolution of the surface. Let us therefore first consider the steady-state adatom densities on the surface subjected to a certain As flux F_{As}.

Let us consider first the As density. In order to evaluate its magnitude, we turn to the continuity equation derived in Chapter 2 (Eq. (2.41)) for the case of As and

consider its steady-state version, i.e., that with $\partial C_{\mathrm{As}}/\partial t = 0$. This is

$$D_{\mathrm{As}}\nabla^2 C_{\mathrm{As}} - k_r\left[C_{\mathrm{Ga}}C_{\mathrm{As}} - (C_{\mathrm{Ga}}C_{\mathrm{As}})_{eq}\right] - \frac{C_{\mathrm{As}}}{\tau^d_{\mathrm{As}}} + F_{\mathrm{As}} = 0, \tag{5.1}$$

where D_{As} is the diffusion coefficient of As adatoms on the surface, τ^d_{As} is their lifetime before desorption, and F_{As} is the As flux being deposited on the surface. However, in the high temperature regime ($\approx 600°\mathrm{C}$) associated with local droplet etching (LDE) arsenic evaporates readily, so that its diffusion length on the surface can be considered negligible. Therefore we neglect the diffusion term in the continuity equation and write simply

$$-k_r\left[C_{\mathrm{Ga}}C_{\mathrm{As}} - (C_{\mathrm{Ga}}C_{\mathrm{As}})_{eq}\right] - \frac{C_{\mathrm{As}}}{\tau^d_{\mathrm{As}}} + F_{\mathrm{As}} = 0. \tag{5.2}$$

Now, making the further assumption that Ga migrates very rapidly across the surface and hence that C_{Ga} is uniform (to be evaluated shortly), we may solve Eq. (5.2) for C_{As} to obtain

$$C_{\mathrm{As}} = \frac{F_b + F_{\mathrm{As}}}{k_r C_{\mathrm{Ga}} + \left(\tau^d_{\mathrm{As}}\right)^{-1}} \tag{5.3}$$

where $F_b \equiv k_r(C_{\mathrm{Ga}}C_{\mathrm{As}})_{eq}$ is the segregation flux from the bulk solid. Note that C_{As} is not in general homogeneous, since $(C_{\mathrm{Ga}}C_{\mathrm{As}})_{eq}$ depends on position through the crystal chemical potential μ_{GaAs}, As per Eq. (2.12) in Chapter 2. Decomposing μ_{GaAs} into $\mu_{\mathrm{GaAs}} = g_{\mathrm{GaAs}} + \Delta\mu_{\mathrm{GaAs}}$, i.e., a bulk component plus a position-dependent surface excess, and assuming a small $\Delta\mu_{\mathrm{GaAs}}/kT$ we have may write

$$(C_{\mathrm{Ga}}C_{\mathrm{As}})_{eq} \approx (C_{\mathrm{Ga}}C_{\mathrm{As}})^{\infty}_{eq}\left(1 + \frac{\Delta\mu_{\mathrm{GaAs}}(r)}{kT}\right), \tag{5.4}$$

where $(C_{\mathrm{Ga}}C_{\mathrm{As}})^{\infty}_{eq}$ is the $(C_{\mathrm{Ga}}C_{\mathrm{As}})_{eq}$ for $\Delta\mu_{\mathrm{GaAs}} = 0$. Introducing this in Eq. (5.3) gives

$$C_{\mathrm{As}}(r) = \frac{F^{\infty}_b\left(1 + \Delta\mu_{\mathrm{GaAs}}(r)/kT\right) + F_{\mathrm{As}}}{k_r C_{\mathrm{Ga}} + \left(\tau^d_{\mathrm{As}}\right)^{-1}}, \tag{5.5}$$

where F^{∞}_b is the segregation flux from the solid for $\Delta\mu_{\mathrm{GaAs}} = 0$. Eq. (5.5) shows explicitly how the As adatom concentration will be higher at points where the surface chemical potential $\Delta\mu_{\mathrm{GaAs}}$ is higher and thus where the decomposition of the solid

is faster.

Let us turn now to the Ga adatom density. Given Ga diffuses readily at these temperatures, we consider a global form of its steady-state mass balance equation, i.e., one that states that the rate of Ga influx to the whole surface equals the rate of Ga outflux. Such as equation writes

$$-k_r\left[C_{\mathrm{Ga}}\overline{C_{\mathrm{As}}}-\overline{(C_{\mathrm{Ga}}C_{\mathrm{As}})}_{eq}\right]-\frac{C_{\mathrm{Ga}}}{\tau_{\mathrm{Ga}}^{d}}+2\pi r_D n k_D(C_{\mathrm{Ga}}^{l}-C_{\mathrm{Ga}})=0. \tag{5.6}$$

Here $\overline{C_{\mathrm{As}}}$ denotes spatial average of $C_{\mathrm{As}}(r)$, i.e. $\overline{C_{\mathrm{As}}}\equiv 1/A_{tot}\int C_{\mathrm{As}}(r)dA$ (likewise for $\overline{(C_{\mathrm{Ga}}C_{\mathrm{As}})}_{eq}$), where dA is an area element of the surface and A_{tot} is the total area of the surface. The first term of Eq. (5.6) relates to Ga exchange between the adatom population and the solid, the second is the rate of Ga evaporation (τ_{Ga}^{d} is Ga adatom lifetime before desorption), and the third is the net rate of Ga supply of the droplet array to the surface. Let us recall from Chapter 2 (Eq. 2.44) that $k_D(C_{\mathrm{Ga}}^{l}-C_{\mathrm{Ga}})$ is the net rate of Ga detachment from the droplet to the adatom population per unit contact line length. Therefore, the net rate of Ga supply per unit surface area from the droplet array to the adatom population is $2\pi r_D n k_D(C_{\mathrm{Ga}}^{l}-C_{\mathrm{Ga}})$, where $2\pi r_D$ is the instantaneous contact line perimeter length of the droplets (r_D is their radius), and we recall n is the number of droplets per unit surface area. We neglect the rate of shrinkage of the droplets, compared to the fast atomistic processes at these temperatures. In order to solve Eq. (5.6) for the Ga concentration C_{Ga}, we define the Ga lifetime before attachment to a droplet, $\left(\tau_{\mathrm{Ga}}^{D}\right)^{-1}\equiv 2\pi r_D n k_D$, and a total Ga lifetime as $\tau_{\mathrm{Ga}}^{-1}=\left(\tau_{\mathrm{Ga}}^{d}\right)^{-1}+\left(\tau_{\mathrm{Ga}}^{D}\right)^{-1}$. We further approximate the spatially-averaged terms of Eq. (5.6) by their value for $\Delta\mu_{\mathrm{GaAs}}=0$ (i.e. we change the overline by a ∞ superscript) since this will only stop holding in the immediate vicinity of droplets and thus over a small fraction of the total area of the surface. Introducing also Ga flux $F_{\mathrm{Ga}}=C_{\mathrm{Ga}}^{l}/\tau_{\mathrm{Ga}}^{D}$, we may put Eq. (5.6) in a more compact form to solve, which is

$$-k_r C_{\mathrm{Ga}}C_{\mathrm{As}}^{\infty}-\frac{C_{\mathrm{Ga}}}{\tau_{\mathrm{Ga}}}+F_b^{\infty}+F_{\mathrm{Ga}}=0, \tag{5.7}$$

with influxes and outfluxes written explicitly. Although Eq. (5.7) looks linear in

C_{Ga} and trivial to solve, we ought to note that the As density C_{As}^{∞} depends upon C_{Ga} (see Eq. (5.3)) through

$$C_{\mathrm{As}}^{\infty} = \frac{F_b^{\infty} + F_{\mathrm{As}}}{k_r C_{\mathrm{Ga}} + \left(\tau_{\mathrm{As}}^d\right)^{-1}}. \tag{5.8}$$

Therefore substituting Eq. (5.8) into Eq. (5.7) gives quadratic equation

$$k_r \tau_{\mathrm{As}}^d C_{\mathrm{Ga}}^2 + \left[\left(F_{\mathrm{As}} - F_{\mathrm{Ga}}\right) k_r \tau_{\mathrm{Ga}} \tau_{\mathrm{As}}^d + 1\right] C_{\mathrm{Ga}} - \tau_{\mathrm{Ga}} \left(F_b^{\infty} + F_{\mathrm{Ga}}\right) = 0, \tag{5.9}$$

whose solution is

$$C_{\mathrm{Ga}} = \frac{\left(F_{\mathrm{Ga}} - F_{\mathrm{As}}\right) k_r \tau_{\mathrm{Ga}} \tau_{\mathrm{As}}^d - 1 + \sqrt{\left[\left(F_{\mathrm{Ga}} - F_{\mathrm{As}}\right) k_r \tau_{\mathrm{Ga}} \tau_{\mathrm{As}}^d - 1\right]^2 + 4 k_r \tau_{\mathrm{Ga}} \tau_{\mathrm{As}}^d \left(F_b^{\infty} + F_{\mathrm{Ga}}\right)}}{2 k_r \tau_{As}^d}. \tag{5.10}$$

Note that C_{Ga} depends on the density of droplets n and on the instantaneous radius r_D (through τ_{Ga}), and will thus change throughout the course of the experiment. However, it is not obvious at first sight how C_{Ga} will evolve throughout the experiment until the simulations are run.

Knowing the Ga and As surface concentrations we can compute the locally-defined growth velocity outside of the droplet as

$$v_O = \Omega_{\mathrm{GaAs}} k_r \left[C_{\mathrm{Ga}} C_{\mathrm{As}} - \left(C_{\mathrm{Ga}} C_{\mathrm{As}}\right)_{eq}\right], \tag{5.11}$$

where Ω_{GaAs} is the volume of a primitive cell in GaAs, C_{Ga} is given by Eq. (5.10), C_{As} is given by Eq. (5.5), and $\left(C_{\mathrm{Ga}} C_{\mathrm{As}}\right)_{eq}$ is given by Eq. (5.4). Integrating Eq. (5.11) in time yields the evolution of the surface outside of the droplets, as a after a time interval of $\mathrm{d}t$ the surface will be displaced an amount $\mathrm{d}h_O = v_O \mathrm{d}t$.

5.2.2 Liquid-solid growth

Now we consider mass exchange between the liquid and the solid. As explained in Chapter 2, the growth reaction at the liquid-solid interface under the droplet again $\mathrm{Ga_{(l)}} + \mathrm{As_{(l)}} \leftrightarrow \mathrm{GaAs}_{(s)}$, where the sparsely dissolved atoms of As in the droplet

react with Ga (the solvent) to form GaAs at the liquid-solid interface. As the arsenic solubility in liquid Ga is very low (below 0.2% at 600°C), the rate of reaction to form GaAs at the liquid-solid interface will be approximately proportional to the arsenic mole fraction x_{As} given the low As solubility in GaAs. We will assume x_{As} remains homogeneous throughout the droplet at all times, as diffusion in the liquid is fast [136]. Therefore, recalling the expression for the net growth rate at the liquid-solid interface from Chapter 2 (Eq. (2.38)), we can write the net growth velocity under the droplet as

$$v_I = \Omega_{\mathrm{GaAs}} k_l (x_{\mathrm{As}} - x_{\mathrm{As}}^{eq}), \tag{5.12}$$

where x_{As}^{eq} is the locally-defined As mole fraction in equilibrium with the solid, and relates to the crystal chemical potential μ_{GaAs} exponentially, as given by Eq. (2.23) (Chapter 2). Given that μ_{GaAs} separates into a bulk component plus a surface component, i.e., $\mu_{\mathrm{GaAs}} = g_{\mathrm{GaAs}} + \Delta\mu_{\mathrm{GaAs}}$, and assuming the surface component remains small, that is, $\Delta\mu_{\mathrm{GaAs}}/kT << 1$ we may write the x_{As}^{eq} in Eq. (5.12) as

$$x_{\mathrm{As}}^{eq}(r) \approx x_{\mathrm{As}}^{eq,\infty} \left(1 + \frac{\Delta\mu_{\mathrm{GaAs}}(r)}{kT}\right), \tag{5.13}$$

where $x_{\mathrm{As}}^{eq,\infty}$ is the value of x_{As}^{eq} for $\Delta\mu_{\mathrm{GaAs}} = 0$.

Let us now consider the form of the surface chemical potential $\Delta\mu_{\mathrm{GaAs}}$. Assuming, for simplicity, that the solid has isotropic surface energy γ, and recalling Eq. (2.29) from Chapter 2 we may write

$$\Delta\mu_{\mathrm{GaAs}} = \Omega_{\mathrm{GaAs}}(\gamma\kappa + p), \tag{5.14}$$

where κ is the curvature of the surface and p is the pressure applied to the surface. Surface energy γ will be the liquid-solid energy γ_{ls} for the surface under the droplet. However Eq. (5.14) also applies to the surface outside of the droplet. In this case we would have that γ equals the vacuum-solid surface energy γ_{vs}. Furthermore, pressure p will be zero under the droplet (we neglect the capillary pressure in the droplet) and also outside the droplet, as the surface is exposed to the vacuum. Therefore p will only be nonzero at the droplet contact line, where it should express the pulling

of the droplet on the surface due to the droplet surface tension γ_{vl}. The question now is how to treat the discontinuity introduced by the contact line.

5.2.3 Smearing the contact line

In order to address the discontinuity, we note that a realistic droplet contact line at these temperatures ought to be subject to thermal fluctuations. Therefore it makes physical sense to smooth the contact line over some finite width w. We will now illustrate how this is done for the case of the surface energy γ.

The surface free energy γ maybe written as [62]

$$\gamma(r) = \Theta(r)\gamma_{vs} + (1 - \Theta(r))\gamma_{ls}, \tag{5.15}$$

where $\Theta(r)$ is a step function, taking a value of 0 under the droplet and 1 outside the droplet. In the absence of smoothing $\Theta(r)$ would be the Heaviside step function centered at the contact line position. However, we smooth the step function over a width w by setting

$$\Theta(r) = \frac{1}{2}\mathrm{erfc}\left(\frac{r_D - r}{\sqrt{2}w}\right), \tag{5.16}$$

where erfc is the complementary error function.

Analogously, the (negative) pressure exerted onto the surface of the solid at the contact line position due to the droplet surface tension pulling on the solid is given by [62]

$$p(r) = -\gamma_{vl} \sin\theta_c \, \delta_c(r), \tag{5.17}$$

where $\delta_c(r)$ is a Delta function centered at the contact line. However, we smooth this Delta function by taking it as the derivative of our smoothed step function defined in Eq. (5.16), that is

$$\delta_c(r) = \frac{\mathrm{d}\Theta(r)}{\mathrm{d}r} = \frac{1}{\sqrt{2\pi}w}\exp\left(-\frac{(r_D - r)^2}{2w^2}\right), \tag{5.18}$$

which gives a Gaussian of width w centered at the contact line. Numerically we take this width as $w = 1\mathrm{nm}$.

The surface chemical potential of Eq. (5.14) is then

$$\Delta\mu_{\mathrm{GaAs}}(r) = \Omega_{\mathrm{GaAs}}(\gamma(r)\kappa(r) + p(r)), \tag{5.19}$$

where $\gamma(r)$ is given by Eq. (5.15) and $p(r)$ is given by Eq. (5.17). The curvature of the surface is the sum of its radial component and its angular component, that is

$$\kappa = -\frac{h''}{(1+h'^2)^{3/2}} - \frac{h'}{r\,(1+h'^2)^{1/2}}, \tag{5.20}$$

where $' = \mathrm{d}/\mathrm{d}r$. However, in our small-slope approximation we can set $h' = \mathrm{d}h/\mathrm{d}r \approx 0$. This sets the angular curvature equal to zero and simplifies the total curvature to

$$\kappa \approx -h'', \tag{5.21}$$

5.2.4 Evolution of the system; Integrating the LDE problem

Let us now explain how the evolution of the system is integrated. We begin with a flat surface at temperature $T \approx 580\,^{\circ}\mathrm{C}$ subjected to a certain flux F_{As}, on which there sits a droplet array with n identical, evenly distributed droplets per unit area, each containing N_{Ga} Ga atoms and N_{As} As atoms. For simplicity we set these such that the arsenic mole fraction is that of equilibrium with the bulk solid, i.e., $x_{\mathrm{As}} = x_{\mathrm{As}}^{eq,\infty}$. Note that N_{Ga} and N_{As} determine the volume V of the droplet, as

$$V = \Omega_{\mathrm{Ga}}^{l} N_{\mathrm{Ga}} + \Omega_{\mathrm{As}}^{l} N_{\mathrm{As}}, \tag{5.22}$$

where Ω_{Ga}^{l} and Ω_{As}^{l} are the respective volumes of Ga and As in the liquid. In turn V determines the position r_D of the contact line, as we will make θ_c remain at its equilibrium value at all times, given by

$$\cos\theta_c = \frac{\gamma_{vs} - \gamma_{ls}}{\gamma_{vl}}. \tag{5.23}$$

Concretely, the volume of a spherical cap with contact angle θ_c is $V = \beta(\theta_c) r_D^3$, where $\beta(\theta_c)$ is a geometrical constant for a spherical cap of contact angle θ [137].

These quantities determine the growth velocity of the solid both outside the droplets ($v_O(r)$) and under them ($v_I(r)$). We define the total growth velocity field by smoothing $v_O(r)$ and $v_I(r)$ across the contact line, i.e.

$$v(r) = \Theta(r)v_O(r) + (1 - \Theta(r))v_I(r). \tag{5.24}$$

Knowing the growth velocity map at the initial instant, we find the displacement of the surface after a small time interval δt simply by as

$$\delta h(r) = v(r)\delta t \tag{5.25}$$

During this small time interval δt the droplets have exchanged Ga and As with their surroundings. We therefore need to calculate the changes δN_{Ga} and δN_{As} in the Ga and As atoms making up the droplet and, with those, find the As mole fraction x_{As} and contact line position r_D in order to continue tracking the evolution of the surface.

Neglecting Ga desorption from the surface of the droplets, we note that Ga can exit/enter the droplet via growth/decomposition at the liquid-solid interface or via detachment/attachment at the droplet contact line. Therefore, the rate of change of the number of Ga atoms N_{Ga} making up the droplet is

$$\frac{\mathrm{d}N_{\mathrm{Ga}}}{\mathrm{d}t} = -\int \frac{v_I}{\Omega_{\mathrm{GaAs}}}(1 - \Theta(r))\,\mathrm{d}A - 2\,\pi\,r_D\,k_D\left(C^l_{\mathrm{Ga}} - C_{\mathrm{Ga}}\right). \tag{5.26}$$

where $\mathrm{d}A$ is the area element of the solid surface. For the case of As, we note that it can likewise exit/enter the droplet via growth/decomposition at the liquid-solid interface. Furthermore, As can enter the droplet due to the As flux F_{As} landing on the surface of the droplet, but it can also exit the droplet by desorbing from its surface. Therefore, the rate of change of the number of As atoms N_{As} making up the droplet is

$$\frac{\mathrm{d}N_{\mathrm{As}}}{\mathrm{d}t} = -\int \frac{v_I}{\Omega_{\mathrm{GaAs}}}(1 - \Theta(r))\,\mathrm{d}A + 4\,\pi\,r_D^2\,\alpha(\theta_c)\left(\xi F_{\mathrm{As}} - F^l_{\mathrm{As}}\right), \tag{5.27}$$

where $4\,\pi\,r_D^2\,\alpha(\theta_c)$ is the area of a spherical cap of radius r_D and contact angle θ_c, and ξ is the sticking coefficient of the incoming As on the droplet surface.

Knowing the new atoms numbers $N_{\mathrm{Ga}} + \delta N_{\mathrm{Ga}}$ and $N_{\mathrm{As}} + \delta N_{\mathrm{As}}$ after a time interval δt using Eqs. (5.26) and (5.27) enables us to calculate the new As mole fraction $x_{\mathrm{As}} + \delta x_{\mathrm{As}}$ as well as the new contact line position $r_D + \delta r_D$. The system is tracked in time by iterating this process until the droplet is consumed.

5.3 Results

In this section we will present simulation results of local droplet etching containing the theoretical scheme described above. In particular, we will consider the same droplet etching experiment under three different As flux intensities. We consider a GaAs(001) surface at $T = 600°\mathrm{C}$ on which there sits a droplet array of identical Ga droplets with droplet radii of $r_D = 0.1\mu\mathrm{m}$, distributed on the surface with density $n = 0.5\mu\mathrm{m}^{-2}$. These can be considered to be distributed forming a hexagonal 2D lattice with a side of length $a = \sqrt{2/(\sqrt{3}n)} \approx 1.5\mu\mathrm{m}$. We also set the initial As mole fraction in the droplet as that of equilibrium with the bulk solid at chemical potential $\mu_{\mathrm{GaAs}} = g_{\mathrm{GaAs}}$, i.e., $x_{\mathrm{As}} = x_{\mathrm{As}}^{eq,\infty}$, which at these temperatures equals $\sim 0.18\%$. We will integrate the evolution of one droplet out of the array and compare the results considering the different flux intensities. It may seem intuitive that a completely minimized flux is best for etching, as one seeks to have a Ga droplet as undersaturated of As as possible for drilling. However we will see that a small but finite flux is optimal for drilling within experimentally accessible timescales. This conclusion has already been reached in experiment [12], but with no physical model to explain why. Here we will address this issue within the physics of our model presented above.

5.3.1 Drilling under low (optimal) As flux

Firstly, we consider a relatively low flux in our simulations; we set a representative value of $F_{\mathrm{As}} = 10^5\mu\mathrm{m}^{-2}\mathrm{s}^{-1}$ and integrate the evolution of the system as described in Section 5.2.4. We also set the rate constant associated to desorption from the droplet

surface such that the net flux penetrating the droplet equals the evaporating flux exiting the droplet, i.e., $k_{\mathrm{As}} x_{\mathrm{As}}^{eq,\infty} = \xi F_{\mathrm{As}}$ (we set a sticking coefficient of $\xi = 0.7$). At first sight, under these circumstances there would seem to be no reason for drilling at the liquid-solid interface. However, it must be noted that although $\mu_{\mathrm{GaAs}} = g_{\mathrm{GaAs}}$ holds under the the bulk droplet, close to the contact line we must consider the pulling of the droplet surface and so $\mu_{\mathrm{GaAs}} = g_{\mathrm{GaAs}} + \Omega_{\mathrm{GaAs}} p$ (see Eq. (5.14)). This is shown schematically in Fig. (5.2), which shows the initial flat surface (blue) on which there sits the initial droplet (red), together with the crystal chemical potential profile μ_{GaAs} (green). As can be seen, μ_{GaAs} remains constant throughout out the flat surface except under the contact line where it dips in a pronounced manner due to the pulling exerted by the droplet's surface tension. This dip produces a noticeable disequilibrium between the droplet and the solid, i.e., $x_{\mathrm{As}} > x_{\mathrm{As}^{eq}}$ (also between the adatom population and the solid, i.e., $C_{\mathrm{Ga}} C_{\mathrm{As}} > (C_{\mathrm{Ga}} C_{\mathrm{As}})_{eq}$) and triggers GaAs deposition at the contact line position.

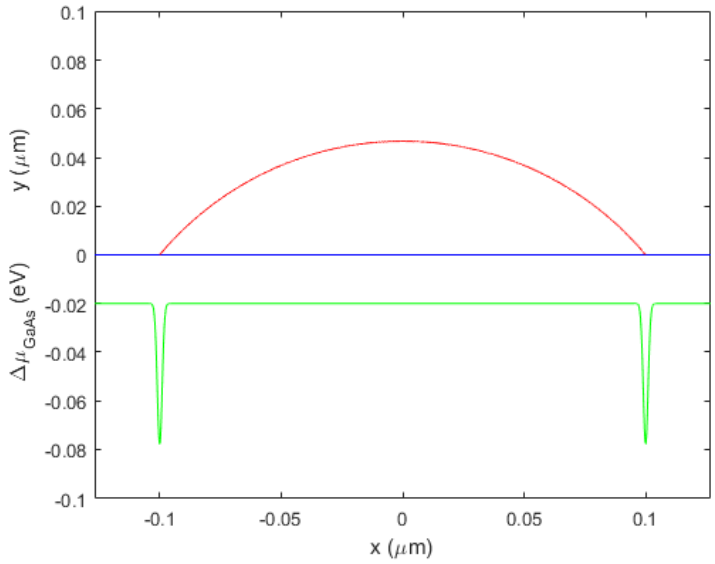

Figure 5.2: Initial configuration: a Ga droplet (red) sitting on a flat GaAs surface (blue). The green line represents the crystal chemical potential μ_{GaAs}. As can be observed, it is constant everywhere except under the contact, where is dips due to the droplet's surface tension pulling on the solid. We take a width $w = 1\,\mathrm{nm}$ as the Gaussian width for the contact line.

Figure 5.3 shows the evolution of the surface. The blue solid line represents the profile of the surface, the vertical dotted lines represent the position of the contact line, and the green dotted horizontal line represents the initial flat geometry of the

surface. Panel (a) shows the initially flat surface. Panel (b) shows the surface after 100 s and, as is well observed, the dip in μ_{GaAs} under the contact line gives rise to a GaAs ridge at the contact line position.

Given that the small As content in the droplet, x_{As} falls when the reaction Ga + As $\rightarrow$ GaAs takes place, so that the droplet becomes undersaturated in As (i.e., $x_{\mathrm{As}} < x_{\mathrm{As}}^{eq,\infty}$) when deposition occurs. This, in turn, triggers drilling under the bulk droplet (note the surface under the droplet goes below the dashed green line). This encapsulates the mechanism of etching: the droplet surface tension pulling on the solid induces GaAs deposition at the contact line. GaAs deposition undersaturates the Ga droplet of As and gives rise to drilling under the bulk droplet.

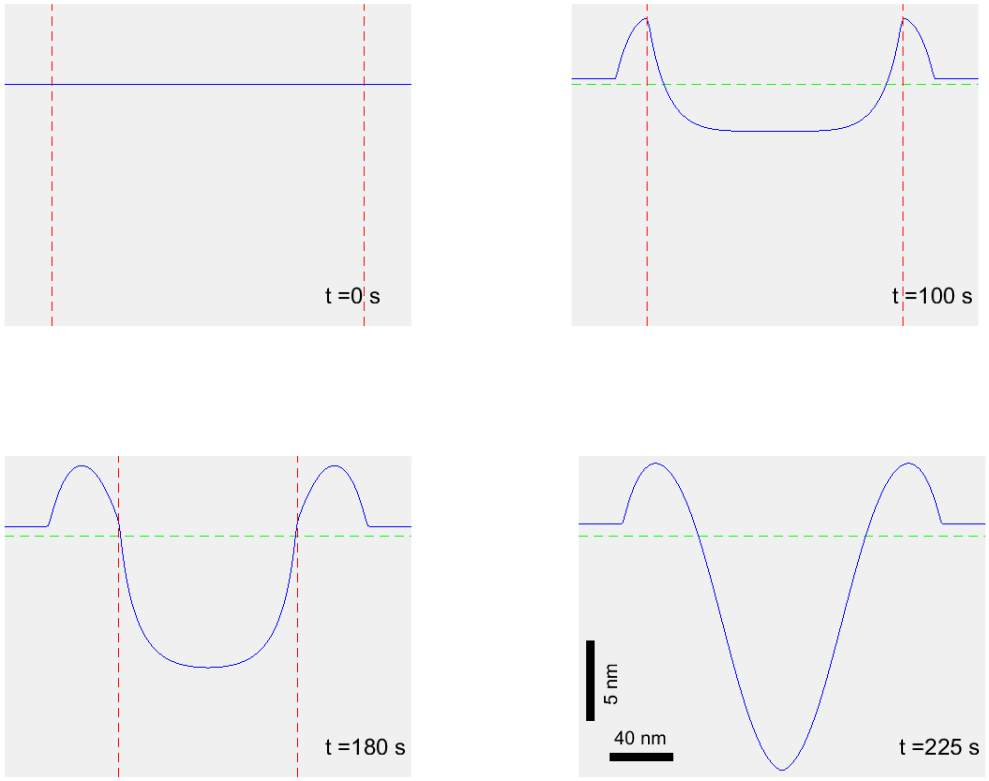

Figure 5.3: Profiles of the evolving surface (blue) under and in the vicinity of a Ga nanodroplet beloning to a nano-droplet array, subjected to an arsenic flux of $F_{\mathrm{As}} = 10^5 \mu\mathrm{m}^{-2}\mathrm{s}^{-1}$. The dashed horizontal green line is the initial surface, and the two vertical red lines represent the instantaneous position of the droplet contact line.

Let us now consider what is happening to the adatom population, and how this affects the evolution of the droplet. In the absence of As flux, the Ga adatom con-

centration would be close to its value of equilibrium with the droplets, C^l_{Ga}, as the temperature is close to the maximum temperature for congruent evaporation T_c. We take C^l_{Ga} to be 0.25 (in units of the number of sites per unit area for a Ga adatom to sit). However, the incoming As flux reacts with surface Ga, thereby lowering the Ga adatom concentration C_{Ga}. This enhances the net Ga flux per unit contact line length from the droplet to the adatom population $J_{\mathrm{Ga}} = k_D \left(C^l_{\mathrm{Ga}} - C_{\mathrm{Ga}}\right)$. The droplets begin losing Ga to the adatom population and therefore shrinks as the experiment proceeds. Effectively, the Ga from the droplets is being crystallized across the surface. Note how the surface outside of the droplet grows as the experiment proceeds (see Fig. 5.3). The final height of the surface (≈ 0.75nm) approximately corresponds to the Ga stored in the initial droplet array (the difference lying in the small amount of Ga that has evaporated).

Figure. 5.4(centre) furthermore shows a plot of the Ga adatom concentration C_{Ga} versus t. Initially, when the droplets are still large, the Ga supply to the surface is relatively abundant. As can be seen in Fig. 5.4(centre), the initial C_{Ga} is close to $C^l_{\mathrm{Ga}} = 0.25\,\nu_{\mathrm{Ga}}$, indicating that the droplet array is replenishing the surface with Ga at a high rate in spite of the presence of the As flux. The value of C_{Ga} continues more or less constant (though decreasing gently) until the droplets reaches approximately half of its initial size. From that point on C_{Ga} decreases rapidly. This is because the droplets are substantially smaller, and therefore the total droplet contact line length per unit surface area that supplies Ga is diminished. C_{Ga} eventually falls to its value in the absence of droplets. Fig. 5.4(left) shows a plot of the contact line position $r_D(t)$ versus t. As can be seen, $r_D(t)$ decreases at approximately a uniform rate until it is about half its initial value. From that point on, the droplet shrinks faster and faster as it continues to shed Ga to the surface while its contact-line-to-volume ratio increases.

It is also useful to consider how the As mole fraction in the droplet changes throughout the course of the experiment. Fig. 5.4(right) shows the plot of $x_{\mathrm{As}}(t)$ versus t. Interestingly, the evolution of x_{As} is unlike the evolution of r_D and C_{Ga}. It stays very much constant and close to the value of equilibrium with the solid, $x^{eq,\infty}_{\mathrm{As}}$

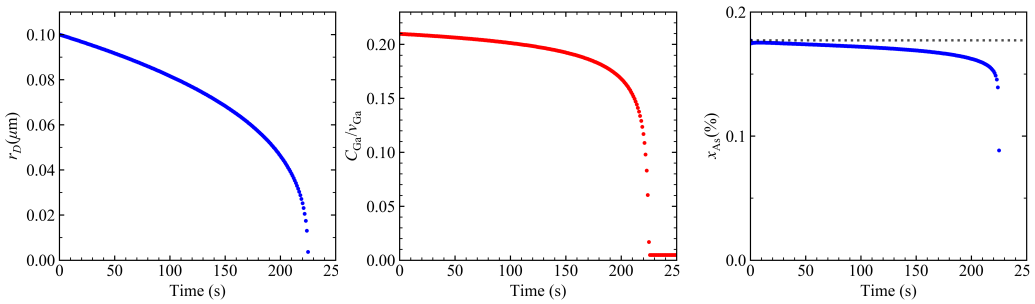

Figure 5.4: Here we show the evolution in time the droplet contact line position (left), the Ga adatom concentration C_{Ga} in units of ν_{Ga} (middle), and the As mole fraction x_{As} in the droplet (right). The black dotted line represents the As mole fraction of equilibrium with the bulk solid, $x_{\mathrm{As}}^{eq,\infty}$.

until the very end of the etching experiment when the droplet is very small. This reflects another very important characteristic of the system: the high rate at which the growth and decomposition reactions Ga + As $\leftrightarrow$ GaAs occur at the liquid-solid interface at the elevated temperatures of LDE ($T \sim 600°$C), i.e., the high value of the reaction rate constant k_l in Eq. (5.12). The large k_l enables the rapid growth of the GaAs ridges at the contact line. In turn, it enables the rapid restoration of the diminished x_{As} (due to the growth at the contact line) by drilling into the solid at a fast rate, and hence for the process to be repeated again. The large rate constant k_l for growth/decomposition at the liquid-solid interface is thus one of the fundamental ingredients behind the formation of nanoholes during LDE experiments.

5.3.2 Drilling under a minimized As flux

Let us now consider the same droplet etching experiment, only now under a completely minimised As flux. This does not mean zero As flux, as there is always a background pressure in MBE chambers associated to residual As from previous experiments. In practice a minimal As flux can be achieved by cooling the As cell. We set an As flux ten times less intense, i.e., $F_{\mathrm{As}} = 10^4 \mu\mathrm{m}^{-2}\mathrm{s}^{-1}$ and we track the evolution of a droplet during 225 s. This is purposely the same amount of time that was needed to crystallise the droplet completely in the previous experiment when using $F_{\mathrm{As}} = 10^5 \mu\mathrm{m}^{-2}\mathrm{s}^{-1}$.

At first thought, it would seem that etching would be favoured under a minimised As flux, since a lower flux would imply a droplet more undersaturated of As and

therefore drilling faster into the solid. This, however, is not the case, as is shown Fig. 5.5, which shows the simulated evolution of the surface profile under these conditions. As in the previous case, the droplets have an initial radius of $r_D = 0.1\,\mu$m and contain the equilibrium As mole fraction $x_{\mathrm{As}} = x_{\mathrm{As}}^{eq,\infty}$. However, the dip in the crystal chemical potential μ_{GaAs} at the contact line position drives GaAs growth to form the classic ridge under the contact line. As explained before, GaAs deposition results in a decrease of the As mole fraction x_{As} in droplet, and thus triggers drilling of the solid under the bulk droplet. This restores the x_{As} in the droplet and enables the process to be repeated again. However, after 225 s of annealing, we only have $\sim$ 4nm deep holes as opposed to the $\sim$ 15nm deep holes that were obtained when annealing under the ten times larger As flux of $F_{\mathrm{As}} = 10^5 \mu\mathrm{m}^{-2}\mathrm{s}^{-1}$. It is also noticeable that the droplet has only shrunk minimally (see Fig. 5.6(left) for a plot of contact line position r_D versus annealing time t) and it is therefore logical to ask whether this has any link to the shallow holes.

In order to find the link between the minimised As flux, the slow droplet shrinkage, and the shallow drilling let us first analyze the behaviour of the adatom population. Under this low As flux, the rate of Ga reaction with surface As is low. Therefore the Ga adatom concentration C_{Ga} is barely affected and remains close to its value C_{Ga}^l of equilibrium with the droplets, as can be seen in Fig. 5.6(middle). As a result of this, the net flux per unit contact line length of Ga from the droplet to the adatom population $J_{\mathrm{Ga}} = k_D \left(C_{\mathrm{Ga}}^l - C_{\mathrm{Ga}}\right)$ remains low, and hence the shrinking of the droplet remains slow. Effectively, the incoming low As flux is crystallizing the droplet array at a slow rate. The shallow drilling under the droplet is in fact a consequence of the idleness of the contact line position r_D. As GaAs is deposited at the contact line, the curvature of the surface at that point builds and hence the crystal chemical potential grows (see Eq. (5.14)). If the contact line does not move, GaAs will continue to be deposited at the same point of the surface and the surface curvature will continue to grow at the same point. This will continue until $\gamma\kappa$ effectively cancels the droplet pulling (negative) pressure p in Eq. (5.14), i.e. $\gamma\kappa + p \approx 0$, and equilibrium is reached between the droplet and the solid. At

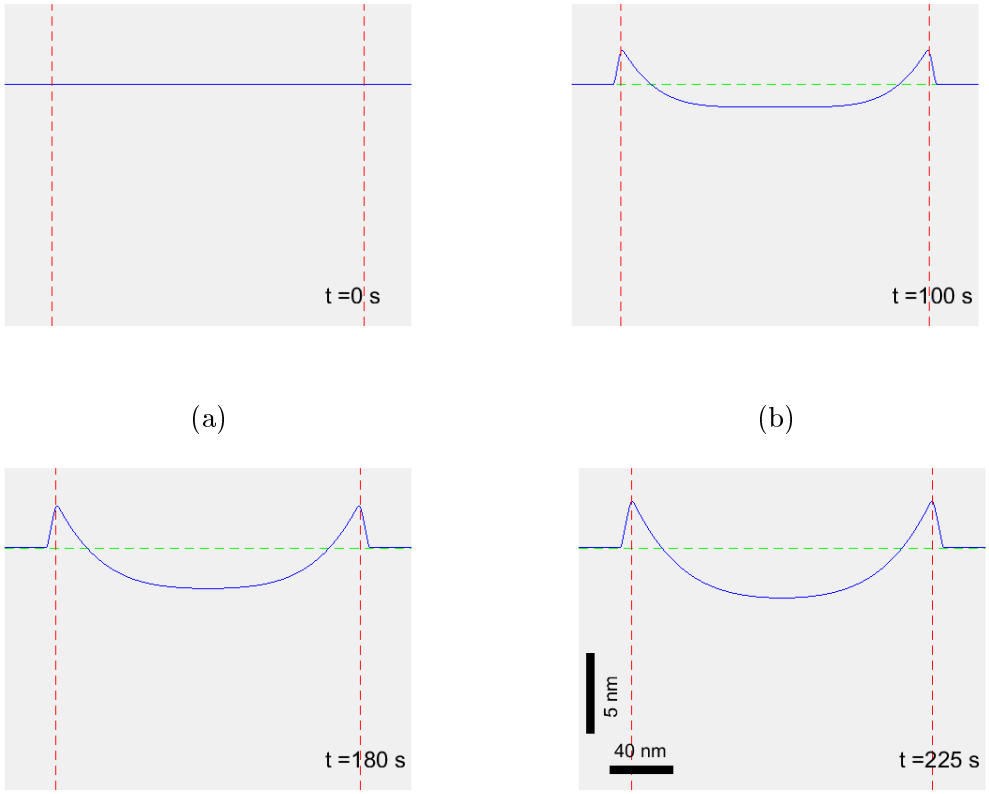

Figure 5.5: Profiles of the evolving surface (blue) under and in the vicinity of a Ga nanodroplet beloning to a nano-droplet array, subjected to a minimised arsenic flux of $F_{\mathrm{As}} = 10^4 \mu\mathrm{m}^{-2}\mathrm{s}^{-1}$ during 225 s (the amount of time that was needed for the droplets to crystallise completely when using $F_{\mathrm{As}} = 10^5 \mu\mathrm{m}^{-2}\mathrm{s}^{-1}$). The dashed horizontal green line is the initial surface, and the two vertical red lines represent the instantaneous position of the droplet contact line.

this point GaAs deposition at the contact line stops and hence the drilling under the bulk droplet stagnates. In the previous case with higher flux, as the contact line moved it continued to encounter un-curved surface on which to deposit GaAs and hence give continuity to the drilling of the solid. The necessity of a finite As flux for drilling has already been observed experimentally [12], but the reason for this was not well understood. Our model, however, resolves this dilemma elegantly in physical terms.

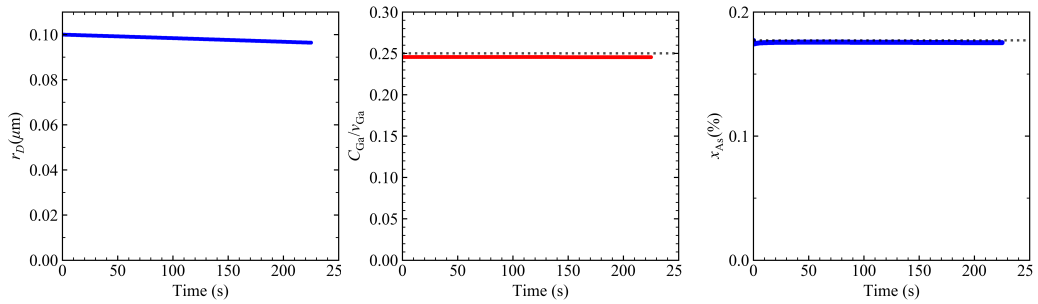

Figure 5.6: Here we show the evolution in time of the droplet contact line position (left), the Ga adatom concentration C_{Ga} in units of ν_{Ga} (middle), and the As mole fraction x_{As} in the droplet (right) for the case of $F_{\mathrm{As}} = 1 \times 10^4 \mu\mathrm{m}^{-2}\mathrm{s}^{-1}$. The black dotted line in the (center) panel corresponds to the liquidus Ga concentration C^l_{Ga} and the black dotted line in panel (right) represents the As mole fraction of equilibrium with the bulk solid, $x^{eq,\infty}_{\mathrm{As}}$.

5.3.3 Drilling under high As flux

Lastly, let us now consider the case of high As flux, and set $F_{\mathrm{As}} = 5 \times 10^5 \mu\mathrm{m}^{-2}\mathrm{s}^{-1}$ (all the rest of parameters are held the same).

Figure 5.7 shows the simulated evolution of the surface profile when the surface is irradiated with the high flux. As can be see, the droplet contact line moves a lot faster (vertical dashed red line) than in the previous cases; the whole droplet is crystallized in 69 s seconds (compared to the 225 s when the optimal $F_{\mathrm{As}} = 1 \times 10^5 \mu\mathrm{m}^{-2}\mathrm{s}^{-1}$ was used). This can be also noted in Fig. 5.8(left), that shows the droplet contact line position r_D versus time t.

The shorter timescale for crystallization of the droplet is a consequence of the higher As flux, which crystallizes Ga at a higher rate. This is clearly manifested in Fig. 5.8(centre), which shows the evolution of the adatom Ga concentration C_{Ga} with time. The higher As flux F_{As} gives and increased As adatom population C_{As} and hence increases the rate of reaction with Ga to form GaAs. This increased rate of reaction notably diminishes the Ga concentration C_{Ga} on the surface. Meanwhile the droplet replenishes the surface with Ga at a rate $J_D = k_D \left(C^l_{\mathrm{Ga}} - C_{\mathrm{Ga}}\right)$per unit contact line length. Given the low surface Ga concentration C_{Ga}, it does so at high rate, making the droplets disappear in a much shorter time (note in Fig. 5.8(centre) how low C_{Ga} is in relation to C^l_{Ga}).

The other result that is very much noticeable in the simulation results of Fig. 5.7 is the shallow depth of the resulting nanoholes, which barely reach $\sim$ 4nm below

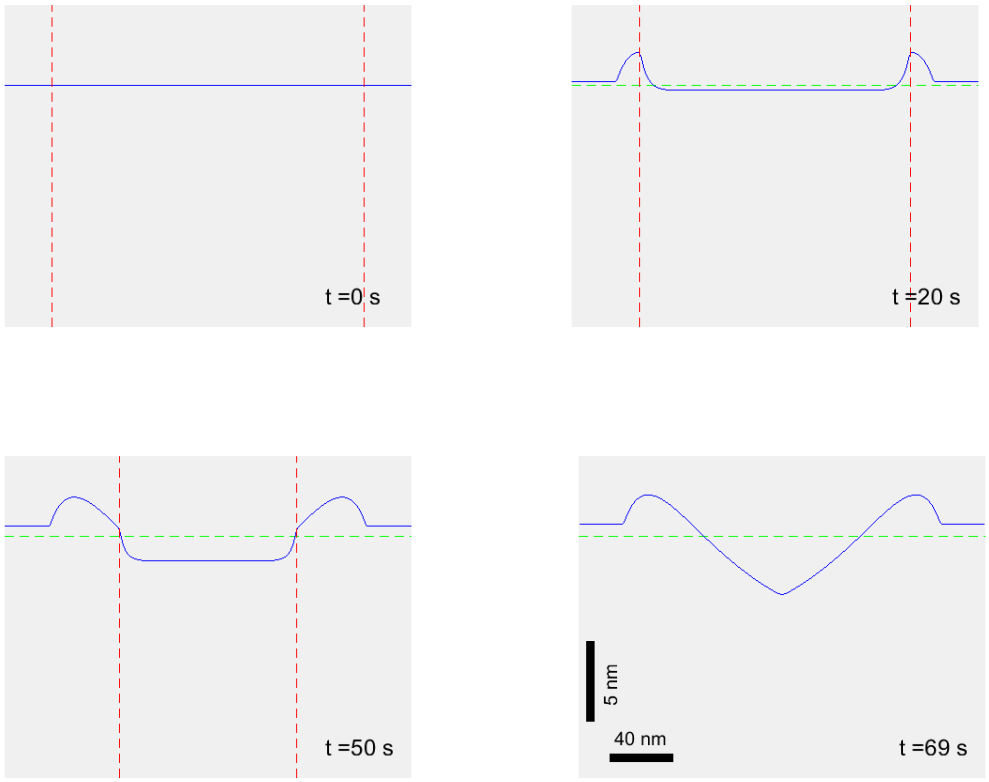

Figure 5.7: Profiles of the evolving surface (blue) under and in the vicinity of a Ga nanodroplet belonging of a nanodroplet array, subjected to a minimized arsenic flux of $F_{\mathrm{As}} = 10^4 \mu\mathrm{m}^{-2}\mathrm{s}^{-1}$. The dashed horizontal green line is the initial surface, and the two vertical red lines represent the instantaneous position of the droplet contact line.

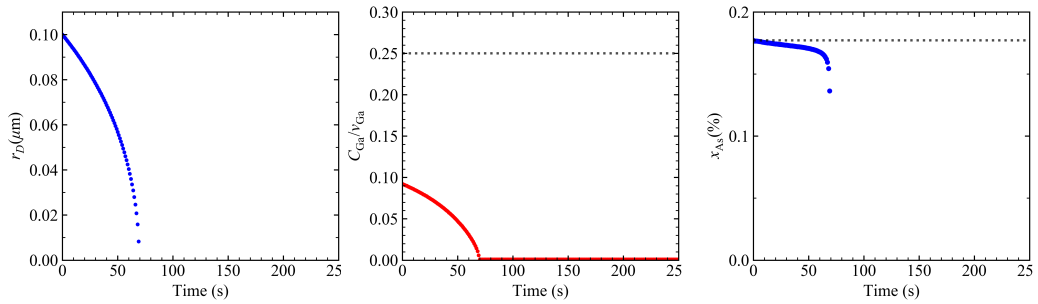

Figure 5.8: Here we show the evolution in time of the droplet contact line position (left), the Ga adatom concentration C_{Ga} in units of ν_{Ga} (middle), and the As mole fraction x_{As} in the droplet (right) for the case of $F_{\mathrm{As}} = 5 \times 10^5 \mu\mathrm{m}^{-2}\mathrm{s}^{-1}$. The black dotted line in the (center) panel corresponds to the liquidus Ga concentration C^l_{Ga} and the black dotted line in panel (right) represents the As mole fraction of equilibrium with the bulk solid, $x^{eq,\infty}_{\mathrm{As}}$.

the surface. It is hence logical to ask how the higher As flux and hence the shorter timescale of the experiment may have given rise to this. The key is actually in the higher velocity with which the droplet contact line moves along the surface as the droplet shrinks (see Fig.5.8(left)). As the contact line sweeps through a certain point on the surface, it does not have time to deposit as much GaAs at that point as it did for lower fluxes. This milder deposition results in a less deteriorated As mole fraction x_{As} in the droplet, and hence less drilling into the solid. For high fluxes the main mechanism is thus the crystallization of the droplets across the surface. The fast rate at which this happens gives less time for the droplets to drill into the solid.

As a minor point, note again that the As mole fraction stays very close to its value for equilibrium with the bulk solid, i.e., $x_{\mathrm{As}} = x^{eq,\infty}_{\mathrm{As}}$, throughout the whole experiment (see Fig. 5.8(right)). This, again, is due to the high rate of the growth and decomposition reaction at the liquid solid interface, so that a loss of As in the droplet due to deposition is quickly replenished by drilling under the bulk droplet. Only at the very end of the experiment, when the droplet is very small, does x_{As} drop as a consequence of the increased contact-line-perimeter-length-to-volume in small droplets.

5.3.4 Comparison with experiment

Lastly, we now compare the final morphology of the nanoholes under the different fluxes of our simulations with results found across the literature. In Fig. 5.9 we show

the final morphologies of the simulated nanohole drilling for the minimized As flux (panel (a)), low flux (panel (b)), and high flux (panel (c)). In Fig. 5.10 we show Atomic Force Microscopy (AFM) linescans of nanoholes produced under minimised flux (panel (a)) [12], low flux (panel (b)) [9], and high flux (panel (c)) [9]. The minimised flux is attained by closing the As shutter and cooling the As cell [12]. Under these conditions the droplets are not crystallised, so they were removed using HCl before AFM scanning. The low and high flux cases (panels (b) and (c)) were performed in the same MBE chamber [9] at a sample temperature of $T = 520°\mathrm{C}$. The only difference between the two cases was the As flux. In the low flux case the chamber pressure was 10^{-7}Torr, while in the high flux case the pressure was 3×10^{-6}Torr.

As can be observed, the overall agreement with experiment is good. Probably the biggest discrepancy is found for minimised As flux case. In our simulations (Fig. 5.9(a)) the liquid-solid interface acquires a rounded shape. The slow advancement of the contact line gives time for this interface to attain some sort of equilibrium shape. This equilibrium configuration, given the assumed isotropic interface energy γ_{ls} is a uniformly curved surface (i.e. a spherical cap) together with a droplet slightly undersaturated with As, i.e. $x_{\mathrm{As}} < x_{\mathrm{As}}^{\infty}$ (see Fig. 5.6). However, the experimental profile for minimised flux (Fig. 5.10(a)) shows quite a flat liquid-solid interface aligned with the (001) direction. This is likely a manifestation of surface energy anisotropy favouring the low energy (001) surface versus vicinal directions.

The salient features of the low (optimal) flux cases (Fig. 5.9(b) and 5.10(b)) compare very favourably. Our simulations reproduce the ridges at the contact line position, as well as the V-tapered shape of the nanohole that is produced as the droplet shrinks. The ridges in the experimental image do look somewhat flatter than those produced in our simulation. This could be a consequence of the high temperature annealing at 620°C for 2 min that was performed after the etching 'in order to remove liquid residues' [9], as it is known that surfaces flatten out when annealing at high temperatures [46].

The high flux case (Fig. 5.9(c) and 5.10(c)) compare very well. The major feature

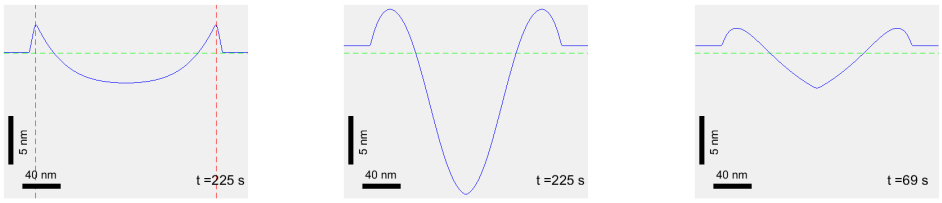

(a) (b) (c)

Figure 5.9: Final profiles of the nanoholes as per our simulations. Panel (a) shows the profile for minimised As flux $F_{\mathrm{As}} = 1 \times 10^4 \mu\mathrm{m}^{-2}\mathrm{s}^{-1}$. Panel (b) shows the profile for low (optimal) flux $F_{\mathrm{As}} = 1 \times 10^5 \mu\mathrm{m}^{-2}\mathrm{s}^{-1}$, and panel (c) shows the profile for high flux $F_{\mathrm{As}} = 5 \times 10^5 \mu\mathrm{m}^{-2}\mathrm{s}^{-1}$.

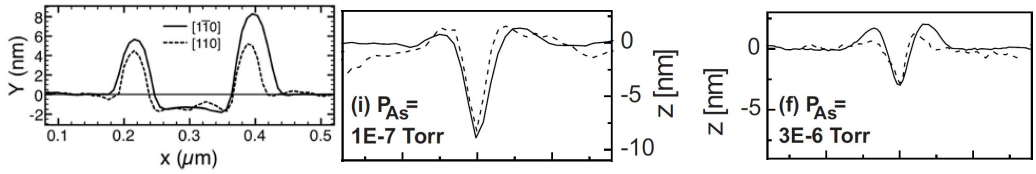

(a) (b) (c)

Figure 5.10: Experimental AFM linescans of nanohole morphologies under different conditions. Panel (a) shows the resulting morphology of a nanohole produced by annealing under at $T = 500°\mathrm{C}$ under a minimized As flux for 30 mins (reprinted form Ref. [12]). The uncrystallized Ga was removed using HCl. Panel (b) shows a nanohole resulting from annealing at $T = 520°\mathrm{C}$ and under a low As flux, corresponding to a pressure of 1×10^{-7}Torr (reprinted from Ref. [9]). Panel (c) shows a nanohole resulting from annealing at $T = 520°\mathrm{C}$ in the same MBE reactor as panel (b) but under a higher As pressure of 3×10^{-6}Torr (reprinted from Ref. [9]). The ticks in the horizontal axes of panels (b) and (c) correspond to 50 nm.

is the shallower holes produced after etching, which is cleary noticeable in both our theory and in experiment.

5.4 Conclusions

In conclusion, we have developed a model for LDE etching of Ga droplets on GaAs surfaces. Using kinetic concepts of mass transport between the droplet, the crystal, and the adatom population, it is able to explain the to-date poorly understood mechanism of droplet etching. In essence we find that etching is triggered by GaAs deposition at the contact line position, driven by the droplet's surface pulling on the solid. This induces drilling at liquid-solid interface under the bulk droplet in order to replenish the equilibrium As content in the droplet. All of this occurs while the incoming As flux crystallizes the droplet across the whole GaAs surface and

therefore while the droplets shrink in size. This shrinking is also shown to be a key ingredient in the drilling; a stationary contact line and hence a minimised flux results in limited drilling. Therefore a low flux is necessary for drilling, as a contact line in motion is needed in order for etching to occur continously. The concepts herein should apply to other III-As systems such Al etching of AlAs or In etching of InAs.

Chapter 6

Conclusions

In this thesis we have investigated essentially two aspects of the GaAs(001) surface; surface phase stability and Ga droplet etching. Regarding phase stability of the GaAs(001) surface we have combined advanced LEEM techniques and theoretical modelling to make two contributions to the state-of-the-art of GaAs(001) surface phases.

In our first study we observed a novel form of phase coexistence on GaAs(001). When this surface is heated above $T \sim 580°$C under vacuum, it is well known that the stable phase in this regime is the $c(8 \times 2)$ reconstruction. However, we observe metastable phase domains spontaneously appear and disappear as a consequence of the enhanced effects of Langmuir evaporation at these elevated temperatures. By means of our advanced dark-field techniques we identify these as corresponding to the (6×6) phase. This phenomenon gives rise to a dynamic phase coexistence which has previously gone unnoticed, possibly due to a lack of real-time imaging of this surface. To better understand the novel mechanism, a Monte Carlo model was developed that is governed by a simple set of rules consistent with our LEEM observations. At the lower temperatures (close to $T \sim 580°$C), we find evaporation is dominated by inverted wedding cake structures, i.e., evaporation occurs in multi-layer mode. This creates a significant time-averaged (6×6) coverage (around 9%). With increasing T, such structures become less pronounced as evaporation tends towards a layer-by-layer mode. This results in a decreased (6×6) coverage, which persists appreciably up to $T \sim 620°$C. Usually, for purposes of growth, just one surface phase is desired.

This novel phenomenon might therefore have broad technological relevance for the growth and processing of thin films under vacuum, since surface phase metastability is likely to occur across a wide range of materials.

In our second study, we combined droplet epitaxy with advanced LEEM imaging and μLEED techniques to map surface phases around liquid Ga droplets. To understand our observations we developed a simple model that considers the diffusion of Ga atoms from the droplets and their reaction with the incoming As flux. The computations produce Ga chemical potential gradients from the droplet edge that explain the sequential order of phases with distance to the droplet, as well as how these phases appear and disappear upon (respectively) opening and closing the As flux. Our observations confirm the stability of the controversial (6×6) phase across a narrow range of Ga chemical potential, and we also establish the existence of a novel (3×6) phase. The respective order of such phases with distance to the droplet allows us to incorporate them in an approximate manner to the GaAs(001) phase diagram. The method reflects phase stability at finite temperature and so naturally incorporates the influence of entropy. This technique is likely to be useful in mapping surface phases for a wide range of technologically important III-V materials, including nitrides.

In our last piece of work we have developed a model for etching of Ga droplets on GaAs surfaces. The model incorporates kinetic concepts of mass transport between the droplet, the crystal, and the adatom population, to explain the mechanism of droplet etching, which to date remains poorly understood. Importantly, we find that etching is a process that originates with the GaAs deposition that occurs at the contact line position, and is driven by the droplet's surface pulling on the solid. The consequent loss in As in the droplet induces drilling at liquid-solid interface under the bulk droplet in order to replenish the equilibrium As content. This deposition-drilling mechanism occurs while the incoming As flux crystallizes the droplet across the GaAs surface and therefore while the droplet shrinks in size. We find that this shrinking is key in the drilling process, as a stationary contact line and hence a minimised flux results in stagnated drilling once the ridge under the contact line

has grown sufficiently. We find that a low flux is necessary for drilling given that a contact line sweeping the GaAs surface is needed in order to achieve continuous deposition and hence drilling. Our model explains this fact, which had been previously observed experimentally, within a simple physical framework. It should be applicable to other III-As systems such Al etching of AlAs or In etching of InAs.

Appendix A

Determining probabilities J_b and ρ from LEEM movies

In this Appendix we will explain how we measure the $c(8\times 2)$ nucleation probability ρ per unit time and area of (6×6), as well as the probability J_b per unit time and area of Lochkeim formation on (6×6). These were measured at different sample temperatures T in the $580-640$°C range. Arrhenius fittings were then performed on these measurements, and the former were fed into the Monte Carlo simulation code as is explained in the main text.

Let ρ be the probability per unit area and time for nucleation of the stable phase on the metastable phase. If we have N metastable domains all with surface area A, after time $\mathrm{d}t$, the number of domains will have dropped by $\mathrm{d}N$, with

$$\mathrm{d}N = -\rho A N \mathrm{d}t. \tag{A.1}$$

Changing variables from from t to domain radius R, we have $\mathrm{d}t = \mathrm{d}R/v$, where v is the step velocity, and $A = \pi R^2$, giving

$$\mathrm{d}N = -\frac{\pi\rho}{v} N R^2 \mathrm{d}R. \tag{A.2}$$

Integrating Eq. (A.2) yields

$$N(R) = N_0 \exp\left(-\frac{\pi\rho}{3v}R^3\right), \tag{A.3}$$

where N_0 is the initial number of domains. Differentiating Eq. (A.3) yields

$$\mathrm{d}N = -N_0 \frac{\pi\rho}{v}R^2 \exp\left(-\frac{\pi\rho}{3v}R^3\right)\mathrm{d}R. \tag{A.4}$$

The probability distribution is hence

$$f(R) = 3\frac{R^2}{a^3}\exp\left(-\frac{R^3}{a^3}\right), \tag{A.5}$$

where a is

$$a = \left(\frac{3v}{\pi\rho}\right)^{1/3}, \tag{A.6}$$

and is related to the average domain radius upon phase transformation, $\langle R\rangle = \int_0^\infty Rf(R)\,\mathrm{d}R$, via $a = \langle R\rangle / \Gamma(4/3)$, where Γ is the gamma function.

To calculate ρ at a certain temperature, we first perform measurements on our LEEM videos and produce a histogram of (6×6) terrace radius at which $c(8\times2)$ nucleates, as contained in Fig. A.1(a). The value of ρ is then calculated by fitting the histogram to the distribution of Eq. (A.5), including an arbitrary proportionality constant. This yields a value for a, which is used together with the corresponding value of v to compute ρ from Eq. (A.6). Our histograms only include single (6×6) domains which undergo transformation to $c(8\times2)$ via the fundamental mechanism as in Fig. 1 of the main text.

A completely analogous argument applies to J_b, only that we consider Lochkeim nucleation instead of phase nucleation. The added difficulty is that it is not possible to observe the moment of Lochkeim nucleation, as $(6\times6)/(6\times6)$ steps show no contrast. Therefore we measure radii R_1 and R_2 of the upper and lower terraces, respectively, as soon as the upper terrace transforms to $c(8\times2)$ and the lower becomes visible (see Section II.A). In accordance with our assumption that step velocity v is independent of the nature of the phases on either side of the step, the

radius of the upper domain at the moment the lower domain nucleated is $R_1 - R_2$. Therefore to calculate J_b at a certain temperature, we perform measurements on our LEEM videos and produce a histogram of (6×6) terrace radius $R = R_1 - R_2$ at which a Lochkeim nucleates on it, as contained in Fig. A.1(b). We then fit the histogram to Eq. (A.5) (including an arbitrary proportionality constant) to obtain a value for a which is then used in Eq. (A.6) (with J_b in the place of ρ) to compute J_b.

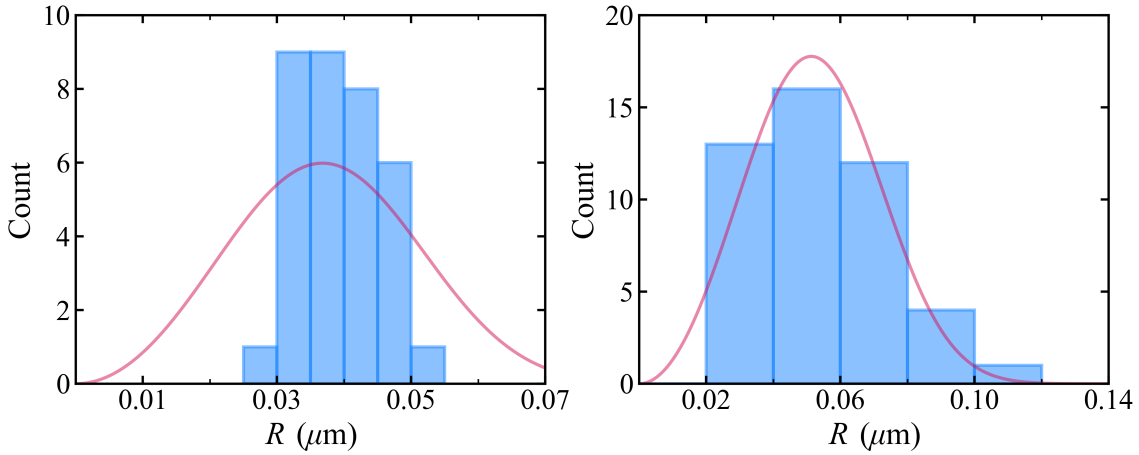

Figure A.1: Histograms of (6×6) terrace radius upon (a) $c(8 \times 2)$ nucleation ($T = 628\,^{\circ}\mathrm{C}$), and (b) Lochkeim nucleation ($T = 592\,^{\circ}\mathrm{C}$), together with their fit to the distribution of Eq. (A.5).

Appendix B

Methodology of the Monte Carlo simulations

In this appendix we proceed to describe the methodology on which the surface phase metastability Monte Carlo simulations are based.

As in most time-evolution simulations models, time is discretised, so that the state of the system is re-evaluated after finite-sized timesteps with magnitude δt. It is convenient to set as small a δt as possible in order to emulate the continuous nature of time as accurately as possible without overly compromising computation time.

In an analogous manner space ought also to be discretised in the form of a mesh. In the case of a 2-dimensional system like ours we represent the GaAs(001) surface by a square *surface matrix*, S. Each element of S represents a small square portion of the GaAs(001) surface with width δx. A given surface element will be either set to 0 or to 1, corresponding to (6×6) and $c(8 \times 2)$, respectively. As with the timestep, δx should be made as small as possible. For this reason surface meshes are usually large matrices. In addition, we need to consider a large GaAs(001) surface in order to obtain precise values for the time-averaged (6×6) coverage. Therefore we usually set S to be 1000×1000 while representing a $10\mu\text{m} \times 10\mu\text{m}$ surface, rendering $\delta x = 10\,\text{nm}$. When calculating the (6×6) coverage was not the focus, we considered smaller portions of GaAs(001) surface and could afford to put δx down to $\approx 1\,\text{nm}$ (as in Fig. 3.14).

The passage of time is modeled by a for loop in which each iteration the state of the surface is updated in correspondence with timestep δt. In our simulations, we utilise matrices that contain all of the information of what is occurring on our GaAs(001) surface. We use these to then produce surface matrix S. We will now explain in more detail how this is done.

The simulations begin with a pristine $c(8\times2)$ surface. Therefore we start with an $N \times N$ surface matrix S containing all 1's (let us suppose we set $N = 1000$). In our first for-loop iteration, i.e., after a time-step δt, the probability p that a Lochkeim nucleation has formed somewhere on the surface is $p = J_w A\,\delta t$, where J_w is the rate of Lochkeim formation per unit surface area and A is the area of our surface (typically $100\,\mu\text{m}^2$). Note that δt has to be made sufficiently small so that $p << 1$. In order to decide whether a Lochkeim has indeed formed on our surface we generate a random number ξ with $0 < \xi < 1$. If $\xi > p$ then no Lochkeime will have formed. However if it occurs that $\xi < p$ then a Lochkeim will have indeed formed somewhere across our surface. In order to decide the location of this Lochkeim, we produce new random numbers m and n which correspond to the coordinates of the Lochkeim in S. These will be real numbers within the $(0, N)$ range. Next we would store this information in a matrix M containing all the relevant information relating to the (6×6) patches on the surface. Concretely, each row of M relates to one patch, and contains the loop iteration i on which the given patch was formed, its coordinates m and n on S, as well as further information as we will see later. Note that we may label each (6×6) patch with the loop-iteration i on which it formed, as at most one Lochkeim will form per loop iteration. With each passing iteration, the radius of existing (6×6) patches will increase an amount $v\,\delta t$, thereby growing in surface area and being subject to $c(8 \times 2)$ nucleation within them. They can also coalesce with each other, or coalesce with a terrace that has already converted to $c(8 \times 2)$. Let us consider now how a generic loop iteration is handled within our MC simulation model.

Figure B.1 shows a schematic flow diagram of the main computational tasks carried out within a generic for-loop iteration. As can be seen, these can be divided

into four main consecutive sections. We will now explain in detail what exactly is done within each of these.

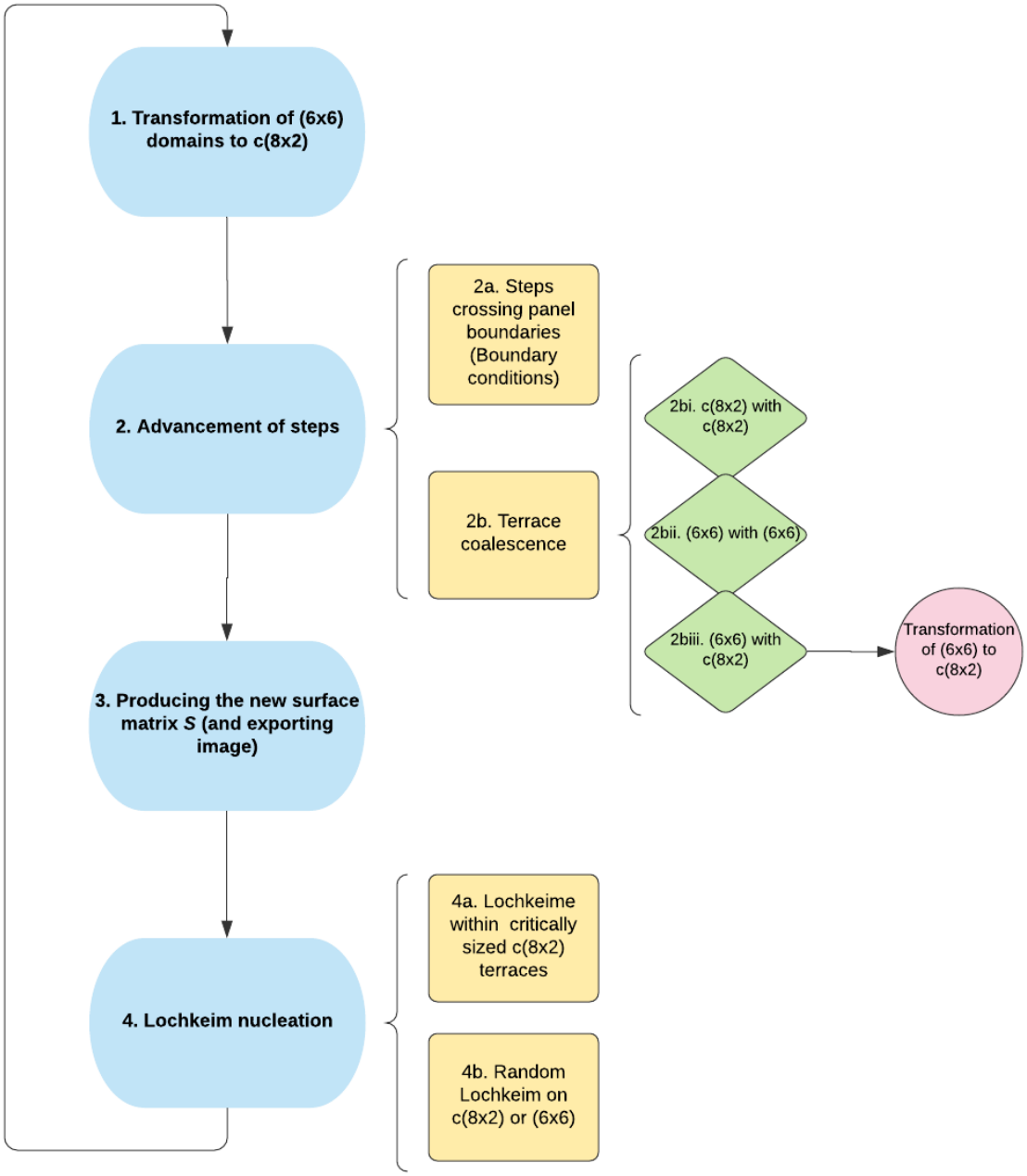

Figure B.1: Schematic flow diagram of the sequential computational tasks performed in a given for-loop iteration.

1. **Transformation of** (6×6) **terraces to** $c(8 \times 2)$**.** First of all, we span all of our black (6×6) patches and see whether $c(8 \times 2)$ will nucleate within them on this iteration. As we observe fast phase boundary propagation experimentally (see Fig. 3.4), in our model we assume $c(8 \times 2)$ propagates instantly across the entire (6×6) once it has nucleated. Therefore we do not consider the motion

of the $c(8 \times 2)$ phase boundary, but rather we assume the whole (6×6) terrace converts to $c(8 \times 2)$ at once.

The probability p of $c(8 \times 2)$ nucleation on a (6×6) terrace on this iteration is $p = \rho\, A_{(6\times6)}\, \delta t$, where ρ is the rate of $c(8 \times 2)$ nucleation on (6×6) (measured experimentally as explained in Appendix A), and $A_{(6\times6)}$ is the area of the (6×6) terrace. To decide whether the (6×6) terrace will convert to $c(8 \times 2)$ we generate a random number ξ with $0 < \xi < 1$. If $\xi > p$, $c(8 \times 2)$ nucleation will not occur. Conversely, if $\xi < p$ then the (6×6) patch ought to transform to $c(8 \times 2)$. We register this occurrence by eliminating the corresponding row (or rows, if the given (6×6) terrace is the coalescence of various (6×6) terraces. We will see how we treat this later) in M. We transfer this matrix row to another information matrix W, analogous to M but containing the information of the $c(8 \times 2)$ terraces present of the surface.

2. **Advancement of steps.** After having decided what (6×6) terraces phase-transform, we ought to consider the advancement of steps during the timestep δt. The expansion of terraces due to step advancement has two main consequences that have to be considered (see Fig. B.1).

   - First is that a step may outgrow our finite-sized GaAs(001) surface. The way to make a finite surface as infinite as possible is to apply periodic boundary conditions. This means assuming that our finite GaAs(001) surface is actually the 'unit cell' of an infinitely large GaAs(001) surface, and that what occurs on our finite surface is occurring identically in the rest of unit cells making up the infinite GaAs(001) surface. This means that if a step crosses our surface through one of its sides, it ought to appear again through the opposite side. Likewise, if a step crosses a corner of our square surface, it should appear again coming through the opposite corner. The way we do this numerically is we span the rows of our information matrices M and W and check if the terraces have crossed each one of the 8 boundaries of our square surface. This is performed by calculating the distance d between the center of the terrace, i. e.,

the Lochkeim coordinates stored in M (or W) and the the boundary in question. For example, the distance (in matrix elements) to the top-right corner would be $d = \sqrt{m^2 + (N-n)^2}$, and the distance to the bottom side would be $d = N - m$. Note that these distances do not change in time. The size of the the terrace, however, grows with each iteration, so that its radius R (in matrix elements) on iteration i will be $R = \nu(i - i_0)$, where ν is the step velocity in matrix elements per iteration, i. e., $\nu = v\delta t/\delta x$, and i_0 is the iteration on which the corresponding Lochkeim formed (remember i_0 uniquely identifies each terrace and is stored in the information matrix). If $R < d$ then the step will not yet have crossed the corresponding boundary. However, if $R > d$ then the step has indeed crossed the boundary and the corresponding notification should be done in our information matrices; effectively, a new terrace has formed on our surface. This terrace will have the same size as the original terrace, and its centre-coordinates will be the same as the original, except displaced appropriately (note that either one or both of these coordinates will now lie outside the $(0, N)$ range). Therefore we add a new row to M (or W if the terrace is already in $c(8 \times 2)$) containing this information. However, we face a small problem with regards to identification of this 'new' terrace, given it actually formed simultaneously with the original terrace. To solve this we note that we will only have to deal with this a maximum of 8 times (corresponding to the crossing of each of the 8 boundaries of our square surface). Further boundary crossing will not occur, as the terrace step will have been completely annihilated by then due to terrace coalescence. Therefore we label these 'new' terraces by adding decimals to i_0, ranging from 0.1 to 0.8 (in 0.1 steps), depending on what boundary crossing they correspond to. However, we take care in ignoring this decimal when computations such as the instantaneous terrace radius are needed.

- The second occurrence that ought to be considered when steps advance

is the coalescence of terraces. This is a crucial phenomenon affecting the (6×6) surface coverage, as when a (6×6) terrace coalesces with a terrace that is already in $c(8\times2)$, the latter phase will propagate to cover the whole combined terrace. Therefore we firstly consider the coalescence of $c(8\times2)$ terraces amongst themselves. We do this by spanning the existing terraces, annotated in information matrix W, and check which have coalesced on this loop iteration. This is done by comparing the distance d between terrace center-points (stored in W) with the instantaneous value of the sum of their radii, R_1 and R_2. That is, when the terrace sizes becomes big enough so that $R_1 + R_2 > d$, then the terraces have coalesced. The key thing is notifying within W that the two terraces have coalesced and now form one combined terrace. We do this by writing the identifier i_0 of the smaller (younger) terrace within the row of the larger larger (older) terrace. Note that in subsequent and hence generic coalescence events, we will be checking for coalesce of $c(8\times2)$ terrace 'clusters'. Therefore the row of the larger terrace will contain the identifiers of all of the smaller circular terraces making up the 'cluster'. We pile these by making use of a third dimension in information matrix W. Furthermore, when a terrace crosses a boundary, as explained above, we note that the original and 'new' terrace form a 'cluster', and therefore we write the identifier of the 'new' terrace (containing the appropriate decimal) within the row of the original terrace in W.

Next we check what (6×6) terraces have coalesced and we notify this in information matrix M. The methodology is the exact same as the one performed for the $c(8\times2)$ terraces, and will therefore not be elaborated on.

Having checked what new (6×6) and $c(8\times2)$ 'cluster' terraces there are, we ought to now check what (6×6) terraces have coalesced with what $c(8\times2)$ terraces. Note that when this happens, the combined terrace ought be $c(8\times2)$. We notify this in our information matrices M and W

by eliminating the corresponding rows in M and appending them in W. Furthermore, the identifiers i_0 of the smaller terraces making up the new 'cluster' are added to the row of the largest terrace of the cluster, making use of a third dimension in matrix W if necessary.

3. **Producing the new surface matrix S.** Now that matrices M and W contain the updated information regarding the (6×6) and $c(8 \times 2)$ terraces on the surface, respectively, we may proceed to update surface matrix S.

   Recall that the simulation begins with a pristine $c(8 \times 2)$ surface, with no steps or (6×6) domains present. Our $N \times N$ surface matrix S will thus consist of all 1's. When exporting S as an image, each of its elements becomes a pixel, and a matrix element containing a 1 will translate into a light-coloured pixel. However, in a generic loop iteration, the surface will contain steps and (6×6) terraces. We will therefore have to swap some of the 1's in S to 0's, which then represent dark-coloured pixels on the exported image. We start by putting in the steps corresponding to the $c(8 \times 2)$ terraces. We therefore span the $c(8 \times 2)$ terraces in information matrix W. Note that now they will be organized into terrace 'clusters' of individual circular terraces that have coalesced. The terrace edges will now be located at radial distance $R = \nu\,(i - i_0)$, where i is the current loop iteration and i_0 is the iteration on which the terrace formed. Therefore we set to 0 those elements that lie inside the given terrace within a certain distance of the terrace boundary. In practice we choose the step thickness to be 2 matrix elements (i. e. 20 nm). When dealing with a 'cluster' of coalesced terraces we take care to not draw a step where the individual circular terraces overlap. Therefore, if for a $c(8 \times 2)$ terrace cluster we do not need to set a single matrix element to 0 it means that sufficient $c(8 \times 2)$ circular surface terraces have coalesced to cover the entire surface. We can hence forget about this $c(8 \times 2)$ terrace cluster and delete from W all of the individual circular terraces (rows in W) that make it up. In this manner our information matrix W will not grow indefinitely and our simulations can run as long as we wish.

Having drawn our $c(8 \times 2)$ terraces on S, we now proceed to draw our (6×6) terraces. This is done in the exact same manner as done when drawing the steps, however we set to 0 all of the matrix elements within the terraces boundaries, which lie at $R = \nu\,(i - i_0)$ from the respective terrace centres. When doing this we simultaneously compute the surface area of our (6×6) terraces by counting the number of matrix elements that we set to 0, and we store these values in M. Note that we will need to know these areas in order to decide whether a nucleation event will occur on them. We also need them in order to calculate the instantaneous (6×6) coverage on the surface. Note that here we use surface matrix S to update our information matrices. This is because it is simpler to calculate the area of a cluster of coalesced circles numerically in this manner than to try to do it analytically.

At this point our surface matrix S has had the steps and (6×6) terraces drawn onto them and can be exported as an image. The matrix elements that are set to 1 will print out as light-coloured pixels, while the those that have been set 0 will become dark-coloured pixels. We also store the instantaneous value of the (6×6) coverage, which is later used to compute the time-averaged (6×6) coverage as is shown in Fig. 3.13.

4. **Lochkeim nucleation.** The last thing we do in a loop iteration is to check if we need to nucleate new Lochkeime on our surface. Recalling that there are two types of Lochkeime (see Section 3.4); those that form systematically at the centre of $c(8 \times 2)$ terraces when these reach a critical radius R_c and those that form randomly on $c(8 \times 2)$ and (6×6) at respective rates J_w and J_b, we ought to take care of these separately.

    - Firstly, we check if we are to nucleate a systematic Lochkeim on a $c(8 \times 2)$ terrace. To do this we span our $c(8 \times 2)$ terraces to see which of them (if any) achieve a radius $> R_c$ on this loop iteration. This critical $c(8 \times 2)$ terrace radius was measured experimentally and is $R_c \approx 0.17\,\mu$m. On these terraces we place a new Lochkeim around its center. We notify in information matrix M about this new (6×6) terrace by appending a

new row onto it with the information relating to this new terrace. Given random Lochkeim might also form later on this iteration, we again use decimals to identity it, i.e., its identifier will be the present iteration number i_0 plus a some small decimal such as 0.001. If more than one systematic Lochkeim forms on this iteration, the relevant decimal will be $\epsilon \times 0.001$, where ϵ spans 1, 2, 3... We also make a note in W that this Lochkeim has formed inside the relevant $c(8 \times 2)$ terrace. This also enables us to distinguish between atomic layers, so that if the $c(8 \times 2)$ terrace is on layer 0, the new (6×6) terrace will be on layer -1. We make a note in M of the layer on which each terrace is. This facilitates checking for terrace coalescence (as described previously), as only terraces that are on the same layer can coalesce. As a side note, we do not place a Lochkeim within a $c(8 \times 2)$ terrace that attains the critical radius R_c if it already has another terrace within (coming from another of the circular terraces making up its cluster).

- After having checked if new Lochkeime form on critically-sized $c(8 \times 2)$ terraces, we now see if we need to nucleate a new random Lochkeim on our surface. As described earlier, the probability that a Lochkeim forms on the $c(8 \times 2)$ surface during any given for-loop iteration is $p_w = J_w A \delta t$, where J_w is the rate of Lochkeim formation per unit area and A is the area of our GaAs(001) surface. Furthermore, as described in Section 3.4, a Lochkeim can form on (6×6) giving rise to the inverted wedding cake structures. For simplicity, we only let one Lochkeim form per (6×6) terrace. Therefore, the probability that a Lochkeim will form on (6×6) during a given iteration is $p_b = J_b A_b \delta t$, where J_b is the rate of Lochkeim formation on (6×6) and A_b is the total area of (6×6) terraces that do not yet have another terrace within them. Now, in order to decide if a Lochkeim will form on our surface during this loop iteration, we generate a random number ξ. If $0 < \xi < p_w$ then a Lochkeim will form on $c(8 \times 2)$. If, alternatively, $p_w < \xi < p_w + p_b$ then a Lochkeim will form on some

(6×6) terrace that does not yet have another terrace inside. Lastly, if $p_w + p_b < \xi < 1$ then a Lochkeim will not form anywhere on this iteration. Note that we ought to chose our timestep δt small enough to that $p_w + p_b << 1$.

In the first case, i. e., that of having a Lochkeim form somewhere on $c(8 \times 2)$ surface, we generate again random numbers that will determine where on the surface the Lochkeim will be located. Given we can't have this Lochkeim form on (6×6) neither within a $c(8 \times 2)$ terrace that can still produce a Lochkeim around its centre when it reaches critical radius R_c, we generate the Lochkeim's coordinates repeatedly until valid ones are produced. When these are found we append a new row in M with the information regarding this new Lochkeim.

In the second case, i.e., that of having a Lochkeim form on (6×6), we first ought to determine within which of the available (6×6) terraces the Lochkeim ought to form. This will be decided by a new random number ξ. If we label the q available terraces from 1 to q, and therefore their surface areas from A_1 to A_q, then the Lochkeim will form on the terrace s that satisfies $\sum_{j=1}^{s-1} A_j/A_b < \xi < \sum_{j=1}^{s} A_j/A_b$, where $A_b = \sum_{j=1}^{q} A_j$ and $A_0 = 0$. Once the terrace has been decided, then new random numbers are generated in order to determine the coordinates of the Lochkeim within the chosen (6×6) terrace. After this, information matrix M is notified of the formation of this new Lochkeim.

These tasks complete a full iteration of the for-loop. This sequence of tasks is thus repeated over and over as the simulation proceeds.

Appendix C

Solving the Ga Reaction-Diffusion Equation

In this appendix we will explain how the Ga reaction-diffusion equation is solved. Firstly, we state the fundamental problem, and then go on to treating both the steady-state and the time-dependent versions.

The Ga reaction-diffusion equation is a boundary value problem (BVP) given by the following differential equation

$$\frac{\partial C_{\mathrm{Ga}}}{\partial t} = D_{\mathrm{Ga}} \left(\frac{\partial^2 C_{\mathrm{Ga}}}{\partial r^2} + \frac{1}{r} \frac{\partial C_{\mathrm{Ga}}}{\partial r} \right) - k_r \left[C_{\mathrm{Ga}} C_{\mathrm{As}} - (C_{\mathrm{Ga}} C_{\mathrm{As}})_{eq} \right], \tag{C.1}$$

for $t > 0$ and $r_D < r < L$. In addition to this, two boundary conditions are supplied. One at the droplet edge (at $r = r_D$), and the other halfway to the next droplet (at $r = L$).

At $r = r_D$ we set the boundary condition

$$- D_{\mathrm{Ga}} \left. \frac{\partial C_{\mathrm{Ga}}}{\partial r} \right|_{r=r_D} = k_D \left(C^l_{\mathrm{Ga}} - C_{\mathrm{Ga}}|_{r=r_D} \right), \tag{C.2}$$

where k_D is a rate constant associated to Ga adatom attachment to the droplet. This equation merely reflects conservation of mass for Ga transport across the contact line; the left-hand-side is the adatom flux immediately outside of the droplet, and the right-hand-side equals the net Ga supply of the droplet to the surface. In the limit

of fast attachment/detachment compared to adatom diffusion, Eq. (C.2) becomes

$$C_{\mathrm{Ga}}|_{r=r_D} = C^l_{\mathrm{Ga}}. \tag{C.3}$$

This states that the Ga adatom concentration at the contact line is that of equilibrium with liquid Ga.

At $r = L$ the boundary condition ought to reflect zero net Ga transport. This implies having a null C_{Ga}, that is

$$\left.\frac{\partial C_{\mathrm{Ga}}}{\partial r}\right|_{r=L} = 0. \tag{C.4}$$

The BVP at hand is thus given by the partial differential equation given by Eq. (C.1) and the boundary conditions of Eq. (C.3) and Eq. (C.4).

C.1 Solving the Steady-State Reaction-Diffusion Equation

The steady-state solution to our BVP is that which is time-independent, i.e., $\partial C_{\mathrm{Ga}}/\partial t = 0$. Eq. C.1 transforms simply to

$$D_{\mathrm{Ga}}\left(\frac{\partial^2 C_{\mathrm{Ga}}}{\partial r^2} + \frac{1}{r}\frac{\partial C_{\mathrm{Ga}}}{\partial r}\right) - k_r\left[C_{\mathrm{Ga}}C_{\mathrm{As}} - (C_{\mathrm{Ga}}C_{\mathrm{As}})_{eq}\right] = 0. \tag{C.5}$$

Defining the natural radial coordinate ρ as

$$\rho \equiv \frac{r}{L_{\mathrm{Ga}}}, \tag{C.6}$$

which spans from $\rho_D \equiv r_D/L_{\mathrm{Ga}}$ to $\rho_L \equiv L/L_{\mathrm{Ga}}$ (where we recall $L_{\mathrm{Ga}} = \sqrt{D_{\mathrm{Ga}}\tau_{\mathrm{Ga}}}$ is the Ga diffusion length before reaction with As), Eq. C.5 simplifies to

$$\frac{\mathrm{d}^2 C_{\mathrm{Ga}}}{\mathrm{d}\rho^2} + \frac{1}{\rho}\frac{\mathrm{d}C_{\mathrm{Ga}}}{\mathrm{d}\rho} - C_{\mathrm{Ga}} + \frac{(C_{\mathrm{Ga}}C_{\mathrm{As}})_{eq}}{F_{\mathrm{As}}\tau_{\mathrm{As}}} = 0, \tag{C.7}$$

where $C_{\mathrm{As}} = F_{\mathrm{As}}\tau_{\mathrm{As}}$ has been introduced. Given that Eq. (C.7) is the modified Bessel equation of zeroth order with inhomogeneous term $(C_{\mathrm{Ga}}C_{\mathrm{As}})_{eq}/F_{\mathrm{As}}\tau_{\mathrm{As}}$, we note its general solution must be

$$C_{\mathrm{Ga}}(\rho) = AI_0(\rho) + BK_0(\rho) + \frac{(C_{\mathrm{Ga}}C_{\mathrm{As}})_{eq}}{F_{\mathrm{As}}\tau_{\mathrm{As}}}, \tag{C.8}$$

where I_0 and K_0 are the modified Bessel functions of zeroth order, and A and B are arbitrary constants. Imposing the boundary conditions of Eq. (C.3) and Eq. (C.4) yields $A \to 0$ (for $L \gg L_{\mathrm{Ga}}$, r_D), while B is simply

$$B = \frac{C^l_{\mathrm{Ga}} - C^L_{\mathrm{Ga}}}{K_0(\rho_D)}, \tag{C.9}$$

where $C^L_{\mathrm{Ga}} \equiv (C_{\mathrm{Ga}}C_{\mathrm{As}})_{eq}/(F_{\mathrm{As}}\tau_{\mathrm{As}})$. Therefore, the As-on steady-state Ga concentration profile is

$$C_{\mathrm{Ga}}(r) = BK_0(r/L_{\mathrm{Ga}}) + \frac{(C_{\mathrm{Ga}}C_{\mathrm{As}})_{eq}}{F_{\mathrm{As}}\tau_{\mathrm{As}}}, \tag{C.10}$$

with B given by Eq. (C.9).

C.2 Soving the Time-Dependent Reaction-Diffusion Equation

Let us now consider solving the full time-dependent BVP. In order to facilitate this, it is convenient to define two new variables apart from the radial coordinate of Eq. (C.6). We define a new time coordinate u as

$$u = \frac{t}{\tau_{\mathrm{Ga}}}, \tag{C.11}$$

where we recall $\tau_{\mathrm{Ga}} \equiv 1/(k_r C_{\mathrm{As}})$. We also define a new Ga concentration variable K_{Ga} as

$$K_{\mathrm{Ga}} = C_{\mathrm{Ga}} - C^{ss}_{\mathrm{Ga}}, \tag{C.12}$$

where C_{Ga}^{ss} is the steady-state solution to the BVP, i.e., that of Eq. (C.10). Introducing these changes into Eq. (C.1) gives

$$\frac{\partial}{\partial u}K_{\mathrm{Ga}} = \Lambda K_{\mathrm{Ga}} \tag{C.13}$$

where Λ is the *reaction-diffusion operator* given by

$$\Lambda \equiv \frac{\partial^2}{\partial \rho^2} + \frac{1}{\rho}\frac{\partial}{\partial \rho} - 1. \tag{C.14}$$

Likewise, the boundary conditions are now

$$K_{\mathrm{Ga}}|_{\rho=\rho_D} = 0, \tag{C.15}$$

and

$$\frac{\partial K_{\mathrm{Ga}}}{\partial \rho}|_{\rho=\rho_L} = 0. \tag{C.16}$$

According to Sturm Liouville theory (see, for example, Ref. [138]), one can write the solution $K(\rho, u)$ to our BVP (now consisting of Eq. (C.13) and the boundary conditions of Eq. (C.15)) and Eq. (C.16) as a linear combination of orthonormal non-degenerate eigenfunctions of Λ. Thus, we may write

$$K_{\mathrm{Ga}} = \sum_{n=1}^{\infty} c_n(u)\phi_n(\rho), \tag{C.17}$$

where $\phi_n(\rho)$ are eigenfunctions of Λ, and $c_n(u)$ are time-dependent coefficients. The fact that the eigenfunctions are orthonormal means they obey

$$\int_{\rho_D}^{\rho_L} \rho\phi_n(\rho)\phi_m(\rho)\mathrm{d}\rho = \delta_{nm}. \tag{C.18}$$

Substituting Eq. C.19 into Eq. (C.13) yields

$$K_{\mathrm{Ga}} = \sum_{n=1}^{\infty} c_n^0 \exp(-a_n u)\phi_n(\rho). \tag{C.19}$$

Here $-a_n$ are the eigenvalues of Λ associated to eigenfunctions $\phi_n(\rho)$, and c_n^0 are the

coefficients of the initial $K^0_{\rm Ga}(\rho) \equiv K_{\rm Ga}(\rho, u = 0)$ in the $\phi_n(\rho)$ basis, given by the scalar product

$$c^0_n = \int_{\rho_D}^{\rho_L} \rho K^0_{\rm Ga}(\rho)\phi_n(\rho)\mathrm{d}\rho. \tag{C.20}$$

Let us now find the eigenvalues and eigenfunctions of operator Λ. The eigenvalue problem is

$$\Lambda\phi_n + a_n\phi_n = 0, \tag{C.21}$$

or

$$\frac{\mathrm{d}^2\phi_n}{\mathrm{d}\rho^2} + \frac{1}{\rho}\frac{\mathrm{d}\phi_n}{\mathrm{d}\rho} + (a_n - 1)\phi_n = 0. \tag{C.22}$$

Defining modified eigenvalues $\lambda_n \equiv \sqrt{a_n - 1}$, and defining a new variable $\xi \equiv \lambda_n\rho$, Eq. (C.22) becomes

$$\frac{\mathrm{d}^2\phi_n}{\mathrm{d}\xi^2} + \frac{1}{\xi}\frac{\mathrm{d}\phi_n}{\mathrm{d}\xi} + \phi_n = 0. \tag{C.23}$$

This is precisely Bessel's equation of zeroth order, whose general solution (undoing the change of variables) is

$$\phi_n(\rho) = AJ_0(\lambda_n\rho) + BY_0(\lambda_n\rho), \tag{C.24}$$

. where A and B are arbitrary integration constants, and J_0 and Y_0 are, respectively, the Bessel functions of first and second kind of order zero.

Applying now the boundary conditions of Eq. (C.15) and Eq. (C.16) gives two equation linear in A and B. One can put these into matrix form to get

$$\begin{bmatrix} J_0(\lambda_n\rho_D) & Y_0(\lambda_n\rho_D) \\ J_1(\lambda_n\rho_L) & Y_1(\lambda_n\rho_L) \end{bmatrix} \begin{bmatrix} A \\ B \end{bmatrix} = \begin{bmatrix} 0 \\ 0 \end{bmatrix} \tag{C.25}$$

where J_1 and Y_1 are, respectively, the ordinary and modified Bessel functions of first order. As the eigenfunctions ought to form a one-dimansional space, the determinant of the matrix in Eq. (C.25) ought to be zero, i.e.,

$$J_0(\lambda_n\rho_D)Y_1(\lambda_n\rho_L) - J_1(\lambda_n\rho_L)Y_0(\lambda_n\rho_D) = 0. \tag{C.26}$$

This is the characteristic equation of our eigenvalue problem. The λ_n-solutions

are the modified eigenvalues of Λ. The nominal eigenvalues are then $-a_n = -(\lambda^2+1)$.

Substituting now any of the two equations in Eq. (C.25) into Eq. (C.24) we obtain the following expression for the eigenfunctions

$$\phi_n(\rho) = k_n \left[Y_0(\lambda_n \rho_D) J_0(\lambda_n \rho) - J_0(\lambda_n \rho_D) Y_0(\lambda_n \rho) \right], \tag{C.27}$$

where k_n are normalization constants. These constants can be calculated imposing the unit norm upon the eigenfunction $\phi_n(\rho)$, i.e., $\int_{\rho_D}^{\rho_L} \rho \phi_n(\rho)^2 \mathrm{d}\rho = 1$. This yields

$$\begin{aligned} \frac{2}{k_n^2} = \rho_L^2 \left[(J_0(\lambda_n \rho_D) Y_0(\lambda_n \rho_L) - J_0(\lambda_n \rho_L) Y_0(\lambda_n \rho_D))^2 + (J_0(\lambda_n \rho_D) Y_1(\lambda_n \rho_L) - J_1(\lambda_n \rho_L) Y_0(\lambda_n \rho_D))^2 \right] \\ - \rho_D^2 (J_0(\lambda_n \rho_D) Y_1(\lambda_n \rho_D) - J_1(\lambda_n \rho_D) Y_0(\lambda_n \rho_D))^2 \end{aligned} \tag{C.28}$$

Undoing the changes of variables of Eq. (C.6), (C.11), and (C.12), we can write the solution to the original BVP defined by Eq. (C.1), (C.3), and (C.4) as

$$C_{\mathrm{Ga}}(r,t) = C_{\mathrm{Ga}}^{ss}(r) + \sum_{n=1}^{\infty} c_n^0 \exp(-a_n t/\tau_{\mathrm{Ga}}) \phi_n(r/L_{\mathrm{Ga}}). \tag{C.29}$$

To numerically evaluate the time-dependent Ga concentration profiles of Eq. (C.29), it is sufficient to assign values to concentrations C_{Ga}^l and $C_{\mathrm{Ga}}^L = (C_{\mathrm{Ga}} C_{\mathrm{As}})_{eq}/(F_{\mathrm{As}} \tau_{\mathrm{As}})$, and to the radial coordinates ρ_D and ρ_L.

Bibliography

[1] Akihiro Ohtake. Surface reconstructions on GaAs(001). *Surf. Sci. Rep.*, 63(7):295 – 327, 2008.

[2] Akihiro Ohtake, Pavel Kocán, Kaori Seino, Wolf G. Schmidt, and Nobuyuki Koguchi. Ga-rich limit of surface reconstructions on GaAs(001): Atomic structure of the (4×6) phase. *Phys. Rev. Lett.*, 93:266101, 2004.

[3] M S Altman. Trends in low energy electron microscopy. *J. Phys.: Condens. Matter*, 22(8):084017, 2010.

[4] C. X. Zheng, J. Tersoff, W. X. Tang, A. Morreau, and D. E. Jesson. Novel GaAs surface phases via direct control of chemical potential. *Phys. Rev. B*, 93:195314, 2016.

[5] Y.R. Niu, J. Pereiro, D. Gomez, and D.E. Jesson. Selected energy dark-field imaging using low energy electrons for optimal surface phase discrimination. *Ultramicroscopy*, 200:79 – 83, 2019.

[6] J. B. Hannon, F.-J. Meyer zu Heringdorf, J. Tersoff, and R. M. Tromp. Phase coexistence during surface phase transitions. *Phys. Rev. Lett.*, 86:4871–4874, 2001.

[7] A. Nemcsics, L. Toth, L. Dobos, Ch. Heyn, A. Stemmann, A. Schramm, H. Welsch, and W. Hansen. Composition of the GaAs quantum dot, grown by droplet epitaxy. *Superlattice Microst.*, 48(4):351 – 357, 2010.

[8] C. Somaschini, S. Bietti, N. Koguchi, and S. Sanguinetti. Fabrication of multiple concentric nanoring structures. *Nano Lett.*, 9(10):3419–3424, 2009. PMID: 19764709.

[9] Ch. Heyn, A. Stemmann, R. Eiselt, and W. Hansen. Influence of Ga coverage and As pressure on local droplet etching of nanoholes and quantum rings. *J. Appl. Phys.*, 105(5):054316, 2009.

[10] K. Seino, W. G. Schmidt, and A. Ohtake. Ga-rich GaAs(001) surface from ab initio calculations: Atomic structure of the (4×6) and (6×6) reconstructions. *Phys. Rev. B*, 73:035317, 2006.

[11] Ch. Heyn, A. Stemmann, T. Kppen, Ch. Strelow, T. Kipp, M. Grave, S. Mendach, and W. Hansen. Highly uniform and strain-free GaAs quantum dots fabricated by filling of self-assembled nanoholes. *Appl. Phys. Lett.*, 94(18):183113, 2009.

[12] David Fuster, Yolanda González, and Luisa González. Fundamental role of arsenic flux in nanohole formation by Ga droplet etching on GaAs(001). *Nanoscale Res. Lett.*, 9(1):309, 2014.

[13] Jinmin Li and Guo-Qiang Zhang. *Light-Emitting Diodes: Materials, Processes, Devices and Applications*, volume 4. Springer, 2019.

[14] Charles Cornet, Yoan Léger, and Cédric Robert. *Integrated lasers on silicon.* Elsevier, 2016.

[15] Simon P. Philipps, Frank Dimroth, and Andreas W. Bett. Chapter i-4-b - high-efficiency III-V multijunction solar cells. In Soteris A. Kalogirou, editor, *McEvoy's Handbook of Photovoltaics (Third Edition)*, pages 439 – 472. Academic Press, third edition, 2018.

[16] J. F. Geisz, R. M. France, K. L. Schulte, M. A. Steiner, A. G. Norman, H. L. Guthrey, M. R. Young, T. Song, and T. Moriarty. Six-junction III-V solar cells with 47.1% conversion efficiency under 143 suns concentration. *Nat. Energy*, 5:326–335, 2020.

[17] R R LaPierre, M Robson, K M Azizur-Rahman, and P Kuyanov. A review of iii-v nanowire infrared photodetectors and sensors. *J Phys D Appl Phys*, 50(12):123001, 2017.

[18] Gaute Otnes and Magnus T. Borgstrm. Towards high efficiency nanowire solar cells. *Nano Today*, 12:31 – 45, 2017.

[19] Edik U Rafailov, Maria Ana Cataluna, and Eugene A Avrutin. *Ultrafast lasers based on quantum dot structures: physics and devices*. John Wiley & Sons, 2011.

[20] Mark J Holmes, M Arita, and Y Arakawa. III-nitride quantum dots as single photon emitters. *Semicond. Sci. Technol.*, 34(3):033001, 2019.

[21] D. Jacobsson, P. Panciera, J. Tersoff, M. C. Reuter, S. Lehmann, S. Hofmann, K. A. Dick, and F. M. Ross. Interface dynamics and crystal phase switching in GaAs nanowires. *Nature*, 531:317–322, 2016.

[22] J. Y. Tsao, T. M. Brennan, J. F. Klem, and B. E. Hammons. Surface stoichiometry dependence of As_2 desorption and As_4 'reflection' from GaAs(001). *J. Vac. Sci. Technol. A*, 7(3):2138–2142, 1989.

[23] J. R. Arthur Jr. Interaction of Ga and As_2 molecular beams with GaAs surfaces. *J. Appl. Phys.*, 39(8):4032–4034, 1968.

[24] M. Itoh, G. R. Bell, A. R. Avery, T. S. Jones, B. A. Joyce, and D. D. Vvedensky. Island nucleation and growth on reconstructed GaAs(001) surfaces. *Phys. Rev. Lett.*, 81:633–636, 1998.

[25] C.T Foxon and B.A Joyce. Interaction kinetics of As_2 and Ga on (100)GaAs surfaces. *Surf. Sci.*, 64(1):293 – 304, 1977.

[26] C.T. Foxon and B.A. Joyce. Interaction kinetics of As_4 and Ga on 100 GaAs surfaces using a modulated molecular beam technique. *Surf. Sci.*, 50(2):434 – 450, 1975.

[27] J. Y. Tsao, T. M. Brennan, and B. E. Hammons. Reflection mass spectrometry of As incorporation during GaAs molecular beam epitaxy. *Appl. Phys. Lett.*, 53(4):288–290, 1988.

[28] T. M. Brennan, J. Y. Tsao, and B. E. Hammons. Reactive sticking of As_4 during molecular beam homoepitaxy of GaAs, AlAs, and InAs. *J. Vac. Sci. Technol. A*, 10(1):33–45, 1992.

[29] A. Y. Cho. GaAs epitaxy by a molecular beam method: Observations of surface structure on the (001) face. *J. Appl. Phys.*, 42(5):2074–2081, 1971.

[30] J.R. Arthur. Surface stoichiometry and structure of GaAs. *Surf. Sci.*, 43(2):449 – 461, 1974.

[31] S. Koshiba, I. Tanaka, Y. Nakamura, H. Noge, and H. Sakaki. Ultrahigh vacuum atomic force microscope study of 10-30 nm scale GaAs ridge structure formation by molecular beam epitaxy. *Appl. Phys. Lett.*, 70(7):883–885, 1997.

[32] Shiro Tsukamoto, Tsuyoshi Honma, Gavin R. Bell, Akira Ishii, and Yasuhiko Arakawa. Atomistic insights for InAs quantum dot formation on GaAs(001) using STM within a MBE growth chamber. *Small*, 2(3):386–389, 2006.

[33] Federico Panciera, Jerry Tersoff, Andrew D. Gamalski, Mark C. Reuter, Dmitri Zakharov, Eric A. Stach, Stephan Hofmann, and Frances M. Ross. Surface crystallization of liquid Au-Si and its impact on catalysis. *Adv. Mater.*, 31(5):1806544, 2019.

[34] In situ STM observations of step structures in a trench around an InAs QD at 300°C. *J. Cryst. Growth*, 378:44 – 46, 2013. The 17th International Conference on Molecular Beam Epitaxy.

[35] Takashi Toujyou and Shiro Tsukamoto. In situ STM observation during InAs growth in nano holes at 300°C. *Surf. Sci.*, 605(13):1320 – 1323, 2011.

[36] D. E. Jesson and W. X. Tang. Surface electron microscopy of Ga droplet dynamics on GaAs(001). *Microsc. Sci. Technol. Appl. Educ.*, 3:1608–1619, 2010.

[37] J. Tersoff, D. E. Jesson, and W. X. Tang. Running droplets of gallium from evaporation of gallium arsenide. *Science*, 324(5924):236–238, 2009.

[38] J. Tersoff, D. E. Jesson, and W. X. Tang. Decomposition controlled by surface morphology during langmuir evaporation of GaAs. *Phys. Rev. Lett.*, 105:035702, 2010.

[39] Z. Y. Zhou, C. X. Zheng, W. X. Tang, J. Tersoff, and D. E. Jesson. Origin of quantum ring formation during droplet epitaxy. *Phys. Rev. Lett.*, 111:036102, 2013.

[40] K. Hannikainen, D. Gomez, J. Pereiro, Y. R. Niu, and D. E. Jesson. Surface phase metastability during langmuir evaporation. *Phys. Rev. Lett.*, 123:186102, 2019.

[41] C. X. Zheng, K. Hannikainen, Y. R. Niu, J. Tersoff, D. Gomez, J. Pereiro, and D. E. Jesson. Mapping the surface phase diagram of GaAs(001) using droplet epitaxy. *Phys. Rev. Materials*, 3:124603, 2019.

[42] Zh. M. Wang, B. L. Liang, K. A. Sablon, and G. J. Salamo. Nanoholes fabricated by self-assembled gallium nanodrill on GaAs(100). *Appl. Phys. Lett.*, 90(11):113120, 2007.

[43] A. Stemmann, Ch. Heyn, T. Koppen, T. Kipp, and W. Hansen. Local droplet etching of nanoholes and rings on GaAs and AlGaAs surfaces. *Appl. Phys. Lett.*, 93(12):123108, 2008.

[44] Ch. Heyn, A. Stemmann, and W. Hansen. Nanohole formation on AlGaAs surfaces by local droplet etching with gallium. *J. Cryst. Growth*, 311(7):1839 – 1842, 2009. International Conference on Molecular Beam Epitaxy (MBE-XV).

[45] Ch. Heyn, A. Stemmann, and W. Hansen. Dynamics of self-assembled droplet etching. *Appl. Phys. Lett.*, 95(17):173110, 2009.

[46] Christian Heyn, Sandra Schnüll, David E. Jesson, and Wolfgang Hansen. Thermally controlled widening of droplet etched nanoholes. *Nanoscale Res. Lett.*, 9(1):285, 2014.

[47] Christian Heyn, Thorben Bartsch, Stefano Sanguinetti, David Jesson, and Wolfgang Hansen. Dynamics of mass transport during nanohole drilling by local droplet etching. *Nanoscale Res. Lett.*, 10(1):67, 2015.

[48] B. L. Liang, Zh. M. Wang, J. H. Lee, K. Sablon, Yu. I. Mazur, and G. J. Salamo. Low density InAs quantum dots grown on GaAs nanoholes. *Appl. Phys. Lett.*, 89(4):043113, 2006.

[49] Ch. Heyn, A. Kster, A. Grfenstein, A. Ungeheuer, A. Graf, and W. Hansen. GaAs quantum dot molecules filled into droplet etched nanoholes. *J. Cryst. Growth*, 477:235 – 238, 2017. Proceeding of the 19th International Conference on Molecular Beam Epitaxy.

[50] Kster A., C. Heyn, and A. *et al* Ungeheuer. Droplet etching of deep nanoholes for filling with self-aligned complex quantum structures. *Nanoscale Res. Lett.*, 11:282, 2016.

[51] W. K. Burton, N. Cabrera, and F. C. Frank. The growth of crystals and the equilibrium structure of their surfaces. *Philos. T. R. Soc. A*, 243, 1951.

[52] J. Y. Tsao. *Materials Fundamentals of Molecular Beam Epitaxy.* Academic Press, San Diego, 1993.

[53] Alberto Pimpinelli and Jacques Villain. *Physics of Crystal Growth.* Collection Alea-Saclay: Monographs and Texts in Statistical Physics. Cambridge University Press, 1998.

[54] H.B. Callen. *Thermodynamics and an Introduction to Thermostatistics.* Wiley, 1985.

[55] C. G. Morgan, P. Kratzer, and M. Scheffler. Arsenic dimer dynamics during MBE growth: Theoretical evidence for a novel chemisorption state of As_2 molecules on GaAs surfaces. *Phys. Rev. Lett.*, 82:4886–4889, 1999.

[56] J. Tersoff, M. D. Johnson, and B. G. Orr. Adatom densities on GaAs: Evidence for near-equilibrium growth. *Phys. Rev. Lett.*, 78:282–285, 1997.

[57] Otto Redlich and A. T. Kister. Algebraic representation of thermodynamic properties and the classification of solutions. *J. Ind. Eng. Chem.*, 40(2):345–348, 1948.

[58] I. Ansara, C. Chatillon, H.L. Lukas, T. Nishizawa, H. Ohtani, K. Ishida, M. Hillert, B. Sundman, B.B. Argent, A. Watson, T.G. Chart, and T. Anderson. A binary database for III-V compound semiconductor systems. *Calphad*, 18(2):177 – 222, 1994.

[59] Conyers Herring. Surface tension as a motivation for sintering. In *The Physics of Powder Metallurgy*, pages 143–179. McGraw-Hill, New York, 1951.

[60] Morton E. Gurtin and Michel E. Jabbour. Interface evolution in three dimensions with curvature-dependent energy and surface diffusion: Interface-controlled evolution, phase transitions, epitaxial growth of elastic films. *Arch. Ration. Mech. An.*, 163(3):171–208, 2002.

[61] A Matrobernardino and B. J. Spencer. Three-dimensional equilibrium crystal shapes with corner energy regularization. 75(2):190–205, 2010.

[62] K. W. Schwarz and J. Tersoff. From droplets to nanowires: Dynamics of vapor-liquid-solid growth. *Phys. Rev. Lett.*, 102:206101, 2009.

[63] J. Tersoff, A. W. Denier van der Gon, and R. M. Tromp. Critical island size for layer-by-layer growth. *Phys. Rev. Lett.*, 72:266–269, 1994.

[64] Robert Gomer. Diffusion of absorbates on metal surfaces. *Rep. Prog. Phys.*, 53:917–1002, 1990.

[65] M. D. Pashley and K. W. Haberern. *The Role of Surface Reconstructions in MBE Growth of GaAs*, pages 63–73. Springer Netherlands, Dordrecht, 1993.

[66] Vincent P. LaBella, Michael R. Krause, Zhao Ding, and Paul M. Thibado. Arsenic-rich GaAs(001) surface structure. *Surf. Sci. Rep.*, 60(1):1 – 53, 2005.

[67] Bruce A. Joyce and Dimitri D. Vvedensky. Self-organized growth on GaAs surfaces. *Materials Science and Engineering: R: Reports*, 46(6):127 – 176, 2004.

[68] Qikun Xue, T. Hashizume, J. M. Zhou, T. Sakata, T. Ohno, and T. Sakurai. Structures of the Ga-rich (4×2) and (4×6) reconstructions of the GaAs(001) surface. *Phys. Rev. Lett.*, 74:3177–3180, 1995.

[69] James G. McLean, Peter Kruse, and Andrew C. Kummel. Atomic structure determination for GaAs(001)-(6×6) by STM. *Surf. Sci.*, 424(2):206 – 218, 1999.

[70] Sung-Hoon Lee, Wolfgang Moritz, and Matthias Scheffler. GaAs(001) surface under conditions of low As pressure: Evidence for a novel surface geometry. *Phys. Rev. Lett.*, 85:3890–3893, 2000.

[71] Akihiro Ohtake, Shiro Tsukamoto, Markus Pristovsek, Nobuyuki Koguchi, and Masashi Ozeki. Structure analysis of the Ga-stabilized GaAs(001)-$c(8 \times 2)$ surface at high temperatures. *Phys. Rev. B*, 65:233311, 2002.

[72] Akihiro Ohtake, Jun Nakamura, Shiro Tsukamoto, Nobuyuki Koguchi, and Akiko Natori. New structure model for the GaAs(001)-$c(4 \times 4)$ surface. *Phys. Rev. Lett.*, 89:206102, 2002.

[73] M. Pristovsek, S. Tsukamoto, A. Ohtake, N. Koguchi, B. G. Orr, W. G. Schmidt, and J. Bernholc. Gallium-rich reconstructions on GaAs(001). *Phys. Status Solidi B*, 240(1):91–98, 2003.

[74] E. Penev, P. Kratzer, and M. Scheffler. Atomic structure of the GaAs(001)-$c(4 \times 4)$ surface: First-principles evidence for diversity of heterodimer motifs. *Phys. Rev. Lett.*, 93:146102, 2004.

[75] Masamitu Takahasi and Jun'ichiro Mizuki. Element-specific surface x-ray diffraction study of GaAs(001)-$c(4 \times 4)$. *Phys. Rev. Lett.*, 96:055506, 2006.

[76] Akihiro Ohtake. Structure and composition of Ga-rich (6×6) reconstructions on GaAs(001). *Phys. Rev. B*, 75:153302, 2007.

[77] Elizabeth A. Wood. Vocabulary of surface crystallography. *J. Appl. Phys.*, 35(4):1306–1312, 1964.

[78] Bernd Meyer. Surface phase diagrams from ab initio thermodynamics. In Johaness Grotendorst, Stefan Blugel, and Dominik Marx, editors, *Computational Nanoscience: Do It Yourself! (NIC Series)*, volume 31, pages 411–418. John von Neumann Institute for Computing (NIC), 2006.

[79] M. P. Seah and W. A. Dench. Quantitative electron spectroscopy of surfaces: A standard data base for electron inelastic mean free paths in solids. *Surf. Interface Anal.*, 1(1):2–11, 1979.

[80] W. Telieps and E. Bauer. An analytical reflection and emission UHV surface electron microscope. *Ultramicroscopy*, 17(1):57 – 65, 1985.

[81] M.S. Altman and E. Bauer. The reconstructions of the Pb(110) surface studied by low energy electron microscopy. *Surf. Sci.*, 344(1):51 – 64, 1995.

[82] W. Swiech and E. Bauer. The growth of Si on Si(100): a video-LEEM study. *Surf. Sci.*, 255(3):219 – 228, 1991.

[83] Z. Y. Zhou, W. X. Tang, D. E. Jesson, and J. Tersoff. Time evolution of the Ga droplet size distribution during langmuir evaporation of GaAs(001). *Appl. Phys. Lett.*, 97(19):191914, 2010.

[84] C. T. Foxon, J. A. Harvey, and B. A. Joyce. The evaporation of GaAs under equilibrium and non-equilibrium conditions using a modulated beam technique. *J. Phys. Chem. Solids*, 34(10):1693 – 1701, 1973.

[85] C. Y. Lou and G. A. Somorjai. Studies of the vaporization mechanism of gallium arsenide single crystals. *J. Chem. Phys.*, 55(9):4554–4565, 1971.

[86] Bernard Goldstein, Daniel J. Szostak, and Vladimir S. Ban. Langmuir evaporation from the (100), (111a), and (111b) faces of GaAs. *Surf. Sci.*, 57(2):733 – 740, 1976.

[87] Christian Chatillon and Dominique Chatain. Congruent vaporization of GaAs(s) and stability of Ga(l) droplets at the GaAs(s) surface. *J. Cryst. Growth*, 151(1):91 – 101, 1995.

[88] N. Isomura, S. Tsukamoto, K. Iizuka, and Y. Arakawa. Investigation on GaAs(001) surface treated by As-free high temperature surface cleaning method. *J. Cryst. Growth*, 301-302:26 – 29, 2007. 14th International Conference on Molecular Beam Epitaxy.

[89] D. Bimberg, M. Grundmann, and N. N. Ledentsov. *Quantum Dot Heterostructures*. Wiley, 1999.

[90] P. Bhattacharya, S. Ghosh, and A. D. Stiff-Roberts. Quantum dot optoelectronic devices. *Annu. Rev. Mater. Res.*, 34(1):1–40, 2004.

[91] J. Orton and T. Foxon. *Molecular Beam Epitaxy: A Short History*. Oxford University Press, 2015.

[92] Emelie Hilner, Alexei A. Zakharov, Karina Schulte, Peter Kratzer, Jesper N. Andersen, Edvin Lundgren, and Anders Mikkelsen. Ordering of the nanoscale step morphology as a mechanism for droplet self-propulsion. *Nano Lett.*, 9(7):2710–2714, 2009.

[93] Changxi Zheng, Wen-Xin Tang, and David E. Jesson. Planar regions of GaAs (001) prepared by Ga droplet motion. *J. Vac. Sci. Technol. A*, 34(4):043201, 2016.

[94] S. B. Zhang and A. Zunger. Structure and formation energy of steps on the GaAs(001)-(2×4) surface. *Mater. Sci. Eng. B-Adv.*, 30(2):127 – 136, 1995.

[95] J. J. Metois and D. E. Wolf. Kinetic surface roughening of Si(001) during sublimation. *Surf. Sci.*, 298(1):71 – 78, 1993.

[96] M. Mundschau, E. Bauer, W. Telieps, and W. Swieh. Atomic steps on Si(100) and step dynamics during sublimation studied by low-energy electron microscopy. *Surf. Sci.*, 223(3):413 – 423, 1989.

[97] Alberto Pimpinelli and Jean-Jacques Métois. Macrovacancy nucleation on evaporating Si(001). *Phys. Rev. Lett.*, 72:3566–3569, 1994.

[98] W. Ostwald. Studien uber die bildung und umwandlung fester korper. *Z. Phys. Chem.*, 22:289–330, 1897.

[99] Sung-Yoon Chung, Young-Min Kim, Jin-Gyu Kim, and Youn-Joong Kim. Multiphase transformation and ostwald's rule of stages during crystallization of a metal phosphate. *Nat. Phys.*, 5:68–73, 2009.

[100] Lester O. Hedges and Stephen Whitelam. Limit of validity of ostwald's rule of stages in a statistical mechanical model of crystallization. *J. Chem. Phys.*, 135(16):164902, 2011.

[101] I. N. Stranski and D. Totomanow. *Z. Phys. Chem.*, 163A:399, 1933.

[102] David Vanderbilt. Phase segregation and work-function variations on metal surfaces: spontaneous formation of periodic domain structures. *Surf. Sci.*, 268(1):L300 – L304, 1992.

[103] Massimo Gurioli, Zhiming Wang, Armando Rastelli, Takashi Kuroda, and Stefano Sanguinetti. Droplet epitaxy of semiconductor nanostructures for quantum photonic devices. *Nat. Mater.*, 18:799–810, 2019.

[104] Toyohiro Chikyow and Nobuyuki Koguchi. MBE growth method for pyramid-shaped GaAs micro crystals on ZnSe(001) surface using Ga droplets. *Jpn J. Appl. Phys.*, 29(11A):L2093, 1990.

[105] Nobuyuki Koguchi, Satoshi Takahashi, and Toyohiro Chikyow. New MBE growth method for InSb quantum well boxes. *J. Crys. Growth*, 111(1):688 – 692, 1991.

[106] Chae-Deok Lee, Chanro Park, Hwack Joo Lee, Kyu-Seok Lee, Seong-Ju Park, Chan Gyung Park, Sam Kyu Noh, and andNobuyuki Koguchi. Fabrication of self-assembled GaAs/AlGaAs quantum dots by low-temperature droplet epitaxy. *Jpn J. Appl. Phys.*, 37(12S):7158, 1998.

[107] Katsuyuki Watanabe, Nobuyuki Koguchi, and Yoshihiko Gotoh. Fabrication of GaAs quantum dots by modified droplet epitaxy. *Jpn J. Appl. Phys.*, 39(2A):L79, 2000.

[108] S Bietti, C Somaschini, and S Sanguinetti. Crystallization kinetics of Ga metallic nano-droplets under As flux. *Nanotechnology*, 24(20):205603, 2013.

[109] T. Mano and N. Koguchi. Nanometer-scale GaAs ring structure grown by droplet epitaxy. *J. Cryst. Growth*, 278:108 – 112, 2005. 13th International Conference on Molecular Beam Epitaxy.

[110] Takaaki Mano, Takashi Kuroda, Stefano Sanguinetti, Tetsuyuki Ochiai, Takahiro Tateno, Jongsu Kim, Takeshi Noda, Mitsuo Kawabe, Kazuaki Sakoda, Giyuu Kido, and Nobuyuki Koguchi. Self-assembly of concentric quantum double rings. *Nano Lett.*, 5(3):425–428, 2005. PMID: 15755088.

[111] Z. Gong, Z. C. Niu, S. S. Huang, Z. D. Fang, B. Q. Sun, and J. B. Xia. Formation of GaAs/AlGaAs and InGaAs/GaAs nanorings by droplet molecular-beam epitaxy. *Appl. Phys. Lett.*, 87(9):093116, 2005.

[112] Shesong Huang, Zhichuan Niu, Zhidan Fang, Haiqiao Ni, Zheng Gong, and Jianbai Xia. Complex quantum ring structures formed by droplet epitaxy. *Appl. Phys. Lett.*, 89(3):031921, 2006.

[113] S. Bietti, C. Somaschini, M. Abbarchi, N. Koguchi, S. Sanguinetti, E. Poliani, M. Bonfanti, M. Gurioli, A. Vinattieri, T. Kuroda, T. Mano, and S. Sakoda. Quantum dots to double concentric quantum ring structures transition. *Phys. Status Solidi C*, 6(4):928–931, 2009.

[114] C Somaschini, S Bietti, S Sanguinetti, N Koguchi, and A Fedorov. Self-assembled GaAs/AlGaAs coupled quantum ring-disk structures by droplet epitaxy. *Nanotechnology*, 21(12):125601, 2010.

[115] C Somaschini, S Bietti, N Koguchi, and S Sanguinetti. Coupled quantum dot-ring structures by droplet epitaxy. *Nanotechnology*, 22(18):185602, 2011.

[116] Y. Aharonov and D. Bohm. Significance of electromagnetic potentials in the quantum theory. *Phys. Rev.*, 115:485–491, 1959.

[117] N. A. J. M. Kleemans, I. M. A. Bominaar-Silkens, V. M. Fomin, V. N. Gladilin, D. Granados, A. G. Taboada, J. M. García, P. Offermans, U. Zeitler, P. C. M. Christianen, J. C. Maan, J. T. Devreese, and P. M. Koenraad. Oscillatory persistent currents in self-assembled quantum rings. *Phys. Rev. Lett.*, 99:146808, 2007.

[118] D Sonnenberg, A Kuster, A Graf, Ch Heyn, and W Hansen. Vertically stacked quantum dot pairs fabricated by nanohole filling. *Nanotechnology*, 25(21):215602, 2014.

[119] Y. H. Huo, A. Rastelli, and O. G. Schmidt. Ultra-small excitonic fine structure splitting in highly symmetric quantum dots on GaAs (001) substrate. *Appl. Phys. Lett.*, 102(15):152105, 2013.

[120] S. Kumar, R. Trotta, E. Zallo, J. D. Plumhof, P. Atkinson, A. Rastelli, and O. G. Schmidt. Strain-induced tuning of the emission wavelength of high quality GaAs/AlGaAs quantum dots in the spectral range of the 87Rb D2 lines. *Appl. Phys. Lett.*, 99(16):161118, 2011.

[121] Z. Y. Zhou, C. X. Zheng, W. X. Tang, D. E. Jesson, and J. Tersoff. Congruent evaporation temperature of GaAs(001) controlled by As flux. *Appl. Phys. Lett.*, 97(12):121912, 2010.

[122] Ernst Bauer. *Surface Microscopy with Low Energy Electrons*. Springer-Verlag, New York, 2014.

[123] Frank W. J. Olver, Daniel W. Lozier, Ronald F. Boisvert, and Charles W. Clark, editors. chapter 10. Cambridge University Press, 2010.

[124] D Wall, I Lohmar, K R Roos, J Krug, M Horn von Hoegen, and F-J Meyer zu Heringdorf. Imaging diffusion fields on a surface with multiple reconstructions: Ag/Si(111). *New J. Phys.*, 12(10):103019, 2010.

[125] M. Kuball, D. T. Wang, N. Esser, M. Cardona, J. Zegenhagen, and B. O. Fimland. Microscopic structure of the GaAs(001)-(6×6) surface derived from scanning tunneling microscopy. *Phys. Rev. B*, 51:13880–13882, 1995.

[126] Hai Xu, Y.G. Li, A.T.S. Wee, C.H.A. Huan, and E.S. Tok. On STM imaging of GaAs(001)-$(n \times 6)$ surface reconstructions: Does the (6×6) structure exist? *Surf. Sci.*, 513(2):249 – 255, 2002.

[127] Pavel Kocán, Akihiro Ohtake, and Nobuyuki Koguchi. Structural features of Ga-rich GaAs(001) surfaces: Scanning tunneling microscopy study. *Phys. Rev. B*, 70:201303, 2004.

[128] Zhiming M. Wang, Kyland Holmes, John L. Shultz, and Gregory J. Salamo. Self-assembly of GaAs holed nanostructures by droplet epitaxy. *Phys. Status Solidi A*, 202(8):R85–R87, 2005.

[129] J.E. Prieto and I. Markov. Stranski-krastanov mechanism of growth and the effect of misfit sign on quantum dots nucleation. *Surf. Sci.*, 664:172 – 184, 2017.

[130] Koichi Yamaguchi, Kunihiko Yujobo, and Toshiyuki Kaizu. Stranski-krastanov growth of InAs quantum dots with narrow size distribution. *Jpn. J. Appl. Phys.*, 39(Part 2, No. 12A):L1245–L1248, 2000.

[131] K. Fu and Y. Fu. Strain-induced stranski-krastanov three-dimensional growth mode of GaSb quantum dot on GaAs substrate. *Appl. Phys. Lett.*, 94(18):181913, 2009.

[132] E. Steimetz, F. Schienle, J.-T. Zettler, and W. Richter. Stranski-Krastanov formation of InAs quantum dots monitored during growth by reflectance anisotropy spectroscopy and spectroscopic ellipsometry. *J. Cryst. Growth*, 170(1):208 – 214, 1997. Metalorganic Vapour Phase Epitaxy 1996.

[133] Ch. Heyn, A. Stemmann, A. Schramm, H. Welsch, W. Hansen, and Á. Nemcsics. Regimes of GaAs quantum dot self-assembly by droplet epitaxy. *Phys. Rev. B*, 76:075317, 2007.

[134] Xinlei Li, Jiang Wu, Zhiming M. Wang, Baolai Liang, Jihoon Lee, Eun-Soo Kim, and Gregory J. Salamo. Origin of nanohole formation by etching based on droplet epitaxy. *Nanoscale*, 6:2675–2681, 2014.

[135] Christian Heyn. Kinetic model of local droplet etching. *Phys. Rev. B*, 83:165302, 2011.

[136] V. A. Gorokhov, T. T. Dedegkaev, Yu. L. Ilyin, V. A. Moshnikov, A. S. Petrov, Yu. M. Sosov, and D. A. Yaskov. The investigation of P and As diffusion in liquid gallium. *Cryst. Res. Technol.*, 19(11):1465–1468, 1984.

[137] H. Yildirim Erbil, G. McHale, and M. I. Newton. Drop evaporation on solid surfaces: Constant contact angle mode. *Langmuir*, 18(7):2636–2641, 2002.

[138] W. E. Boyce and R. C. DiPrima. *Elementary Differential Equations and Boundary Value Problems, 10th Edition*. Wiley, 2012.